AD-A220600

DTIC ACCESSION NUMBER

PHOTOGRAPH THIS SHEET

DTIC FILE COPY

LEVEL

1

INVENTORY

Physical Characteristics of Magnetic ----

DOCUMENT IDENTIFICATION

15 MAY 87 N00014-85-C-2225

DISTRIBUTION STATEMENT A

Approved for public release;
Distribution Unlimited

DISTRIBUTION STATEMENT

ACCESSION FOR

NTIS GRA&I

DTIC TRAC

UNANNOUNCED

JUSTIFICATION

BY

DISTRIBUTION/

AVAILABILITY CODES

DISTRIBUTION	AVAILABILITY AND/OR SPECIAL	
A-1		

DISTRIBUTION STAMP

DTIC
ELECTE
APR 17 1990
S D
E

DATE ACCESSIONED

DATE RETURNED

16 25

DATE RECEIVED IN DTIC

REGISTERED OR CERTIFIED NUMBER

PHOTOGRAPH THIS SHEET AND RETURN TO DTIC-FDAC

DTIC FORM 70A APR 87

DOCUMENT PROCESSING SHEET

PREVIOUS EDITIONS MAY BE USED UNTIL STOCK IS EXHAUSTED

FINAL REPORT

PHYSICAL CHARACTERISTICS OF MAGNETIC BACTERIA AND THEIR ELECTROMAGNETIC PROPERTIES IN THE FREQUENCY RANGE OF 1 - 400 GHz

BioMagnetech Corporation
301 East 47th St., Suite 6A
New York, NY 10017

FINAL REPORT

PHYSICAL CHARACTERISTICS OF MAGNETIC BACTERIA AND THEIR ELECTROMAGNETIC PROPERTIES IN THE FREQUENCY RANGE OF 1 - 400 GHz

BioMagnetech Corporation
301 East 47th St., Suite 6A
New York, NY 10017

Contract No.: N00014-85-C-2225

Period: 15 May 1985 - 14 May 1987

TABLE OF CONTENTS

ABSTRACT

Basic D.C. magnetic and gigahertz properties of magnetosome chains in the magnetotactic bacterium Aquaspirillium magnetotacticum were investigated. Cell yield in fermenter grown and batch cultures were increased by over an order of magnitude to 5 x 10^9 cells/ml, making large-scale production of A. magnetotacticum and magnetosomes possible. D.C. hysteresis and A.C. gigahertz remanence studies were carried out on whole cells, separated magnetosome chains and cells aligned on substrates. The results were compared with synthetic Fe_3O_4 and γ-Fe_2O_3 particles. Electromagnetic absorption is zero and in applied magnetic fields was determined up to 400 gigahertz for cells suspended in an inert binder. Birefringence of an aligned sample was detected. Magnetosomes in cells were shown to be enveloped by phospholipid bilayer membranes with membrane proteins, some of which are not present in the cellular plasma membrane. Research was also initiated on genetic transfer of magnetosome production, and on bioaccumulation by A. magnetotacticum of Pu^{4+} and other heavy metal ions from water.

I. SCALE-UP OF CULTURING AND HARVESTING OF MAGNETIC BACTERIA

A. Bioproduction of Single Domain Magnetite in Large Scale Batch Cultures

1. Introduction

a) Magnetotatic microbes: a primer

Discovered only within the last decade, magnetotatic microorganisms (Figs. I1, I2) are now widely known. Awareness and interest in these fascinating protists stems from two facets of their biology, (i) "magnetotaxis" (Fig. I1) or cell orientation and motility directed by the geomagnetic field and (ii) "magnetosomes" (Fig. I2), which are intracellular membrane-enveloped single crystals comprising single magnetic domains of magnetite (Fe_3O_4). Magnetotaxis and magnetosomes have been observed in prokaryotes and more recently in saprozoic euglenoids (I1, I2) which have eukaryotic cell structure. Only magnetotatic bacteria have been cultered axenically, however. The most thoroughly studied magnetotatic microorganism is Aquaspirillum magnetotacticum. Cultures of this freshwater bacterium consist of gram-negative, highly motile, bi-polarly flagellated, helical cells (Fig. I3).

Most of the dozens of other types of magnetotactic bacteria have been described only to a limited extent. They must be collected directly from natural environments or propagated in the laboratory in enrichment cultures. Both marine and freshwater types, including rods, spirilla, cocci, and other morphological forms are commonly encountered. Photographic descriptions of some of these diverse bacteria appear in Figure I4 and elsewhere (I3, I4). Aquaspirillum magnetotacticum, which appears to be fairly representative of other magnetic bacteria in terms of its basic magnetic characteristics, has

provided considerable insight into the physics and biology of the entire group.

A. Magnetotacticum is an obligately microaerophilic, heterotrophic denitrifier which can, under suitable conditions, also fix nitrogen at significant rates. Cells of this species can be grown in a completely chemically defined medium. Prior to recent work undertaken to improve cell yields (see below), cells grew to final yields of roughly 3×10^8 cells/ml. They must be cultured at very low dissolved oxygen tension (d.o.t.) of approximately 1 % of saturation (I5). Non-denitrigying cells are forced to respire with O_2. Consequently, when grown on ammonia as the sole nitrogen source they benefit from somewhat more oxygen in the medium, and final cell yields of such non-denitrifying cells can be measurably greater (5×10^8 cells/ml). As shown in Figure I5, however, the culture magnetite yield at a d.o.t. value of 10% is only 40% of the maximum obtained at 1 % O_2. Although they differ in the terminal acceptor used for electron disposal, both ammonia-grown and nitrate-grown cells appear similar in regard to the effect of O_2 on magnetite: magnetitie yields drop off either above or below the optimal d.o.t. value of approximately 1 % of saturation (Fig. I5).

Cells of A. Magnetotacticium do not ferment or use sugars. They use organic acids as sources of carbon and energy and show considerable versatility in their means of electron disposal. They contain a branched electron transport chain containing hemes of types a-, a_1-, b-, c-, d-, and o. They simultaneously express both a "high aeration" terminal oxidase (cytochrome o) and a "low aeration" oxidase (cytochromes d and a_1) under the microaerobic conditions required for their growth. In addition to electron disposal to O_2 via these oxidases, cells are also capable of nitrate and

nitrite respiration (forming nitrous oxide and dinitrogen) (I6). They also carry out electrogenic proton pumping with Fe^{3+} (I7) and are presumably, therefore, capable of sustaining a proton motive force with ferric iron reduction. Cells' ability to reduce iron may be associated with their ability to produce magnetite. Bacterial magnetite formation involves reduction of some of the iron in an oxidized precursor (I8). Conditions which favor magnetite formation (low oxygen supply, nitrate in lieu of ammonia as N source, and high iron concentration) are also those which promote dissimilatory iron reduction. Moreover, with ferric iron abundantly available, limitation of other electron acceptors favors magnetite formation. Thus, it is becoming increasingly evident that cell respiration may directly affect cell magnetite synthesis.

b) Biogenic magnetite: the magnetosome

Bacterial magnetite appears to be produced by partial reduction of a ferrihydrite ($5\ Fe_2O_3 \cdot 9\ H_2O$) precursor (I8; Fig. I6). The process may involve precipation, followed by solution and re-precipitation (I8) of iron atoms. The cell limits the upper size of its single crystal magnetite grains to single magnetic domain size which is in the vicinity of about 500 - 1000 angstroms. The mechanism by which cells limit crystal growth is not known. The result, however, is a narrow distribution of crystal sizes in the fully mature bacteria.

The envelope comprising the magnetosome boundry layer in cells of A. magnetotacticum strain MS-1 appears to be a biological membrane (lipid bilayer). Freeze-etching studies as well as TEM of thin-sectioned cells supports this interpretation. The magnetosomes in a partially purified state contain specific proteins not observed in either the cell inner or

outer membrane. The magnetosome membrane may control the size, morphology and orientation of magnetite single crystals within the cell. Cell culture conditions determine the numbers of magnetosomes per cell but not, as far as is known, these other parameters. There are, consequently, magnetosome genes which control magnetosome size, morphology, and orientation in a species-specific manner. At least 3 distinct crystal morphologies of bacterial magnetite are known.

Magnetosomes of A. magnetotacticum consist of 420 Å truncated octahedra (Fig. I7) arranged in a chain such that the [111] crystal faces lie along the chain axis (I10). Other magnetotactic bacteria possess magnetosomes consisting of truncated hexagonal prisms (Fig. I8). When in chained configurations, particles of this type also lie with the [111] faces in the chain axis. A third type of magnetosome is tapered or bullet-shaped (Fig. I9). These are also single crystals of magnetite but of unknown crystal morphology. Fine grain magnetite particles with either the hexagonal prismatic or tapered shapes cannot be produced by chemical precipitation methods and are therefore unique bacterial products (I11).

c) Culture methods for magnetic bacteria

i) Enrichment cultures

Many types of magnetotactic bacteria can be maintained in the laboratory only by means of enrichment cultures consisting of sediments and water collected from natural habitats containing them. They persist in such cultures after initial stages of active microbial growth characterized by microbial metabolism of low molecular weight substances which suppoort rapid and prolific biomass production. After depletion of the more easily

metabolizable substances, a prolonged subsequent phase characterized by clearing of the water and lower species diversity and lower bacterial density is reached. It is during this stage when the biomass is supported by polymer (cellulose, complex polysaccharides, etc.), degradation, that magnetotactic bacteria becomes greatly enriched in numbers. Addition of nutrients or of mineral salts (N, P) to such natural enrichments has a more harmful than stimulatory effect, and the factors which promote selective growth of magnetotactic bacteria in late stages of enrichment are not known.

ii) Stock cultures

Two magnetotactic bacterial strains were isolated from enrichment cultures and grown in pure culture in a chemically defined medium. The medium composition is given in Table 1. Cultures were maintained in 150 ml sealed serum bottles or flasks under an initial headspace of approximately 1 kPa O_2. During growth, additional O_2 was added as required to maintain microaerobic conditions in the headspace. Cell yields attained 2-3 x 10^8 cells/ml. Solid medium of the same composition but with 1% agar was used to for cloning cells. In solid medium cells grew densely especially at the centers of colonies. This suggested (i) that cells required protection from oxygen toxicity and (ii) that in medium of this composition cells did not form toxic metabolic products which would limit their own growth. Stock cultures were stored frozen in DMSO.

iii. 10 - 15 L scale batch cultures

Cells were grown in 10 - 15 L batches in glass carboys equipped with dissolved O_2 electrodes and/or means of adjusting the d.o.t. through stirring rate or sparging rate. The necessary O_2 was provided as a N_2/air gas stream mixed by means of capillary gas proportioning tubes. O_2

TABLE 1: Magnetic spirillum growth medium (MSGM)

Component	Added amount per liter
Tartaric acid	0.37 g
Succinic acid	0.37 g
Sodium acetate	0.05 g
Sodium nitrate	0.17 g
Monopotassium phosphate	0.69 g
Sodium thioglycollate *)	0.06 g *)
Resazurin (stock 1 g/L)	8 drops
Ferric quinate (0.01 M) **)	2 ml **)
Minerals ***)	5 ml ***)
Vitamins ****)	0.5 ml ****)
Distilled water	1 liter

*) Alternatively, 0.03 g ascorbic acid

**) Stock solution of 2.7 g/L FeC13 and 1.9 g/L Quinic acid

***) Mineral medium (pH 6.5 w/KOH) containing per liter:

Nitrilotriacetic acid	1.5 g
MgSO4.7H2O	3.0 g
MnSO4.H2O	0.5 g
FeSO4.7H2O	0.1 g
CoSO4	0.1 g
CaC12	0.1 g
ZnSO4	0.1 g
CuSO4.5H2O	0.01 g
AlK(SO4)2	0.01 g
H3BO3 (boric acid)	0.01 g
Sodium molybdate	0.4 g
Water	1 liter

****) Vitamin medium containing per liter:

Biotin	20 mg
Folic acid	20 mg
B-6 (pyridoxine HC1)	100 mg
B-1 (thiamine HC1)	50 mg
B-2 (riboflavin)	50 mg
Niacin	50 mg
Panthotenic acid (DL Ca-salt)	50 mg
B-12	1 mg
PABA	50 mg
Lipoic acid	50 mg

concentration in the influent gas stream was measured with a Beckman Instruments E2 paramagnetic oxygen analyzer and that of culture headspace with a gas chromatograph equipped with an electroncapture detector. The medium (Table 1) was prepared in 10 - 15 L volumes. Subsequent to pH adjustment, the medium was autoclaved (air atmosphere) for 1 hr. During cooling, the medium was sparged with sterile O_2-free N_2. Ferric quinate was added as a sterile supplement to the cooled medium which was then inoculated with 100 - 200 ml of a culture of actively motile and magnetic cells. Cultures were then sparged with O_2-free N_2 for 2 hr (10-20 ml/min) after which the vessels were sealed and incubated without mixing. Cultures achieved maximum growth after 4-5 days at 30°C. Cells were then harvested either by continuous flow centrifugation or filtration and washed in 25-50 mM phosphate buffer (pH 6.8), concentrated and stored at 4°C in buffer.

iv. Continuous cultures

Methods used for this type of culture have not been published. Cultures were maintained in commercial bench-top fermentation devices (New Brunswick Bio-flow 1.5 L bench top fermenter and a Pegasus 2 L fermenter). Each reactor vessel was equipped with pH and DO electrodes. A pH controller was used. However, automated DO control was not available. Adaptations were made to each commercial fermenter to allow growth of obligate microaerophiles. Nutrient feed was provided by means of pH feedback control to nutrient pumps connected to feed reservoirs. Delivery of oxygen was by means of diffusion through a silicone tube (O.D. 5/8", I.D. 3/16" 220 cm long) connected in-line with the N_2 inlet. This allowed for slow O_2 diffusion into the N_2 stream which, as a carrier (50-60 ml/min), provided microaerobic conditions in the reaction vessell as determined by means of

headspace analysis and DO electrodes.

The reactor vessels were autoclaved, the medium was sparged with O_2-free N_2 during cooling, and iron was then added to the cooled medium. After inoculation, the culture was allowed to grow briefly as a batch culture before activating the nutrient feed pumps. Upon activating the pumps, the culture was thereafter maintained as a true continuous culture. The culture was maintained at a dilution rate of 0.08 and had a mass doubling time of 7 hr.

d) Previous yields

Previous culture methods for magnetic bacteria resulted in cell yields of 3-5 x 10^8 cells/ml which corresponded to roughly 0.2 - 0.3 g wet weight or 20-30 mg dry weight bacteria/L. Of this, 2% of dry cell weight was magnetite iron yielding approximately 0.5 to 0.75 mg dry weight magnetite per liter of culture. Thus, from each 10 L culture it was possible to recover 5 - 7.5 mg purified magnetite.

For certain proposed applications of magnetic bacteria these yields have been adequate to demonstrate feasibility of applications or processes under evaluation. This was also sufficient for characterizing physical and chemical properties of the magnetite product. For other potential applications, however, product yield was clearly in need of improvement. Improved bio-product yields can be accomplished by (i) strain selection (ii) improved culture growth yields (iii) genetic manipulation to increase gene-copies and transcription rates (iv) use of environmental chemical and physical inducers which modulate gene expression or (v) combinations of these.

An effort to increase biomagnetic yields through improved culture growth yields was undertaken by BMC in 1986. These efforts were tremendously successful and strain MS-1 can now be cultured to cell densities normally associated with growth of E. coli. As a prelude to optimizing cell growth, an analysis was carried out of the culture medium previously used (see above) to grow A. magnetotacticum strains MS-1 and MS-2 as described in the Project Description below.

2. Project Description

a) Evaluation of culture medium

Bacteria can be considered in the most basic sense, to comprise the emperical formula:

$$C_1 H_{1.8} O_{0.5} N_{0.2}$$

The elemental composition of A. magnetotacticum is not known. However, that of another gram-negative bacterium, E. coli. is given in Table 2. "Lesser" elements usually comprise traces of the dry cell weight, and in this respect, A. magnetotacticum is exceptional because its iron composition is 2% of its dry weight (which is 100 x that of E. coli).

The culture medium used for A. magnetotacticum was examined to determine the maximum cell yields it could support. Estimated maximum cell concentrations based upon the elemental composition of the cells and growth medium are shown in Table 3. Previous culture methods for A. magnetotacticum resulted in very low final cell yields estimated to be 20 - 80 mg dry wt/l. Such low cell densities typically reflect nutritional limitations rather than growth inhibition due to formation of toxic metabolites.

Inspection of the growth data revealed multiple nutritional limitation

TABLE 2: Elemental Composition of Bacteria

ELEMENT	PER CENT DRY WEIGHT
C	50
O	20+
N	14
H	8
P	3
K	2
S	1
Na	1
Ca	0.05
Mg	0.05
Cl	0.05
Fe	0.2 (usually less)*

*A. magnetotacticum cells contain 2% of their dry wt as Fe

TABLE 3: Estimated maximum cell concentration based upon the elemental compostion of the growth medium.

Element	In medium; mg/L	In dry cells; % (by weight)	Maximum cell growth; g/L (dry weight)
Nitrogen	28	7-14	0.2 - 0.4
Potassium	194	0.5-1	19.4 - 38.8
Phosphorus	154	1-3	5.1 - 15.4
Sulfur	3.2*)	0.5-1	0.3 - 0.6 *)
Magnesium	1.5	0.5-1	0.15- 0.3
Iron	2	0.3-2	0.1 - 0.7 **)
Oxygen	60 ***)	---	0.03- 0.06 ***)
Carbon	280	--- aerobic	0.2 - 0.3 ****)
Carbon	280	--- anaerobic	0.04- 0.1 *****)

*) Assuming no thioglycollate in medium (using ascorbate as reducing agent)

**) Magnetic vs. nonmagnetic cells (iron contents of cells from Table 1 in Blakemore et al. 1979 publication)

***) Assuming aerobic growth; 0.5 - 1.0 g cell/g oxygen -- The oxygen concentration is here calculated assuming 1% oxygen in headspace (giving 30 mg/L equivalent oxygen concentration) plus oxygen available from nitrate to nitrite reduction.

****) Aerobic growth; 0.3 - 0.4 g cell/g tartaric acid equiv.

*****) Anaerobic growth; 0.05 - 0.15 g cell/g tartaric or equiv.

in the growth medium, neglecting even, the possibility of cells producing extracellular polymeric products. Apparent limiting factors in descending order were: Carbon/energy source, electron acceptor, iron, magnesium, and nitrogen, followed by sulfur. Thus, it seemed reasonable to expect that increases in cell yield of up to 100 X (to 2-10 g/l) might be achieved merely by modifying the culture medium constituents to remove these nutrient limitations.

b) Scale-up and optimization of cell and magnetite yields

Semi-continuously fed, discontinuously harvested batch cultures were grown in a Chemap 14 L glass fermenter fully automated for pH and D.O. control. D.O. was adjusted at different times during growth trials either by means of sparge or stirring rate. Cultures were sparged constantly with a stream of O_2-free N_2 (50-60 ml/min) during growth. O_2 was provided by means of a length of silicone tubing (o.d. 5/16"; i.d. 3/16"; 220 inches long) inserted into the N_2 supply line. This allowed for constant, limited diffusion of O_2 into the sparging gas stream. The growth vessel inlet and off-gasses (N_2, O_2, CO_2) were quantified by means of a gas flow mass spectrometer. Nutrients were provided on demand by means of pH feedback control to an in-line peristaltic feed pump. Since nutrients were added on demand during growth and only small volumes of culture were removed for cell yield and magnetite analysis, the culture volume increased during each run from about 7 to 10 L.

As a consequence of a preliminary growth experiment in this apparatus, it was possible to deduce the yield coefficients for several nutrients, notably for the carbon source - tartaric acid. By the end of growth 160 mg dry wt of product had consumed 0.87 g/l tartaric acid. Thus:

$$Y_{tartaric} = 160/870 = 0.18 \text{ g cell/g tartaric acid}$$

Assuming cells are 50% carbon, and since tartaric is 34% C then:

$$\frac{0.18 \text{ g cell/g tartaric} \times .50}{0.34} = 26\% \text{ of tartaric acid C consumed}$$

went to cell biomass.

Thus, an estimated 74% of tartaric acid C consumed went to CO_2. Since tartaric acid has m.w. 140:

$$\frac{870 \text{ mg tartaric acid}}{140 \text{ mmoles}} = 6.2 \text{ mmoles TA} \times 0.74 \times 4 \text{ carbons/mol} =$$

18.4 mmoles CO_2 expected (assuming no other products were excreted by cells). In confirmation of these predictions, using a mass spectrometer, the measured quantity of CO_2 was 17 mmole. It is clear that roughly 75% of substrate carbon utilized was dissimilated (oxidized to CO_2) and 25% was assimilated into cell material.

Because it is toxic, cells could not be provided with the full complement of oxygen necessary to support the rate and amount of growth observed for the quantity of tartaric acid utilized. Therefore, additional electron acceptor was provided as nitrate in the form of nitric acid.

From 293 mg/l of nitric acid utilized and 870 mg/l of tartaric acid utilized, the cells produced 159 mg/l dry weight. This meant that for balanced feeding, a mixture consisting of 1/3 nitric and 2/3 tartaric would be appropriate. Actually since nitric comes as a 70% solution, a mixture containing 100 g/l tartaric and 48 g/l nitric acid would be in optimal proportions to prevent imbalance between oxidant and reductant required to support growth. An additional advantage in using this mixture was that only

one nutrient feed controller was needed to supply both oxidant and reductant.

On the basis of these results, in a susequent batch culture the following nutrient feed mixture was employed in which the (i) the proportion of C/N was adjusted optimally (ii) the quantity of iron and mineral nutrients were also increased to prevent both nutrient limitation and sufficient iron for cells to make magnetite optimally:

100	g/L	L-tartaric acid
32	g/L	HNO_3
1.7	g/L	$FeSO_4$ 7 H_2O
300	ml/L	Stock Mineral Solution

With the use of this balanced feed mixture the maximum optical density increased to 1.2, and the final cell mass to 325 mg dry wt/L corresponding to 5×10^9 cells/ml. This is more than ten times the growth ever before achieved with this organism and is equivalent to the cell yields commonly associated with growth of E. coli.

Cell yields have not yet been maximized. In related studies using 1.5 L continuous cultures, major increases in cell growth were obtained merely by increasing the supply of reductant in a system provided with automatic pH control. This suggests that cells were simultaneously using both O_2 and nitrate to dissimilate the carbon source.

Continuous culture methods provide benefits of precise regulation of O_2, pH, and nutrients and permit study of cells maintained at constant growth. We undertook to clarify the relationship of iron and O_2 to growth and magnetic yields of cells in continuous culture.

The chemostat used was all glass and at no time during growth did the

culture or any solutions added to it come in contact with ferrous metals. The total background iron concentration of medium to which no iron compounds were intentionally added was 0.35 μm. Iron was supplied as ferric quinate. The culture (2.0 L volume) was maintained at D = 0.075 h^{-1} and the mass doubling time (T_D) was held at 9.2 h. Dissolved O_2 was monitored with a galvanic electrode and maintained at 1% of saturation by adjusting the N_2-to-air ratio of a mixture supplied at a constant rate of 3.3 cc . min^{-1}. Culture pH was maintained at 6.8 by means of an automatic controller delivering sterile 3 N H Cl.

With iron held constant at 8 μm, culture biomass approximately doubled with each doubling of nitrate concentration over the range 2 to 8 mM (Fig. I10). This established that nitrate, which served both as a nitrogen source and as a terminal electron acceptor, was a limiting nutrient at 4 mM. This concentration was used in subsequent studies with iron.

Culture growth over the range of iron concentrations 2-32 μm with nitrate limiting (4μm) is shown in Figure I11. As expected, increases in iron from 2-8 μm had no effect on biomass yield of these nitrate limited cultures. However, a striking and unexpected result occurred as iron was further increased from 8 to 16 μm; the biomass doubled. Thus, at some value between 8 and 16 μm, iron relieved cells of nitrate limitation. However, corresponding yield increases were not observed with further increase in iron from 16 to 32 μM (Fig. I11). Since iron in μM quantity was not merely substituting for nitrate (present in mM amounts) as an alternate terminal electron acceptor, we sought another explanation for its stimulatory role.

The increase in biomass with 16 μm iron was accomplished within approximately 10 h by an increased culture O_2 demand. Unless the d.o.t. was

maintained at 1% by providing O_2, the increase in growth was minimal and cells became non-magnetic (Fig. I12). Restoration of microaerobic conditions reversed the growth trends (Fig. I12, arrow). However, cell biomass returned to only 35% of the expected value and cells remained non-magnetic. This illustrates that despite having nitrate, cells required O_2 for growth and that after experiencing O_2 limitation they do not fully recover even after three culture volume changes.

The increase in biomass and O_2 demand triggered by the shift to 16 μm iron was consistent with the possibility of a shift in cell respiration from nitrate to O_2 as acceptor, thereby relieving cells of nitrate limitation. The range of iron values effecting this change was similar to that shown previously (I7) to effect siderophore production and synthesis of a 55 Kdal iron-repressible outer membrane protein (possibly involved in iron transport) by cells in batch culture. However, culture fluids obtained at each steady state did not contain hydroxanate siderophore and cells produced the 55 Kdal IROMP at each iron tested. Cells each produced an average of 7 magnetosomes at each iron concentration, although at lower iron many particles were smaller than normal. The results indicate that information concerning siderophores, IROMPS, and magnetosome production gathered from cells in batch culture may not be consistent with results obtained using continuous cultures. For large scale biomagnetic production a certain amount of empirical information will be needed and that database now begun, will need to be expanded using continuous cultures with automated control growth parameters.

In Fig I13 we show a graphic representation of the improvement in cell yields by showing the degree of turbidity change from the typical culture

prior to the scale-up task and the current state of scaled-up growth in fermenter. Figure I14 gives an illustration of a 150 liter carboy using an improved batch culture process in the high yield region.

It is fortunate that high culture yields of magnetic bacteria (nearly comparable to those obtained with E. coli) are now possible, but in a simple mineral medium containing tartaric acid as the carbon and energy source. Tartaric acid is a readily available feedstock well suited to mass culture of these microorganisms in industrial scale operations. At the present time it is possible to project from current cell yields to an eventual cost per pound of dry bacteria of less than $100, possibly as little as $10/lb.

3. Suggested Activities

Target cell yields of 2g/l appear attainable with this bacterium. As cell yields increase, it may become necessary to increase the pH buffering capacity of the medium. Additional increases in cell growth would be expected by supplying preformed growth factors, vitamins and nucleotides in the culture medium in the form of a small amount of yeast extract. Computer interfacing to further automate and stabilize the culture during growth would be beneficial because of the sensitivity of the organisms to fluctuations in d.o.t.

Some attention must be directed to the magnetic state of the cells produced in high yields by the methods described. Cultures produced to date included a fair proportion of non-magnetic bacteria which probably reflects improper oxygen control throughout the growth of the culture or else iron limitation at the high cell densities attained.

B. Harvesting of Magnetic Bacteria

Harvesting methods for magnetic bacteria include centrifugation, membrane filtration, magnetic separation and possible combinations of these such as magnetic membrane filtration.

Magnetic separation methods have been developed for large scale process streams such as removal of iron impurities from kaolin or coal (FeS). BMC has developed small scale magnetic separations which have been used to evaluate the magnitude of the magnetic field gradient required to remove the bacteria from flowing streams of culture fluid or other menstrums within certain criteria of time and shear velocity, etc. These results have been very satisfying to date. The bacteria can be effectively separated from static fluids or those in motion in small tubes. A patent has been issued for use of the cells or their particles in magnetic separation techniques.

Magnetic separation methods if applied to fermentation fluids can be expected to have certain advantages over centrifugation and membrane filtration methods. These include: (a) high throughput (b) no clogging of pores (c) lower cost (d) increased safety over centrifugation (e) low noise and (e) efficient recovery of cells with no breakage and consequently no alteration of the desired cell product by internal cell enzymes.

C. REFERENCES

I1. Blakemore, R. P., Science 190: (1975) 377.

I2. Frankel, R. B., and Blakemore, R. P., J. Magn. Magn. Mater. 15-18 (1980) 1562.

I3. Blakemore, R. P., Ann. Rev. Microbiol. 36, (1982) 217.

I4. Blakemore, R. P., and Frankel, R. B., Sci. Am. 245 (1981) 58.

I5. Blakemore, R. P., Maratea, D., and Wolfe, R. S., J. Bacteriol. 140 (1979) 720.

I6. Bazylinski, D. A. and Blakemore, R. P., Appl. Environ. Microbiol. 46 (1983) 1118.

I7. Paoletti, L. C., and Blakemore, R. P., J. Bacteriol. 167 (1986) 73.

I8. Frankel, R. B., Papaefthymiou, G. C , Blakemore, R. P., and O'Brien, W., Biochem Biophys. Acta 763 (1983) 147.

I9. Mann, S., Frankel, R. B., and Blakemore, R. P., Nature 310 (1984) 405.

I10. Balkwill, D. L., Maratea, D., and Blakemore, R. P., J. Bacteriol. 141 (1980) 1399.

I11. Blakemore, R. P., Short, K. A., Bazylinski, D. A., Rosenblatt, C., and Frankel, R. B., Geomicrobiol. J. 4 (1984) 53.

D. FIGURE CAPTIONS

Figure I-1: Optical microscope photograph of A. magnetotacticum in a water drop, aligned by a magnetic field.

Figure I-2: (ieft): Electron micrograph of thin section of A. magnetotacticum showing paratial chain of magneto sources. (right): magnetosome chains after separation from cell debris.

Figure I-3: Electron micrograph of negatively strained whole cell of A.magnetotacticum with chain of magnetosomes. Cell is approximately 3 microns long.

Figure I-4: Magnetotactic bacteria with hexagonally prismatic magnetosomes. TEM of negatively stain sells. Bars = 1 micron.

Figure I-5: Culture Fe_3O_4 yield plotted as a function of O_2 pressure in the headspace for cells grown on NO_3^-, NH_4^+ and NO_3^- + NH_4^+.

Figure I-6: Schematic representation of Fe_3O_4 precipitation process in A. magnetotacticum (after Ref. I8).

Figure I-7: (top): Electron micrograph of unidentified magnetotactic rod with chain of magnetosomes. (inset): morphology of magnetosomes from high resolution electron microscopy and electron diffraction studies. (bottom): Chains of magnetosomes following isolation from cell debris.

Figure I-8: Unidentified magnetotactic microorganism from Japan with chain of magnetosomes. (Insets): Enlargement of magnetosomes; magnetosome morphologies from high resolution electron microsopy and electron diffraction.

Figure I-9: Magnetotactic bacteria with bullet-shaped magnetosomes. TEM of negatively stained cells. Bars = 1 μm.

Figure I-10: Effect of nitrate on growth of strain MS-1 continuously cultured with 8 um iron. Absorbance, ·; Cell #, ; Biomass, □.

Figure I-11: Effect of Fe concentration on growth of A. magnetotacticum strain MS-1 in continuous culture as measured by: Absorbance, ·, Cell #, Δ; Biomass, □.

Figure I-12: Effect of O_2 deprivation on strain MS-1 cells as measured by Absorbance, (·) and biomass (□). Arrow indicates time of O_2 replenishment.

Figure I-13: Sealed bottles of A. magnetotacticum illustrating highly improved yields (right) compared to normal yields (center) and uninoculated medium (left).

Figure I-14: 150 liter batch culture of A. magnetotacticum growing under the high yield regime.

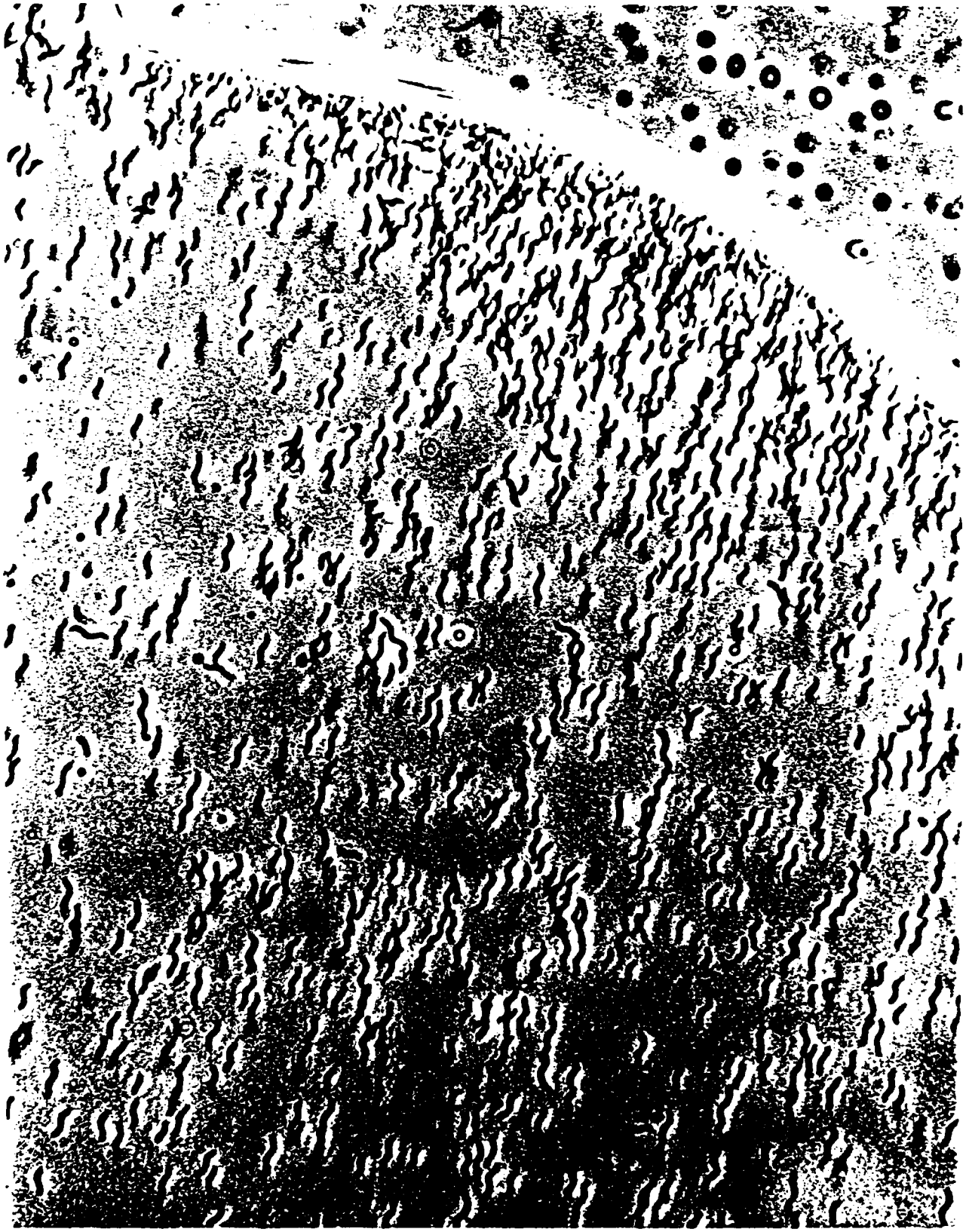

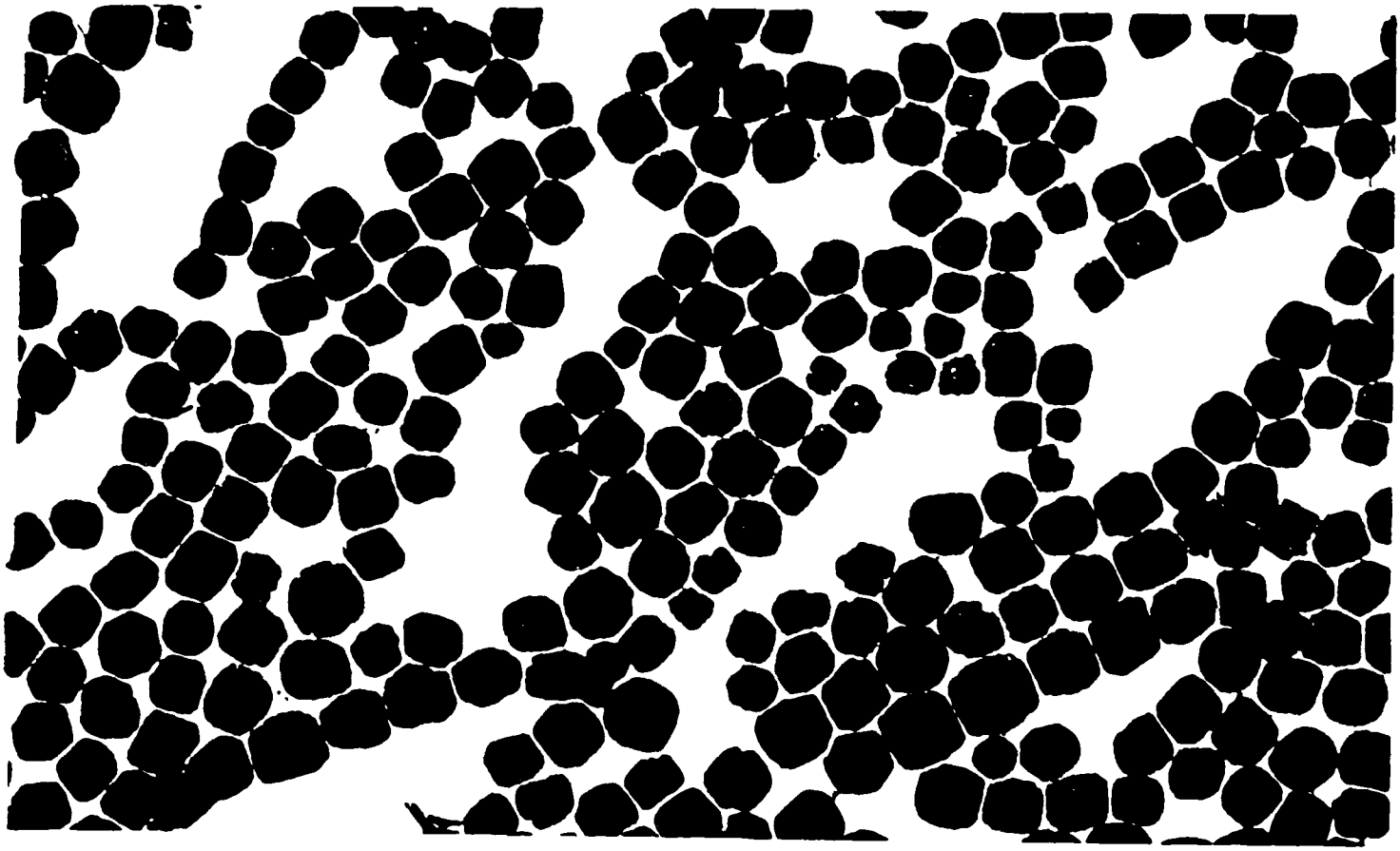

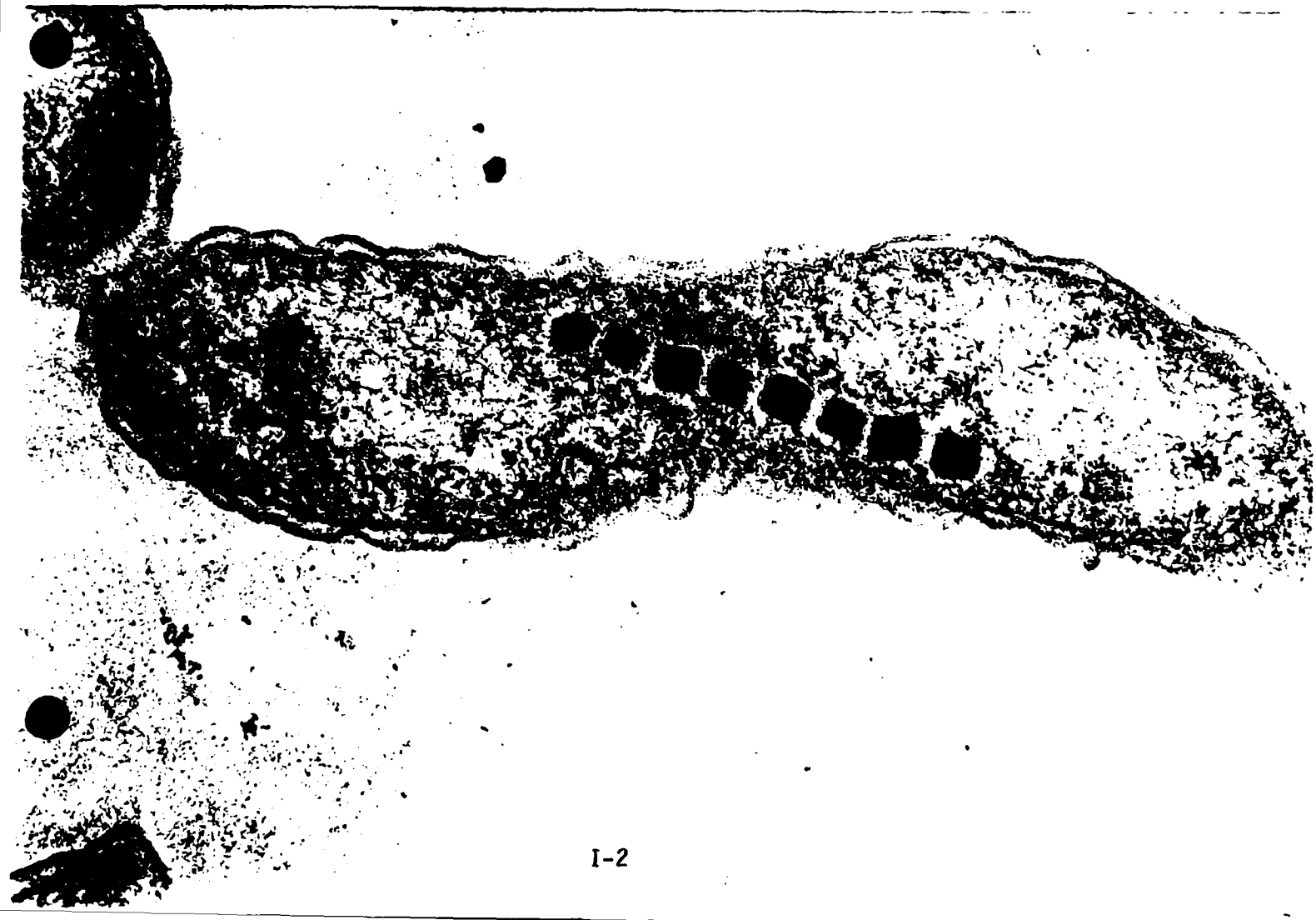

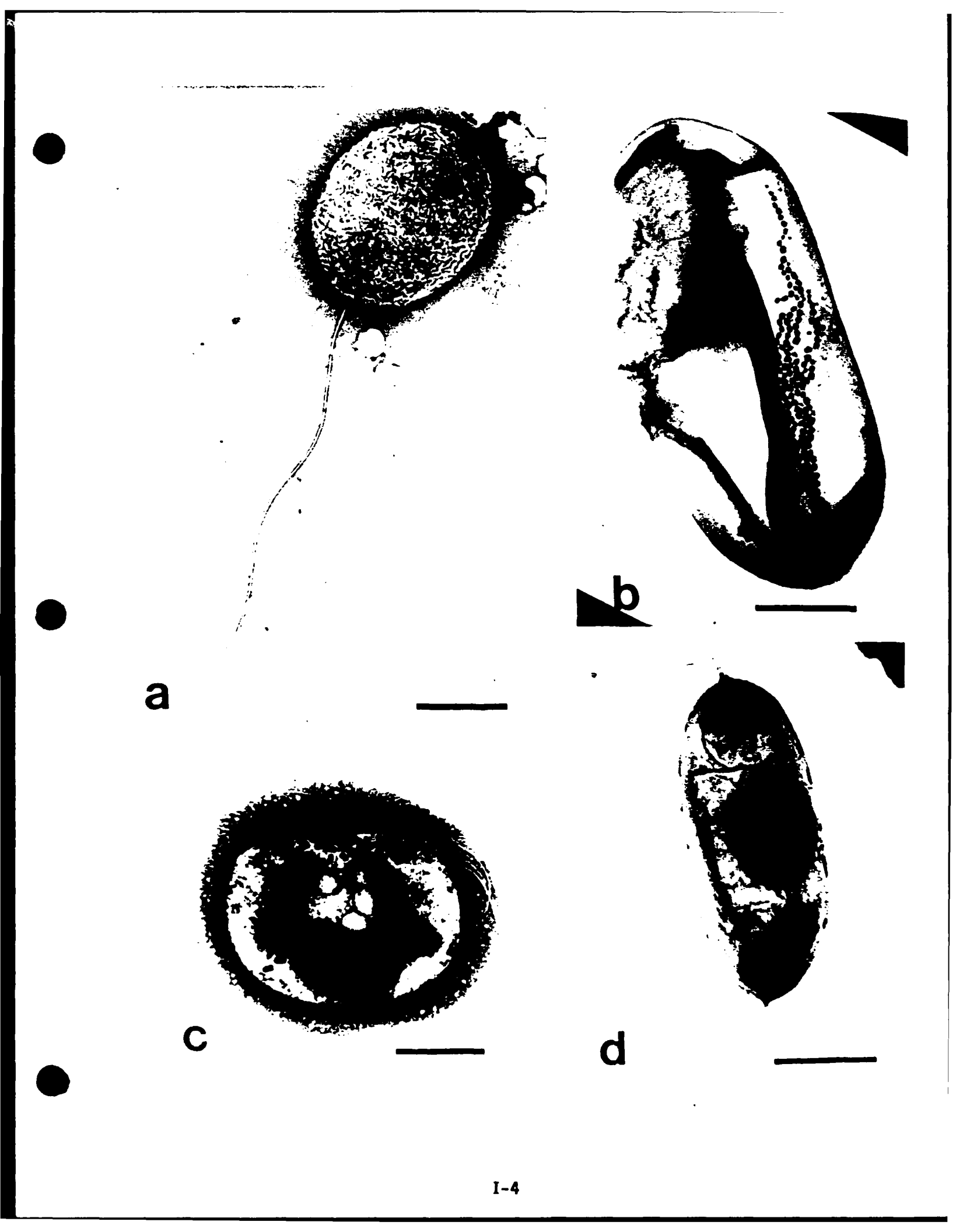
a
b
c
d

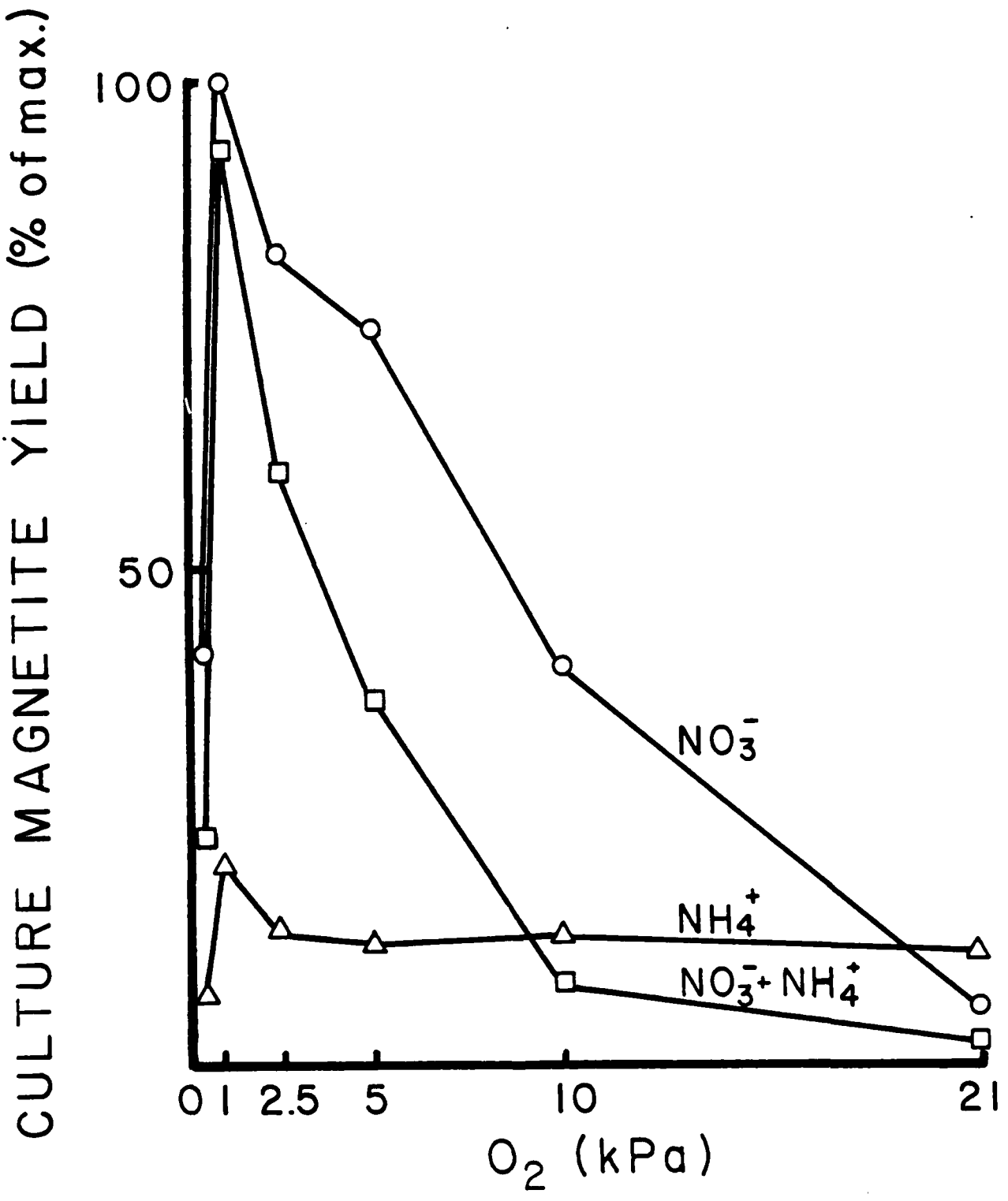
CULTURE MAGNETITE YIELD (% of max.)
100
50
0 1 2.5 5 10 21
O_2 (kPa)
NO_3^-
NH_4^+
$NO_3^- + NH_4^+$

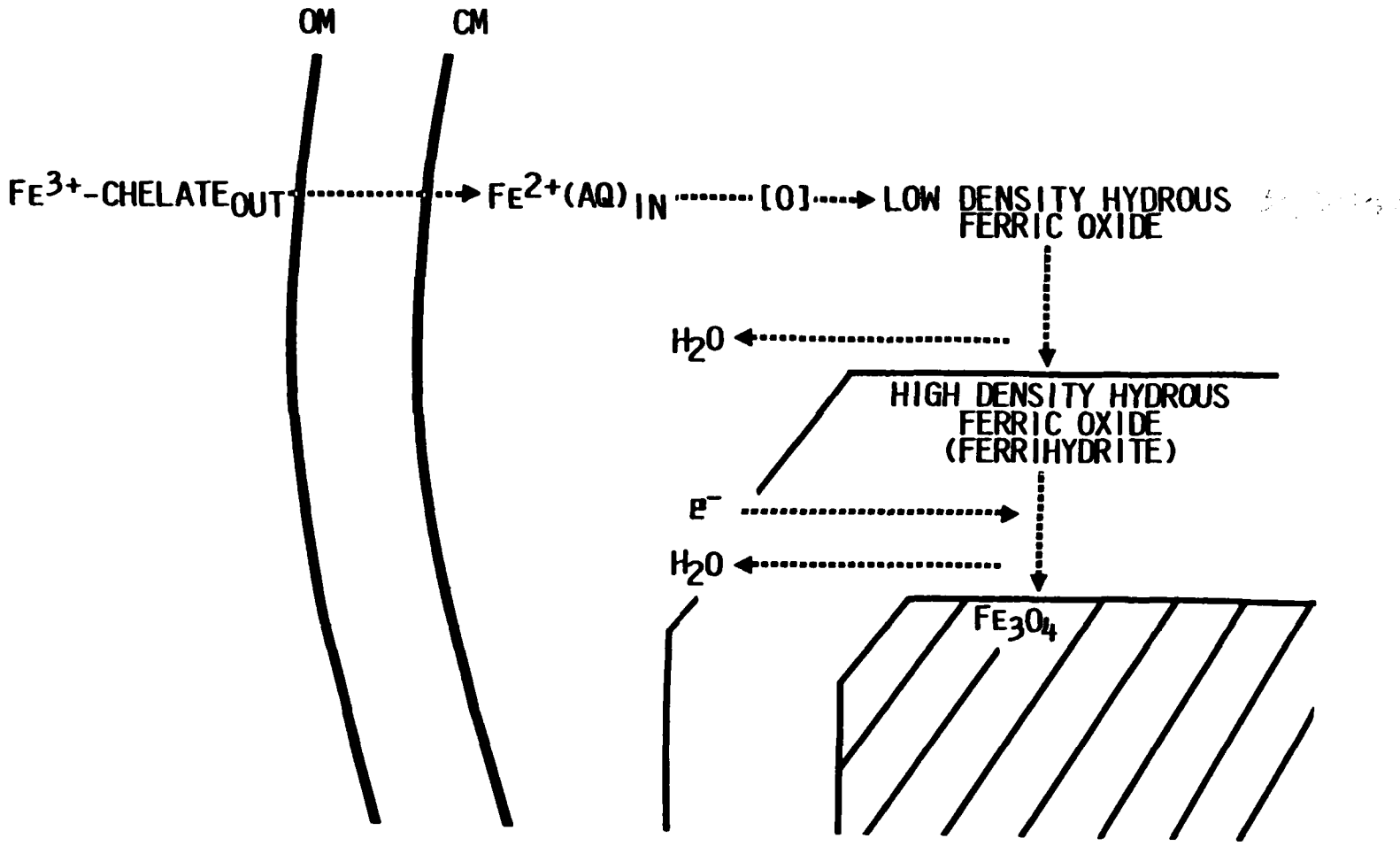
OM
CM
Fe^{3+}-CHELATE$_{OUT}$
$Fe^{2+}(AQ)_{IN}$
[O]
LOW DENSITY HYDROUS FERRIC OXIDE
H_2O
HIGH DENSITY HYDROUS FERRIC OXIDE (FERRIHYDRITE)
e^-
H_2O
Fe_3O_4

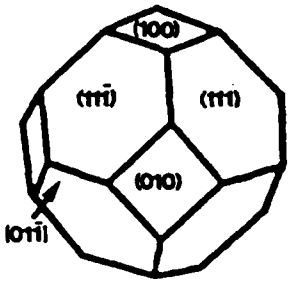
(100)
(111̄)
(111)
(010)
[011̄]

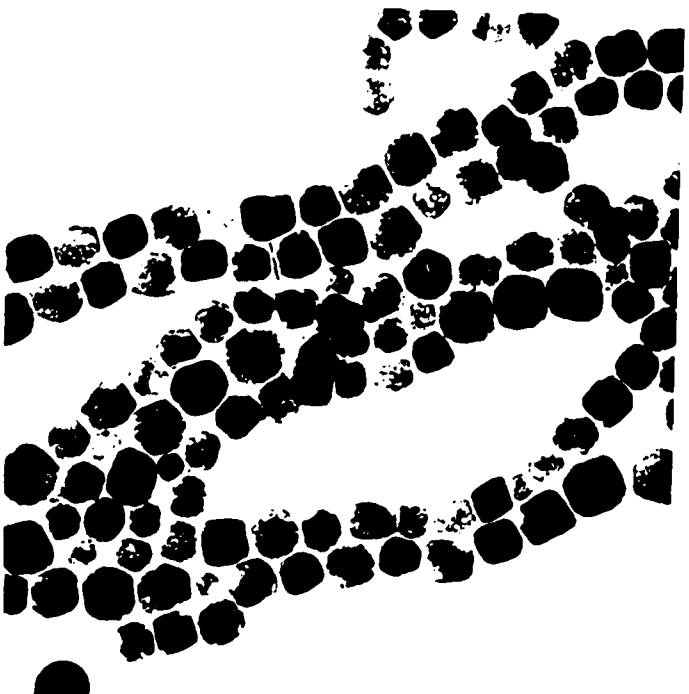

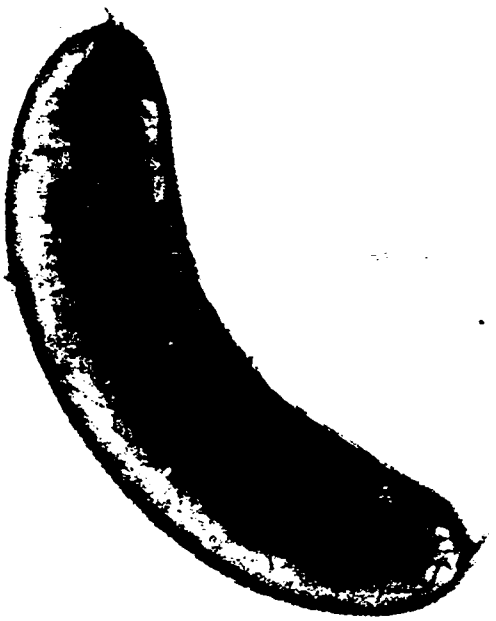

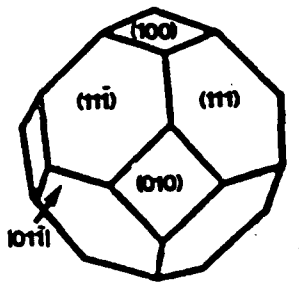
(100)
(111)
(111)
(010)
(011)

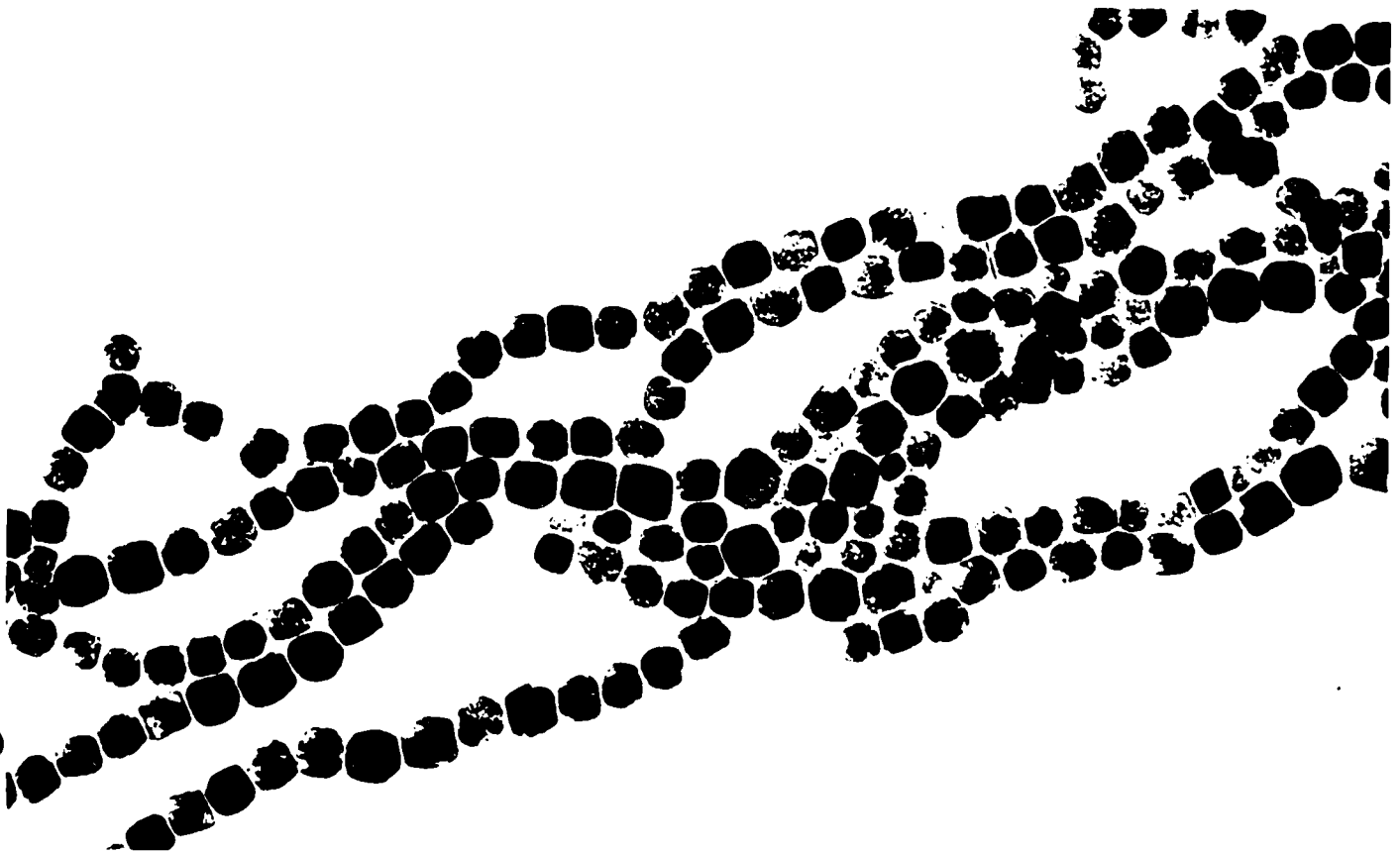

[2̄11]
[01̄1̄]
(111)
(1̄11)
(11̄1)
(01̄1)
(1̄1̄1)
001
1̄11
100
110
010
10̄1
01̄1
1̄10
1̄00
00̄1
1̄01
[2̄11]
[01̄1̄]

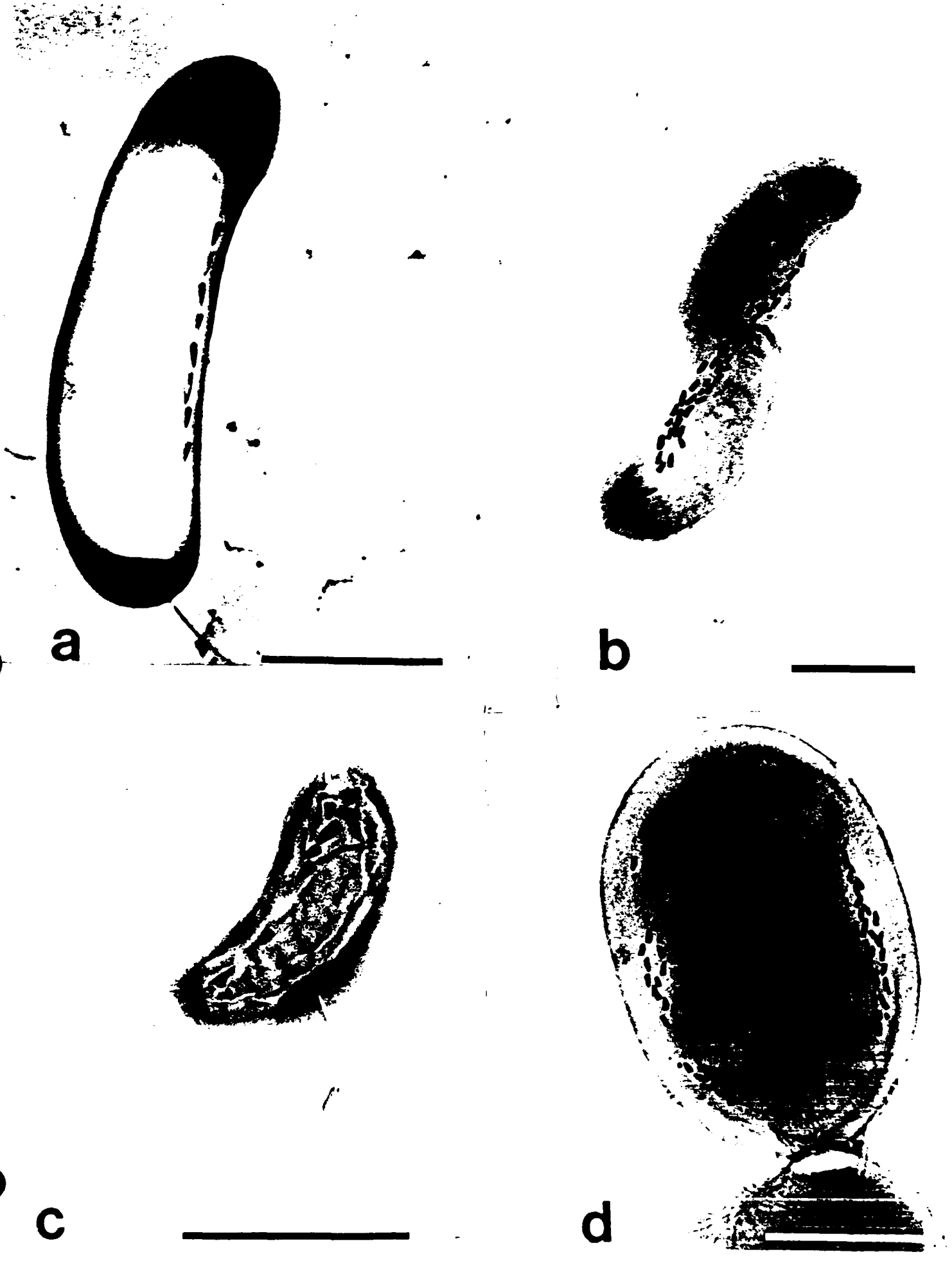
a
b
c
d

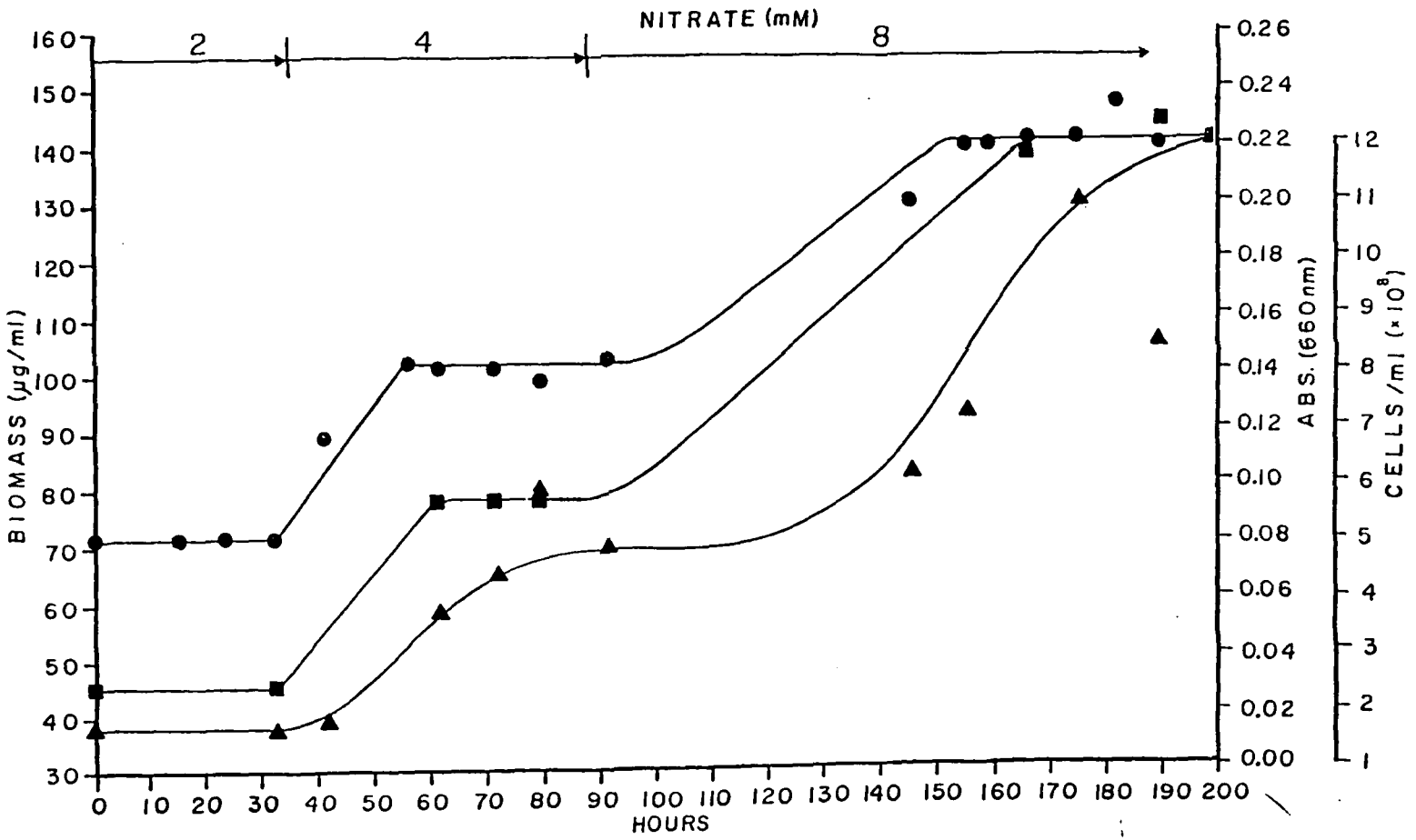
NITRATE (mM)
2
4
8
BIOMASS (µg/ml)
ABS. (660nm)
CELLS/ml (×10⁸)
HOURS
160
150
140
130
120
110
100
90
80
70
60
50
40
30
0.26
0.24
0.22
0.20
0.18
0.16
0.14
0.12
0.10
0.08
0.06
0.04
0.02
0.00
12
11
10
9
8
7
6
5
4
3
2
1
0 10 20 30 40 50 60 70 80 90 100 110 120 130 140 150 160 170 180 190 200

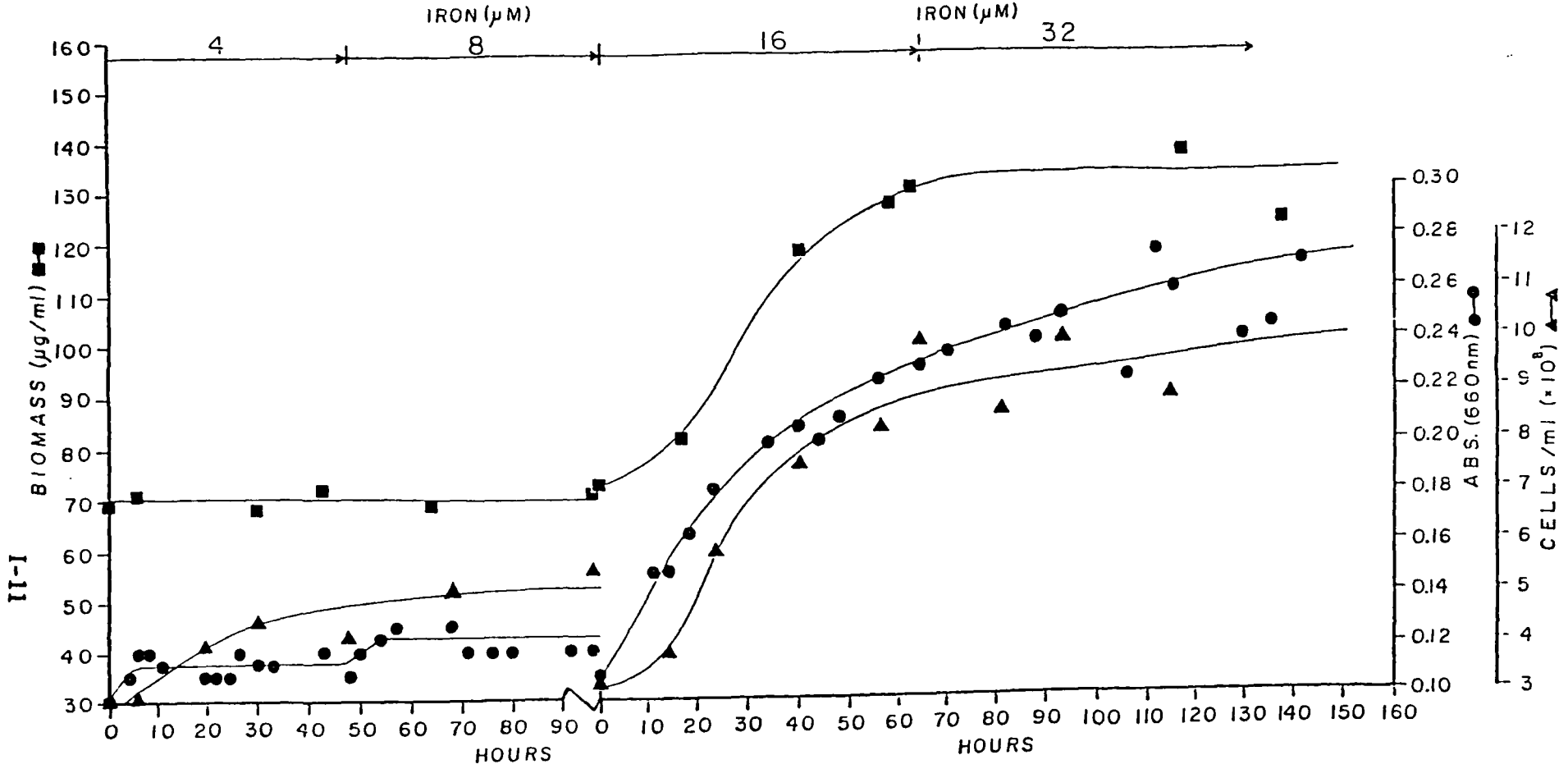
IRON (μM)
4
8
IRON (μM)
16
32
BIOMASS (μg/ml)
ABS. (660nm)
CELLS/ml (×10⁸)
HOURS
HOURS

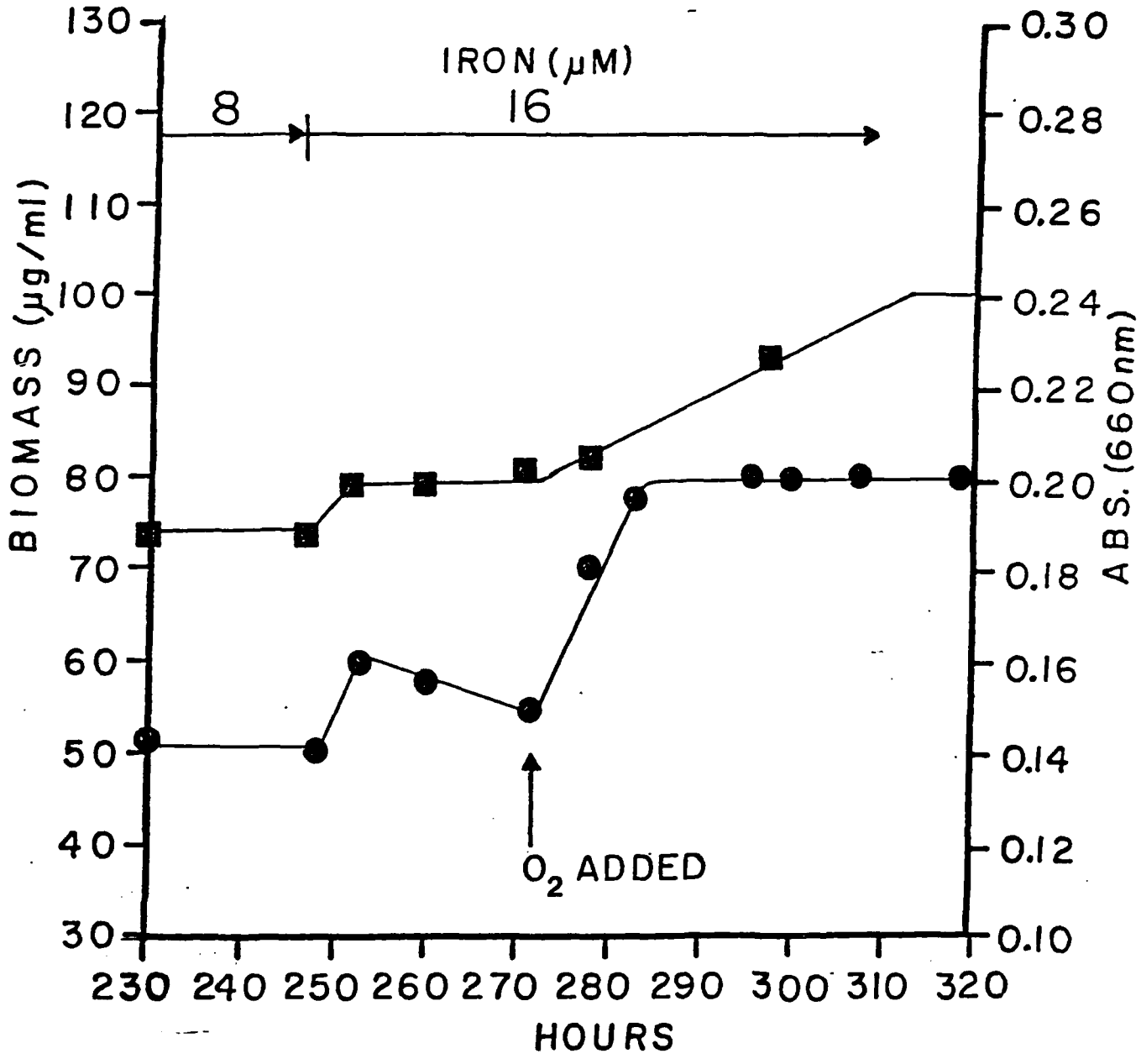
IRON (μM)
8
16
BIOMASS (μg/ml)
ABS. (660nm)
130
120
110
100
90
80
70
60
50
40
30
0.30
0.28
0.26
0.24
0.22
0.20
0.18
0.16
0.14
0.12
0.10
O2 ADDED
230 240 250 260 270 280 290 300 310 320
HOURS


typical culture of MS-1 in MSGM O.D. 0.08
MS-1 in MSGM grown in fermenter O.D. 1.2

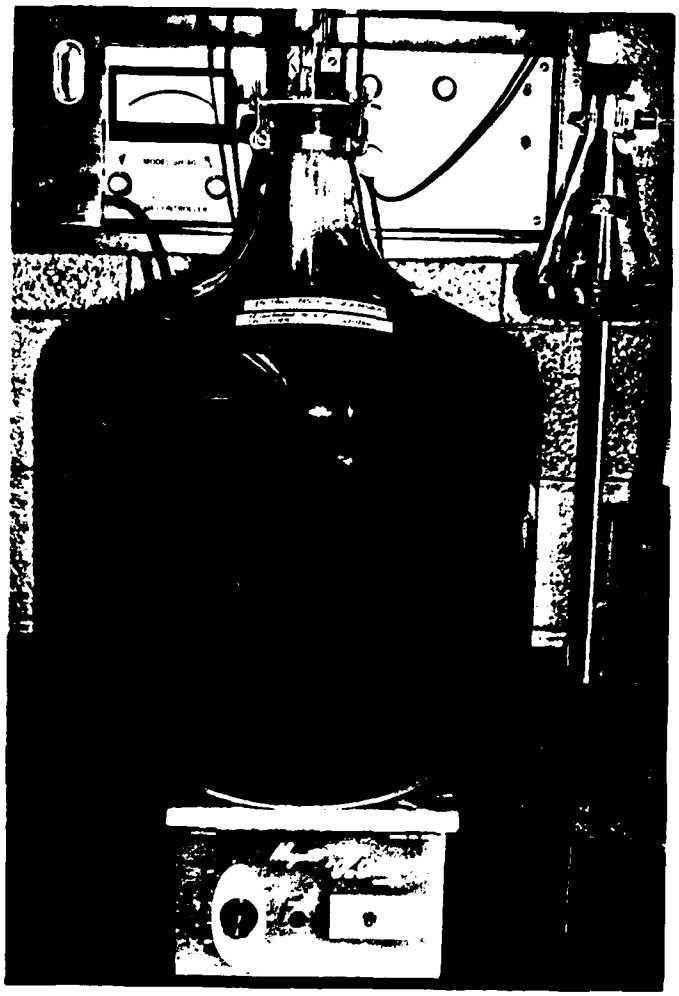

II. BASIC MAGNETIC PROPERTIES OF MAGNETIC BACTERIA

A. Experimental Magnetic Procedure

Magnetic measurements were made on samples of freeze-dried cells of A. magnetotacticum. One sample was prepared by pressing 56.4 mg of freeze-dried cell powder into a 5 mm pellet. Other samples were prepared by thoroughly mixing the cell powder with fast drying epoxy to ensure immobilization of the material during the measurement process. D.C. hysteresis loops were measured with a vibrating sample magnetometer after saturating the sample magnetically at 90 degrees to the measurement axis. Additional measurements were made using a novel rotating sample magnetometer.

Remanent magnetization (RM) was measured in a five layer mu-metal shield using a commercial fluxgate spinner magnetometer. All RM measurements were at least 10-100 times above the lower limit of the instrument. Alternating field (AF) demagnetization was performed along a single axis using a resonant-type device, with a working frequency of 60 Hz and a peak AF of 1200 G. The AF coil was situated within Helmoholtz coils to reduce any stray, dc fields to approximately less than 50×10^{-5} G, within the sample volume. Isothermal remanent magnetization (IRM) was produced using either a short-duration pulse discharge coil, capable of producing fields up to 1000 G, or an iron-cored electromagnet, with a peak field of 10,000 G. IRM acquisition curves were measured by applying incrementally increasing fields to initially demagnetized samples and noting the IRM produced. The reverse process to this was dc demagnetization, which consisted of applying increasingly higher reverse-polarity fields to a saturation IRM (SIRM). Anhysteretic remanent magnetization (ARM) was

imparted using a solenoid which fitted within the AF demagnetization solenoid. After a sample was initially AF demagnetized at 1200 G, and ARM was imparted to 6 G. All ARM's were produced by dc fields which were always parallel to the axis of the alternating field. Viscous remanent magnetization (VRM) was induced in the sample by exposing it to a constant field of 5 G, for approximately 16 hours. The decay of VRM in zero field was then measured at logarithmic time intervals. Samples were AF demagnetized at 1200 G immediately prior to the start of the acquisition process. Low-field initial susceptibility was measured using a commercial AC bridge device.

Two samples were studied exhaustively: (1) M-1, which consisted of intact freeze-dried cells; and (2) M-2, which consissted of freeze-dried, separated magnetosomes. From the saturation magnetizations, the former had approximately 1% by weight of magnetite, while the later had approximately 14% by weight. The freeze-dried powders were suspended in clear epoxy (non-magnetic) for remanence measurements. The volume concentration of magnetite of M-1 was approximately 1.29×10^{-5}. The small quantity of powder available for M-2 (a few milligrams) made an exact estimate for the volume concentration difficult; however, it was estimated to be at least 74.7×10^{-3}. Furthermore, because of the overall higher percentage of magnetite in the separated magnetosomes used to make M-2, particle agglomeration and clumping were more likely to occur; hence, local concentrations may be much higher than that estimated above.

B. D.C. Measurements

1. Hysteresis Loops

Figure II1 and II2 and show the initial magnetization and hysteresis curves of M-1 measured to ± 600 Oe and ± 1200 Oe, respectively. The primary quantities determined by the hysteresis loop are the coercive force, H_c, and the ratio of the remanent magnetization, M_R, to the saturation magnetization, M_s. The saturation magnetization σ_s was measured in an applied field of 6 kOe. For this sample, σ_s = 0.60 emu/gm, H_c = 160 kOe, and M_R/M_s = 0.43.

The value of σ_s is equivalent to an Fe_3O_4 content of about 1% dry weight of the cells. The shape of the hysteresis loop is consistent with the Stoner-Wohlfarth (SW) model (II1) of coherent rotation. A theoretical hysteresis loop calculated from the SW model for a random array of non-interacting, randomly oriented magnetic dipoles of single-domain character with uniaxial anisotropy, H_A, is shown in Figure II3. H_A was determined as described below.

The distribution of anisotropy energies in the sample was determined by measuring the component of magnetization normal to the magnetizing field H after magnetizing the sample to saturation, reducing the field to zero, and rotating the sample by 6 degrees (II2, II3). From these data, the anisotropy field distribution was calculated and plotted in Figure II4. The mode of the anisotropy distribution H_A = 440 Oe.

This value was checked by measuring the initial susceptibility of a spinning sample with the Hall probe technique, as shown in Figure II5. The result is H_A (average) = 476 Oe, in good agreement with the other method. This value of H_A was used with the SW model to calculate the theoretical

hysteresis loop in Figure II3.

Measurements were also made on samples of magnetic bacteria grown in batch culture that were fixed in 1% gluteraldehyde following growth and harvesting. A portion of this batch was subsequently freeze-dried for electromagnetic measurements. Another portion was kept in dense suspension.

2. Magnetically Induced Birefringence

The average magnetic moment per bacterium in the suspension was determined by means of the magnetically induced birefringence of the suspension (II5). The experimental apparatus is shown in Fig. II6. A laser beam is passed through a linear polarization analyzer before striking the detector. The analyzer is initially set at 90 degrees (extinction) to the polarizer and no photons strike the detector. When the magnetic field at the sample is zero the birefringence of the sample is zero and the polarization of the beam is not affected. As the magnetic field perpendicular to the beam and 45 degrees to both the polarizer and analyzer is increased the sample becomes increasingly birefringent due to the increasing alignment of the cellular magnetic dipoles in the magnetic field direction. The birefringence of the sample changes the polarization of the beam from linear to elliptical, and photons pass the analyzer and strike the detector. The intensity measured by the detector is a measure of the birefringence of the sample and hence the degree of alignment of the cells. Thus intensity as a function of magnetic field data can be fit to yield the average magnetic moment of the cells in the suspension. In the actual measurement a null technique is employed to increase the signal to noise ratio. A Pockel's cell is employed to cancel the birefringence of the sample and restore the extinction condition. Since the birefringence of the

Pockel's cell is known this is a measure of the birefringence of the sample.

The magnetically induced birefringence of the sample $\Delta n(H)$ is given by the expression

$$\Delta n = N \Delta p V \langle P_2 (\cos \theta) \rangle \qquad \text{(II.1)}$$

where N is the number density of the bacteria, Δp is the optical polarizability anisotropy per bacterium, V is the bacterial volume, and $P_2(\cos\theta) = 3/2 \cos^2\theta - 1/2$ is the second Legendre polynominal. θ is the angle between the bacterium and the optic axis. The brackets denote the ensemble average. For bacteria with magnetic moment μ, the angular distribution function with respect to the magnetic field direction is

$$f(\theta,\alpha) = \frac{\alpha \exp [\alpha \cos \theta] \sin \theta}{2 \sinh \theta} \qquad \text{(II.2)}$$

where $\alpha = \mu H/k_B T$. Here

$$\begin{aligned} \langle P_2 (\cos \theta) \rangle &= \int P_2 (\cos \theta)\ f\ (\theta, \alpha)\ d\ \theta \\ &= 1 - \frac{3 \cos \alpha}{\alpha} + 3/\alpha^2. \end{aligned} \qquad \text{(II.3)}$$

Therefore

$$\Delta n = \Delta n_o \left[1 - \frac{3 \coth \alpha}{\alpha} + 3/\alpha^2 \right] \qquad \text{(II.4)}$$

where $\Delta n_o = N\Delta pV$. Since $\langle P_2 (\cos \theta) \rangle \rightarrow 1$ in the limit $\mu H \gg k_B T$, Δn saturates at Δn_o.

Measurements of the magnetically induced birefringence of the glutaraldehyde-fixed cells in suspension as a function of magnetic field are shown in Figure II7. The data were fit with the Langevin theory (Eq. II.4) modified to take a Gaussian distribution of cellular moments about the average value into account. The average value was 2.4×10^{-13} emu and the

standard deviation was 8.2×10^{-14} emu. Using an electron micrograph (Fig. II.8) to estimate the volume of Fe_3O_4 per magnetosome, and using the known value of 470 emu per cubic centimeter for Fe_3O_4, we get an average of 7-8 magnetosomes per bacterium in the sample.

Measurements of the average orientation of cells in suspension as a function of magnetic field at 300 K were also attempted with a SQUID magnetometer. The total magnetization approaches saturation for fields above 10 Oe, as expected for an array of permanent magnetic dipoles with moments of the order of 10^{-12} emu. We originally hoped to measure the initial susceptibility between 0 and 5 Oe, but trapped flux in the superconducting magnet in the system below 5 Oe made the measurements unreliable.

However, measurements were made on the suspension of cells after freezing in an applied field in the magnetometer. By following the moment with temperature during the cooling process, it was determined that the suspension froze below 265 K. The freezing process itself was found to disrupt the alignment of the cells to an extent that depended on the applied field. At 100 Oe, the orientation decreased to about 60% of the saturation value. At 900 Oe, the orientation decreased to 95% of the saturation value. Using this sample the complete hysteresis loop was determined as shown in Figure II9. From these data, $H_C = 285$ and $M_R.M_s = 0.67$, values consistent with vsm data on freeze-dried cells. This increase in M_R/M_s over the randomly oriented samples (theoretical value for $M_R/M_s = 0.5$) is consistent with the SW theory for partially ordered samples (II1).

3. Oriented Samples

Partially oriented samples of cells were prepared by drying suspensions

of the gluteraldehyde-fixed cells onto mylar film substrates in the presence of an intense magnetic field $\vec{H}_d$ as high as 150 kOe. Two orientationns of H_d relative to the direction normal to the film plane $\vec{n}$ were used: S1) $\vec{H}_d$ oriented $\perp$ to the film ($\vec{H}_d \parallel \vec{n}$); S2) $\vec{H}_d$ oriented in the film plane ($\vec{H}_d \perp \vec{n}$). After the drying process was complete, the films were removed from the field. Hysteresis loops were subsequently determined for several orientations of the measuring field H_o. For sample S1, loops were determined with H_o normal to the plane of the film ($\vec{H}_o \parallel \vec{H}_d$, $\vec{H}_o \parallel \vec{n}$) and in the plane of the film ($\vec{H}_o \perp \vec{H}_d$, $\vec{H}_o \perp \vec{n}$). For sample S2, loops were determined with $\vec{H}_o \perp \vec{H}_d$, $\vec{H}_o \perp \vec{n}$), and two orthogonal directions in the plane of the film, viz. ($\vec{H}_o \parallel \vec{H}_d$, $\vec{H}_o \perp \vec{n}$) and ($\vec{H}_o \perp \vec{H}_d$, $\vec{H}_o \perp \vec{n}$). A third sample, S3, was prepared with $\vec{H}_d = 0$.

Magnetization data for S2 is presented in Figure II10. The results for all samples are sumarized in Table I. Alignment of the bacterial magnetic moments in the plane of the film (sample S2) was high, as evidenced by the high M_R/M_s ratio for $\vec{H}_o \parallel \vec{H}_d$ and low ratios for both orientations of $\vec{H}_o \perp \vec{H}_d$ ($\vec{H}_o \perp \vec{n}$, and $\vec{H}_o \parallel \vec{n}$). On the other hand, alignment of cells perpendicular to the film (sample S1) was not great. For comparison, in S3 there is evidence for preferential alignment of the bacterial magnetic moments in the plane of the film. This suggests that surface tension tends to pull the long axes of the cells into the plane during the drying process. When $\vec{H}_d \parallel \vec{n}$, the tendency for moments to orient along H_d competes with the surface tension effect and the distribution of moments tends toward isotropy. For $\vec{H}_d \perp \vec{n}$, the magnetic and surface tension forces reinforce each other and high alignment in the plane of the film is achieved. In contrast, the freezing of cells in water in the presence of a strong

TABLE II-1: Magnetic Parameters for partially oriented magnetotactic bacteria as mylar substrates

Sample	Alignment Field	Measuring Field	M_r/M_s	H_c
S1	$H_d \parallel \vec{n}$	$\parallel \vec{n}$	.36	250
		$\perp \vec{n}$	.58	275
S2	$\vec{H}_d \perp \vec{n}$	$\parallel \vec{n}$	.58	112
		$\parallel \vec{H}_d$	.87	287
		$\perp \vec{H}_d, \vec{n}$	.31	250
S3	$H_d \perp \vec{n}$	$\parallel \vec{n}$	.10	125
		$\perp \vec{n}s$	.58	312
S4	$H_d = 0$	$\perp \vec{n}$	.41	37
σ-Fe_2O_3		$\parallel \vec{n}$	.26	167
		$\perp \vec{n}$	.88	297

magnetizing field produces substantial alignment because the surface tension forces attributible to the drying process is not present.

The data for the sample S2 with the moments highly oriented in the plane of the film can be compared with magnetic data for gamma-Fe_2O_3 magnetic tape (Fig. II.11). In the latter, elongated gamma-Fe_2O_3 particles with dimensions comparable to the bacterial magnetosome chain are oriented in the plane of the tape. The results (Table I) show that the magnetic properties of the magnetosome chains are entirely comparable to the elongated gamma Fe_2O_3 particles. This indicates that the magnetic properties of the magnetosome chain are those of an elongated single-magnetic-domain dominated by shape anisotropy. Conversely, one can argue that the magnetization reversal process of moments in the magnetic tape is similar to that in the magnetosome chain, namely, incoherent reversal of the Jacobs-Bean type (II6).

4. Separated Magnetosomes

In addition to magnetic measurements on whole cells, measurements were also made on isolated magnetosome chains and chain fragments obtained by disruption of whole cells followed by magnetic separation of the magnetosome chains from the non-magnetic cell debris. The separated magnetosomes were dried down on a mylar film (S4) with the orienting field $\vec{H}_d = 0$ presented in Table II-I. Compared to the whole cells, the saturation magnetic moment per gram is higher as expected, and the coercive force is lower. This result can be explained in terms of the clumping of the magnetosome chains following separation from the enveloping cellular material, resulting in higher chain-chain magnetic interactions that lower the magnetic anisotropy

TABLE II-2: Coercivities and coercivity distribution parameters for dispersed magnetotactic bacteria.

Coercivity (kAm^{-1})	M-1	M-2
H_c	21.36	2.96
H_r	22.08	13.28
H_r'	22.00	17.92
$H_{\frac{1}{2}irm}$	25.76	7.20
$H_{\frac{1}{2}arm}$	26.96	9.84
$(H_1/H_2)_{irm}$ [a]	0.530	0.358
$(H_1/H_2)_{irm}$ [b]	0.500	0.192
$(H_1/H_2)_{irm}$ [c]	0.541	0.167
$(H_1/H_2)_{arm}$ [d]	0.550	0.298

[a] distribution parameters for IRM acquisition

[b] distribution parameters for DC demagnetization of SIRM

[c] distribution parameters for AF demagnetization of SIRM

[d] distribution parameters for AF demagnetization of 0.04 kAm^{-1} ARM

and hence the coercive force and M_R/M_s ratio. Further magnetic properties of the separated magnetosomes are presented below.

C. REMANENCE

1. Remanence Curves and Coercivity Estimates

Remanence curves and their coercive forces are given by the following notation. All remanence curves have been normalized with respect to saturation remanence. IRM acquisition and dc demagnetization curves are denoted by $J_{ir}(H)$ and $J_d(H)$ respectively. The remanent coercive force, H_r, is the reverse dc field necessary to reduce an initial SIRM to zero. The complement to this is H_r', which is the dc field at which $J_{ir}(H)$ is 0.5. Normalized AF demagnetization curves of SIRM or ARM are denoted by $J_{ir}(\tilde{H})$, where $\tilde{H}$ is the peak alternating field. The median destructive field, $\tilde{H}_{\frac{1}{2}}$, is the AF necessary to reduce an initial remanence by half. Moreover, to estimate the spectral widths of the coercivity distributions sampled by the various remanences, let H_1 and H_2 be the fields at which the normalized intensity is respectively 15% and 85% of saturation.

For an ensemble of non-interacting, single-domain grains, Wohlfarth [II7] has shown that the following relationships hold between the different RM curves:

$$J_d(H) = 1 - 2\,J_{ir}(H) \qquad \text{(II.5a)}$$

$$J_{ir}(H) = \tfrac{1}{2}[1 + J_d(H)] = d(h) \qquad \text{(II.5b)}$$

$$J_{ir}(\tilde{H}) = 1 - J_{ir}'(H) = r(h) \qquad \text{(II.5c)}$$

These relations also imply that $H_{\frac{1}{2}} = H_r = H_r'$ and on a plot of $J_{ir}(H)$ and $J_{ir}'(H)$, the crossover point occurs at a value, R, of 0.5 (II7 - II12).

Particle interactions, however, will tend to offset the coercivity spectra of the different RM curves; as a result, relations (II.5a-c) will

not be satisfied [e.g., (II7-II12)]. Instead, Kneller II12 proposed that the effects of particle interactions will produce two types of magnetic behavior with respect to relations (II.5a-c). Type I materials are characterized by $J_{ir}(H) < d(H) < r(H)$, $d(H) = \frac{1}{2}[J_{ir}(H) + r(H)]$, $R < 0.5$, and $H_{\frac{1}{2}} < H_r < H'_r$. Type II materials, in contrast, are characterized by $J_{ir}(H) > d(H) > r(H)$, $R > 0.5$, and $H_{\frac{1}{2}} > H_r > H'_r$. Solidified suspensions of SD particles, in which agglomeration of particles occur, are typical type I materials; SD precipitates in a non-magnetic matrix, in which minimal, or no, agglomeration takes place, are typical type II materials [II12]. As will be shown subsequently, samples M-1 and M-2 displayed prototypical type II and type I behavior respectively.

2. Acquisition and Demagnetization of IRM

Normalized RM curves of $J_{ir}(H)$ and $J_{ir}(\tilde{H})$ for M-1 and M-2 are shown in Fig. II12a,b. Both samples saturated by 600 G and the acquisition curves were similar in form. Coercivities and spectral paramters are given in Table II-2 and indicated that sample M-1 had a slightly narrower coercivity spectrum and approached saturation at a slightly faster rate than M-2.

The most drastic differences between these samples, however, were observed during AF demagnetization of SIRM (Fig. II13). Here, M-2 had a much broader spectral width, decayed much faster with H, and complete demagnetization occured at approximately 300 G, as compared to, 600 G for M-1. The decrease in R from 0.620 to 0.215 and the general shift to higher coercivities for acquisition, and lower coercivities for demagnetization (see Table II2) suggested that grain-grain, or chain-chain interaction effects were more pronounced in M-2 than in M-1.

The difference in demagnetization characteristics between M-1 and M-2 was demonstrated further when remanence data were plotted in terms of $J_{ir}(H)$, according to relations (II.5a-c). These results indicated that M-1 and M-2 exhibited characteristic type II and type I behavior, respectively. Agglomeration of particles were likely to occur in M-2 because the extracted magnetosomes were no longer separated by the cell membrane of the bacterium; hence the individual chains were now closer together in the freeze-dried powder. This would explain its type I behavior. On the other hand, the individual chains were still intact within the bacterium in M-1 and therefore agglomeration of the chains would be considerably reduced. This reduction in agglomeration was apparently sufficient to produce type II behavior. Yet, chain-chain interactions must still be present, to some degree, in M-1; otherwise, the remanence curves would be described exactly by the Wohlfarth relations. The effects of interactions were investigated further with ARM in the following section.

3. Anhysteretic Remanent Magnetization

The acquisition of weak-field ARM/SIRM for both samples are shown in Fig. II14 and show that the approach to saturation was much more rapid in M-1 than in M-2. Anhysteretic susceptibilities (actually x_{arm}/SIRM) were 2.675 $(kA/m)^{-1}$ and 0.125 $(kA/m)^{-1}$, for M-1 and M-2 respectively. It is well known that particle interactions are responsible for finite values of x_{arm} (II12); furthermore, type I materials have $x_{arm}^{-1} > 0$ while type II materials have $x_{arm}^{-1} = 0$ (II12). Even though M-1 had a finite value of x_{arm}, the observed x_{arm} values for M-2 and M-1 were quantitatively consistent with type I and II behavior.

In order to relate x_{arm} values to particle interaction fields, Jaep's

theory (II13) of ARM for interacting SD grains was used. In brief, the ARM equation for interacting grains, derived in (II13), is

$$p_{arm} = \tanh \left[M_s/kT \left\{ (1-\bar{H}_a/H_r)h_{dc} - \lambda p_{arm} \right\} \right] \qquad (II.6)$$

where p_{arm} = ARM/SIRM, $\bar{H}_a$ is the value of the AF when the ARM converges to its equilibrium value, h_{dc} is the dc inducing field, and λ is the interaction field parameter. The term $(1 - \bar{H}_a/H_r)$ can be approximated by $B = M_{sb}/M_s \ (T/T_b)^{1/2}$ (II13), where the subscript b refers to the value of the parameter at the thermal blocking temperature. The small argument expansion of the tanh function yields

$$p_{arm} = Bh_{dc}/(kT/M_s + \lambda) \qquad (II.7)$$

The parameter B cannot be determined for the bacterial magnetite samples because of the adverse chemical changes which would be produced by heating the samples close to the Curie temperature of magnetite; therefore λ cannot be obtained directly. However, an order of magnitude estimate of B, and thus λ, can be obtained as follows. We assume that T_b varied discreetly between 500° and 575°C and that $M_s \propto (T - T_c)^{0.4}$ for magnetite, near the Curie temperature. With these approximations, λ was found to vary between 0.0098 and 0.052 kAm^{-1} for M-1, and between 0.78 and 1.94 kAm^{-1} for M-2. Accroding to these calculations, the interactions fields were approximately 50 times greater in M-2 than in M-1. Furthermore, we can calculate an average distance between chains of particles (assuming a chain length of 10) that would be necessary to produce a field equal to λ. These calculations predicted that particle chains were 1-3 μm apart in M-1, while the particle chains were 0.3-0.4 μm apart in M-2. The former estimate was consistent with the average size of an individual bacterium and supported the contention that agglomeration effects may not be that significant in M-1.

The interaction field is also related to the volume fraction (p) of magnetite, where $p = (r/R)^3$, r = average particle size (42 nm) and R = average distance between particles (as determined by λ). The volume fraction calculated from the interaction field correspond closely to the observed volume fraction for M-1 (predicted = 0.926×10^{-5}, observed $\approx 1.29 \times 10^{-5}$). However, the correspondence was not as close for M-2 (predicted = 2.74×10^{-5}, observed $\approx 74.7 \times 10^{-5}$ and probably higher). In this case, the interaction fields may not necessarily depend on concentration in a simple fashion because of particle agglomeration.

4. Lowrie-Fuller Test

A commonly used procedure in rock magnetism is the Lowrie-Fuller test (II14), which compares the AF demagnetization spectra of a strong-field (IRM) to a weak field (ARM) remanence in order to make predictions about the domain state of the remanence carrying phase. In brief, weak-field ARM in SD and small MD particles exhibit more resistance to AF demagnetization than strong-field IRM, whereas large MD particles exhibit the opposite behavior (see II14 for a more complete discussion).

The results of the Lowrie-Fuller test for M-1 and M-2 are shown in Fig. II15 and predicted that the domain state was SD, as one would have suspected based on particle size. Our results can now be compared to results given in II15, which were obtained from deep-sea sediments in which biogenic magnetite was suspected of being present. Petersen et al. (II15) used $\Delta LF = H_{\frac{1}{2}arm} - H_{\frac{1}{2}irm}$, ARM/IRM, and $H_{\frac{1}{2}irm}$ values as a means to distinguish between biogenic SD magnetite from inorganic MD magnetite. These parameters, however, are more likely to distinguish any type of SD from MD particle. It

is only by inference that the presence of biogenic magnetite is suspected based on these magnetic measurements. Nevertheless, they found that some of their samples fell within a tight group (component A) with $\Delta LF = 3.6-5.6$ kAm^{-1}, ARM/IRM = 0.07 - 0.10, and $H_{\frac{1}{2}irm} = 9.2 - 12.0$ kAm^{-1}. These same samples were later found to contain magnetite particles with grain morphologies which were highly suggestive of a biogenic origin. However, our magnetic results were significantly different from those attributed to their A component. Specifically, we found that for M-1, $\Delta LF = 1.20$ kAm^{-1}, ARM/IRM = 0.005, and $H_{\frac{1}{2}irm} = 7.2$ kAm^{-1}.

There are a number of explanations for this discrepancy. First, we do not know if different species, or older species, of magnetotactic bacteria would exhibit slightly different magnetic properties. Second, the fossil biogenic magnetite could conceivably act as individual particles, whereas in our samples they are still in chains. Third, the A component may not be totally due to biogenic magnetite, but could contain an inorganic SD contribution as well. For all these reasons, it is not too surprising that our results differ significantly from those in II15.

5. Viscous Remanent Magnetization

Differences in VRM behavior betwen M-1 and M-2 were quite dramatic. The viscous moments, which was acquired in a steady field of 0.40 kAm^{-1}, were approximately 0.08% (for M-1) and 0.76% (for M-2) of SIRM after only 16 hours. The zero field decay of VRM is shown in Figure II16. As determined by step-wise least squares regression, for times less than 16 hours, M-1 had a linear logarithmic decay (VRM $\propto$ log t), while M-2 had a cubic logarithmic decay [VRM $\propto (\log t)^3$].

Neel's (II16) SD theory for non-interacting particles predicts a log t

dependence; however, the logarithmic time dependence is commonly observed to be non-linear in many natural and analogue rock samples and in spin glasses (II17-II18). The reasons for this type of behavior are not clear; although, it has been suggested that particle interactions and the particle grain size distribution could be responsible (II18). Using a mean random field approach, Walton and Dunlop (II18) showed that the acquisition and decay of VRM should follow a polynomial log t dependence ($M \propto a_0 + a_1 (\log t) + a_3 (\log t)^3 + \cdots$). In the limit of zero interactions, the time dependence should be approximately linear in log t. This may be a reasonable explanation for our VRM results. As the IRM and ARM results suggested, particle interactions were much lower in M-1 than in M-2. Nevertheless, the $(\log t)^3$ behavior observed for M-2 was still unusual because the mean random field theory predicts that the linear and quadratic terms should be more dominant than the cubic term for the short duration of these experiments. Depending on the severity of particle agglomerations, the mean random field theory may not be a suitable approximation for particle interactions in M-2 and therefore could explain the difference between theory and the observed time dependence of VRM.

6. Comparison with synthetic sub-micron magnetites

The results of our experiments offer an excellent opportunity to compare the magnetic properties of bacterial magnetite to those obtained on comparable sized synthetic sub-micron magnetite. Invariably, all synthetic magnetite samples contain a range of particle sizes. Moreover, inhomogeneous dispersion and particle clumping in dilute concentrations means that interaction effects are probably prevalent. In order to

understand if certain variations of magnetic properties are produced by particle interactions or by particle size distributions, it is necessary to separate these two effects. In many cases this can be difficult, if not impossible. The narrow particle size distribution of the bacterial magnetite effectively removes this as a variable; hence, differences in magnetic properties between our samples should be due to interactions alone.

The sub-micron magnetite data have been taken from the rock magnetic literature (II8, II9) and include (1) chemically precipitated equidimensional particles, with grain sizes within the range of 25 to 220 nm and (2) acicular particles with axial ratios of 8:1 and 7:1 and dimensions of 30 x 200 nm and 40 x 3500 nm, respectively. The elongated particles have similar grain dimensions as the isolated particle chains in sample M-1. The data we chose to compare was based primarily on their availability in the literature and included ARM, SIRM, x_o, S_d, and coercivity. In addition to eliminate errors arising from uncertainties in the weight percentage of magnetite in our samples, ratios of magnetic parameters were used for comparisons. The ratios used and their responses to changes in grain size and particle interactions were as follows.

The ratios x_{arm}/x_o and $x_{arm}/SIRM$ are slightly dependent on grain size, but strongly dependent on particle interactions (II4,10,13,19,21). S_d/J_s varies inversely with grain size [$\propto d^{-(1-1.5)}$], within the submicron range. (II17-18). x_o/J_s is practically independent of grain size and for SD magnetite, $x_o/J_s \lesssim 8.75 \times 10^{-3}$ $(kA/m)^{-1}$ (II21); however, superparamagnetic (SP) particles can increase this ratio to an upper limit of ≈ 3.75 $(kA/m)^{-1}$ (II21). $SIRM/x_o$ varies between 1.5 to 50 kAm^{-1} as grain size decreases from tens of microns to submicron and samples with a high SP content can have

SIRM/x_o ratios below 0.01 kAm^{-1} (II21). Furthermore, particle interactions can increase x_o/J_s and decrease SIRM/x_o through their effects on x_o (II20). Parameter ratios are summarized in Table II-3 and coercivities are summarized in Table II-4.

7. Parameter Ratios

Particle (or chain-chain) interactions should have a pronounced effect on the ratio x_{arm}/x_o and x_{arm}/SIRM with x_{arm} decreasing and x_o increasing with increasing concentration or packing factor (e.g., II12, II20). The results for M-2 had characteristic values similar to, but slightly lower than, those for the synthetic cubic magnetites. The ratios for M-1, however, were at least an order of magnitude than those for cubic magnetite, and 4-10 times higher than those for the acicular magnetite. If *interactions, presumably due to agglomeration effects, are responsible* for these low values in M-2, then these data also suggest that interactions effects are probably prevalent in both the cubic and acicular magnetite samples -- a result that has been suggested many times before (e.g. II19, II21). This is supported further by the observation that, in all cases where experimental data exists, the synthetic magnetites exhibit type I behavior (II8, II9). It was interesting to note, however, that the volume concentration in M-2 was significantly greater than that reported for the synthetic magnetites (usually less than 1% by volume) and this could indicated that acicular magnetite was not a good analog for ARM in M-1. Particle agglomeration in the acicular samples is probably partly responsible for this descrepancy. In other words, the much higher values observed for M-1 were undoubtedly related to the reduced effects of agglomerations. This result is consistent with its type II behavior.

TABLE III: Comparison of observed magnetic parameters for bacterial magnetic with data from synthetic sub-micron cubic and acicular magnetites.

parameter	M-1	M-2	cubic[a]	acicular[b]
x_{arm}/x_0	148.7	1.46	5.19-9.76	5.98-38.2
x_{arm}/SIRM ($1/kAm^{-1}$)	2.675	0.125	0.150-0.188	0.113
x_0/J_s ($x10^{-3}$)($1/kAm^{-1}$)	9.86	34.88	8.75	6.875
SIRM/x_0 (kAm^{-1})	55.58	11.73	32.08-51.68	53.12
S_d/J_s ($x10^{-4}$)	0.257	0.917	0.60	---
J_r/J_s	0.53	0.41	0.28	0.35-0.45

[a] values were interpolated for a grain size of 42 nm. Results were taken from [13].

[b] acicular magnetites were 30 x 200 nm (Dunlop [13]) and 40 x 350 nm (King, unpublished).

The x_o/J_s and $SIRM/x_o$ parameters had values that were similar for both the bacterial and synthetic magnetites. This suggested that there was a minimal contribution from SP particles at room temperature. However, it was observed that for M-2 the value of x_o/J_s was higher and $SIRM/x_o$ are probably responsible for these slight differences. In general, particle agglomerations can increase x_o two ways. First, the overall increase in particle interactions produced by agglomermations can increase x_o (II20). Second, particle agglomeration can cause the break down of long particle chains into shorter ones. This has the effect of producing a decrease in shape anisotropy, which would therefore cause an additional increase in x_o.

S_d/J_s values for both M-1 and M-2 were similar to those obtained on the synthetic magnetites, although there were no S_d/J_s was slightly lower for M-1 and slightly higher for M-2 than that observed for the cubic magnetites. Again, this may indicate the effects of particle interactions (II18); however, the effect appears to be slight.

8. Coercivity

Values of H_c, H_r', H_r, and $H_{\frac{1}{2}}$ for M-1 and M-2 and for the cubic and acicular magnetites are summarized in Table II-4. H_c and $H_{\frac{1}{2}}$ were significantly higher and H_r and H_r' were significantly lower than the cubic magnetic data predicted for sample M-1. In contrast, the acicular magnetite data had significantly higher values for coercivity than that observed for M-1. The coercivity results for M-2 were significantly lower than those observed for the synthetic magnetites. Increase particle agglomerations were most likely responsible for the much lower coercivities for M-2.

It has been suggested that fanning is the most likely reversal mode for

TABLE II-4: Comparison of observed coercivity for bacterial magnetites with data from synthetic cubic and acicular magnetites.

Coercivity (kAm^{-1})	M-1	M-2	cubic[a]	acicular[b]
H_c	21.36	2.96	17.04	24.4-35.04
H_r	22.08	13.08	30.72	40.4-48.0
H_r'	22.00	17.92	40.48	54.16
$H_{\frac{1}{2}irm}$	25.76	7.20	22.64	34.72
$H_{\frac{1}{2}arm}$	26.96	9.84	---	45.68

[a] values were interpolated for a grain size of 42 nm. Results were taken from [II-8].

[b] acicular magnetites were 30 x 200 nm [1], and 40 x 350 nm (King et al., [II-19]).

M-1. On the other hand, it is unlikely that fanning occurs in the equidimensional magnetites. Other incoherent reversal modes, such as curling, buckling, or even the passage of a metastable domain wall, could occur in these particles and result in higher nucleation fields (see II12), as is observed.

The acicular magnetite would appear to represent a better analog for predicting the coercivity of M-1. For magnetite, the fanning model predicts $H_r = 47.2\ kAm^{-1}$ for a random alignment of spherical particles in contact with one another. This estimate gives a reasonable fit to the observed values of the acicular samples (Table II-4), but is still twice as high as observed for M-1. However, it is known that the particles within the bacterial chain are not touching. This would reduce the coercivity by a factor of $(1 + \beta)^{-3}$, where β is the separation distance normalized to the particle's diameter.

9. Model Coercivity

The chain-of-spheres, or fanning, mechanism was originally developed to model the coercive force in elongated single domain grains (II6). This model would seem most ideal to describe the reversal mode in the bacterial magnetite (II22); furthermore, it would seem to be an even better approximation for magnetization reversal in the bacterial magnetite than in elongated single domain grains because of the unique linear arrangement of cubic-shaped particles in the former.

Model coercive force values can be readily obtained for magnetite using the results already determined for iron [Table 1 in (II6), (Fig. II17)]. In the original fanning calculations, the spheres were assumed to be touching. It is clear from photomicrographs that this is not the case for the

particles making up the chain in magnetotactic bacteria. To account for a finite separation distance, the model coercive forces must be reduced by an amount $(1 + \beta)^{-3}$, where $\beta = x/a$, a is the particle diameter, and x is the separation distance. This correction assumed that β was a constant along the chain length for an individual bacterium. Coercive force for randomly oriented chains as a function of β are plotted in Figure II17 for three different reversal models: (1) symmetric fanning (model A), where the magnitude of the angle of fanning is constant along the length of the chain; (2) non-symmetric fanning (model A'), where the angle of fanning is not constant; and (3) parallel rotation (model B) (see Fig. II6). In addition, the Stoner-Wohlfarth values for H_c due to shape and magnetocrystalline anisotropies are also included in Figure II6. The results of these calculations were as follows.

First, H_c increases continuously with chain length for both models A and B; whereas, in model A, H_c is nearly independent of chain length for n greater than 6 (II6). Second, the values of β needed to predict the observed coercive force for M-1 of 21.4 kAm^{-1} were (1) 0.253 for model A, (2) 0.37 - 0.46 for model A, and (3) 0.8 - 0.9 for model B. Models A and A' predicted values of β that were consistent with observation (x = 3 - 18 nm, $\beta \approx 0.07 - 0.43$). Model B, however, predicted β values that are too high and it therefore seems unlikely that coherent rotation controls the coercivity in M-1. Third, the Stoner-Wolhfarth values also predict coercivities which are either too low (magnetocrystalline), or too high (shape) to account for the observed coercive force. Finally, to account for the observed coercivity spectrum in M-1 (i.e., $H_1/H_2 \approx 1$), either a distribution in chain length (model A only), or a distribution of β (model A

or A'), or both, must be assumed.

D. REFERENCES

II1. E. C. Stoner and W. P. Wohlfarth, Trans. Roy. Soc. (Lond.) A240 (1948) 599.

II2. P. J. Flanders and S. Shtrikman, J. Appl. Phys. 33 (1962) 216.

II3. P. J. Flanders, J. Appl. Phys. 53 (1982) 2567.

II4. R. B. Frankel and R. P. Blakemore, J. Magn. Mater. 15-18 (1980) 1562.

II5. C. Rosenblatt, F. F. T. de Aranjo and R. B. Frankel, Bipophys. J. 40 (1986) 83-85.

II6. I. S. Jacobs and C P. Bean, Phys. Rev. 100 (1955) 1060.

II7. E. P. Wohlfarth, J. Appl. Phys. 29 (1958) 595.

II8. D. Dunlop, Earth Planet. Sci. Lett. 78 (1986) 288.

II9. S. Cisowski, Phys. Earth Planet. Int. 26 (1981) 56.

II10. P. Dankers, Geophys. J. Roy. Aston. Soc. 64 (1981) 447.

II11. G. W. D. Spratt, P. R. Bissell, and R. W. Chantrell, IEEE Trans. on Mag. MAG-22 (1986) 659.

II12. E. Kneller, Fine Particle Theory, in: Magnetism and Metallurgy, eds. A. E. Berkowitz and E. Kneller (Academic Press, NY, 1969).

II13. W. F. Jeap, J. Appl. Phys. 42 (1971) 6339. S. K. Banerjee and J. P. Mellema, Earth Planet. Sci. Lett. 23 (1974) 177.

II14. W. Lowrie and M. Fuller, J. Geophys. Res. 76 (1971) 6339. M. E. Bailey and D. J. Dunlop, Earth Planet. Sci. Lett. 63 (1983) 611.

II15. N. Petersen, T. von Dobeneck, and H. Vali, Nature 320 (1986) 611.

II16. L. Neel, Ann. Geophys. 5 (1949) 99.

II17. D. J. Dunlop, Geophys. J. Roy. Astron. Soc. 74 (1983) 667. B. M. Moskowitz, Geophys. J. Roy. Astron. Soc. 82 (1985) 143. R. V. Chamberlin, J. Appl. Phys. 57 (1985) 3377.

II18. D. Walton, Nature 286 (1980) 245. D. Walton and D. J. Dunlop, Solid State Commun. 53 (1985) 359.

II19. D. J. Dunlop, J. Geophys. Res. 78 (1973) 7602. D. J. Dunlop, M. E. Bailey, and M. F. Wescott-Lewis, Geochim. Cosmoschim. Acta. 39 (Suppl. 6) (1975) 3063. J. W. King, S. K. Banerjee, and J. Marvin, J.Geophys. Res. 88 (1983) 5911. D. J. Dunlop, J. Geophys. Res. 91 (1986) 9569.

II20. P. M. Davis, J. Appl. Phys. 51 (1980) 594.

II21. D. J. Dunlop, Phys. Earth Planet. Int. 26 (1981) 1. R. Thompson, J. Bloemendal, J. A. Dearing, F. Oldfield, T.A. Rummery, J. C. Stober, and G. M. Turner, Science 207 (1980) 481.

II22. C. R. Denham, R. P. Blakemore, and R. B. Frankel, IEEE Trans. on Mag. MAG-16 (1980) 1006.

II23. D. L. Balkwill, D. Maratea, and R. P. Blakemore, J. Bacteriol. 141 (1980) 1399.

B. FIGURE CAPTIONS

Figure II1: DC hysteresis loop for freeze-dried magnetic bacteria samples to = 600 Oe.

Figure II2: Hysteresis loop computed from the SW theory for a distribution of anisotropies showin in Figure II3. The calculation gives H_c = 135 Oe and M_R/M_s = 0.5.

Figure II3: DC hysteresis loop to ± 1200 Oe.

Figure II4: Anistropy field (H_A) distribution.

Figure II5: Hysteresis loop of stationary sample and initial magnetization curve of a spinning sample for determination of average anisotropy field.

Figure II6: Hysteresis loop to = 900 Oe for a suspension fo fixed cells in water frozen at 900 Oe.

Figure II7: Schematic representation of MIB apparatus. The field H is applied along the y axis and the fast (optic) axis of the Pockel's cells is along z. The polarization and analyzer are oriented along 2 (y + z) and 2 (y - z), respectively.

Figure II8: Relative birefringence as a function of magnetic field for glutaraldehyde-fixed cells in water suspension.

Figure II9: Electron micrograph of a magnetic bacterium from the sample used in the MIB measurements. The bar is 1 micron.

Figure II10: Hysteresis loops for samples oriented in the plane of the substrate (S2). The solid line and dashed line are for the measuring field parallel and perpendicular, respectively, to the orienting field direction.

Figure II11: Superposition of hysteresis loops for S1 (solid line) and γ-Fe_2O_3 (dashed line) with the measuring field parallel to the orienting field in both cases.

Figure II12: Normalized induced remanent magnetization (IRM) data (+) and AF demagnetization of saturation induced magnetization (SIRM) (□). (a) sample M-1; (b) sample M-2.

Figure II13: AF demagnetization of SIRM. Labelled quantities are defined in the text. (a) Sample M-1; (b) sample M-2.

Figure II14: Acquisition of weak-field ARM/SIRM for samples M-1, (□), and M-2 (+).

Figure II15: AF demagnetization of IRM (□) and ARM (+). (a) Sample M-1; (b) sample M-2. The Lowrie-Fuller orientation for SD and small MD particles is that weak-field ARM is more resistant to demagnetization than stron-field IRM.

Figure II16: Zero-field decay of viscous remanent magnetization (VRM) in samples M-1 (□) and M-2 (+).

Figure II17: Coercive force calculated for the chain of spheres model (Ref. II6), plotted versus interparticle separation for different chain lengths.

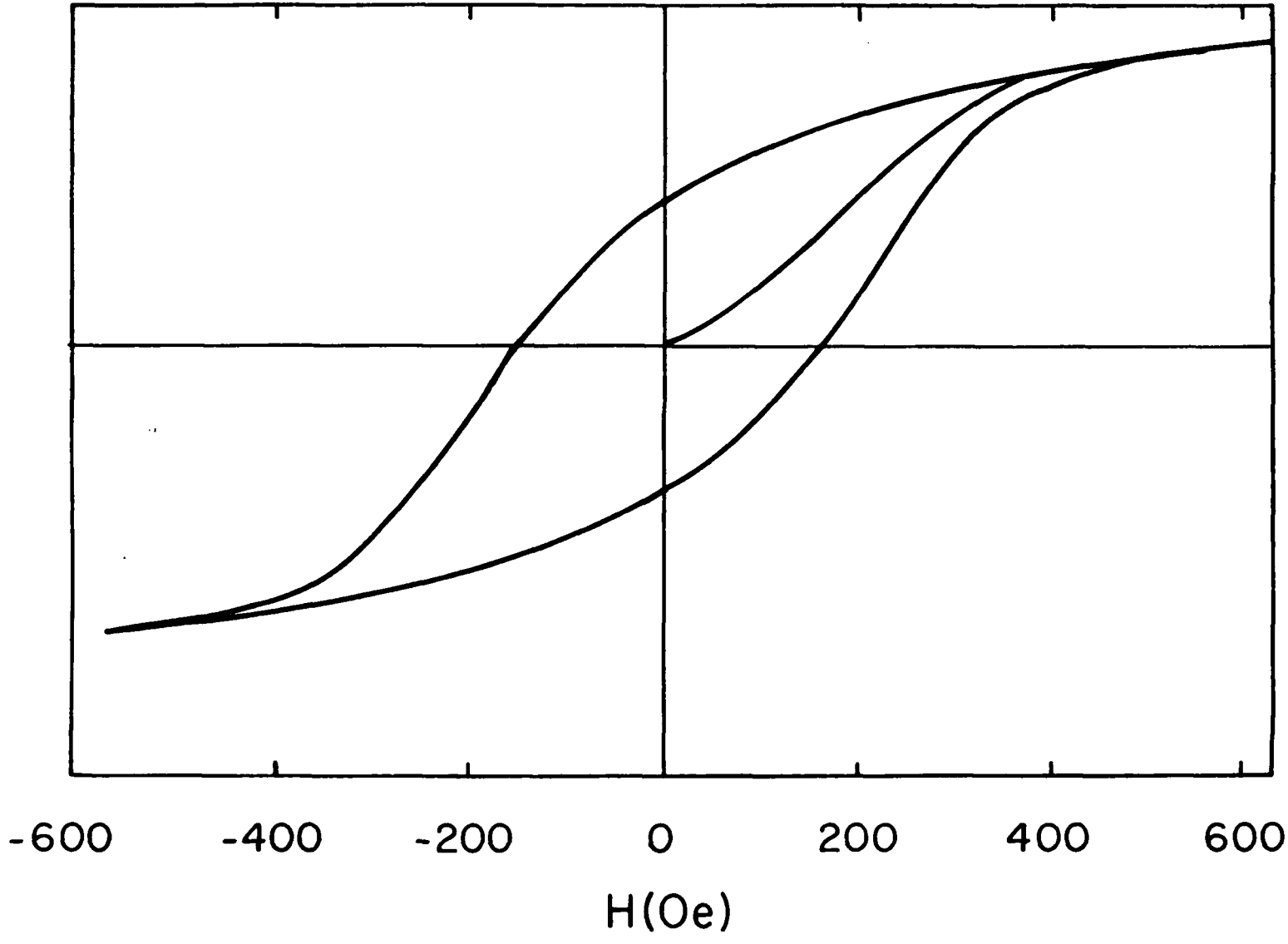
-600
-400
-200
0
200
400
600
H(Oe)

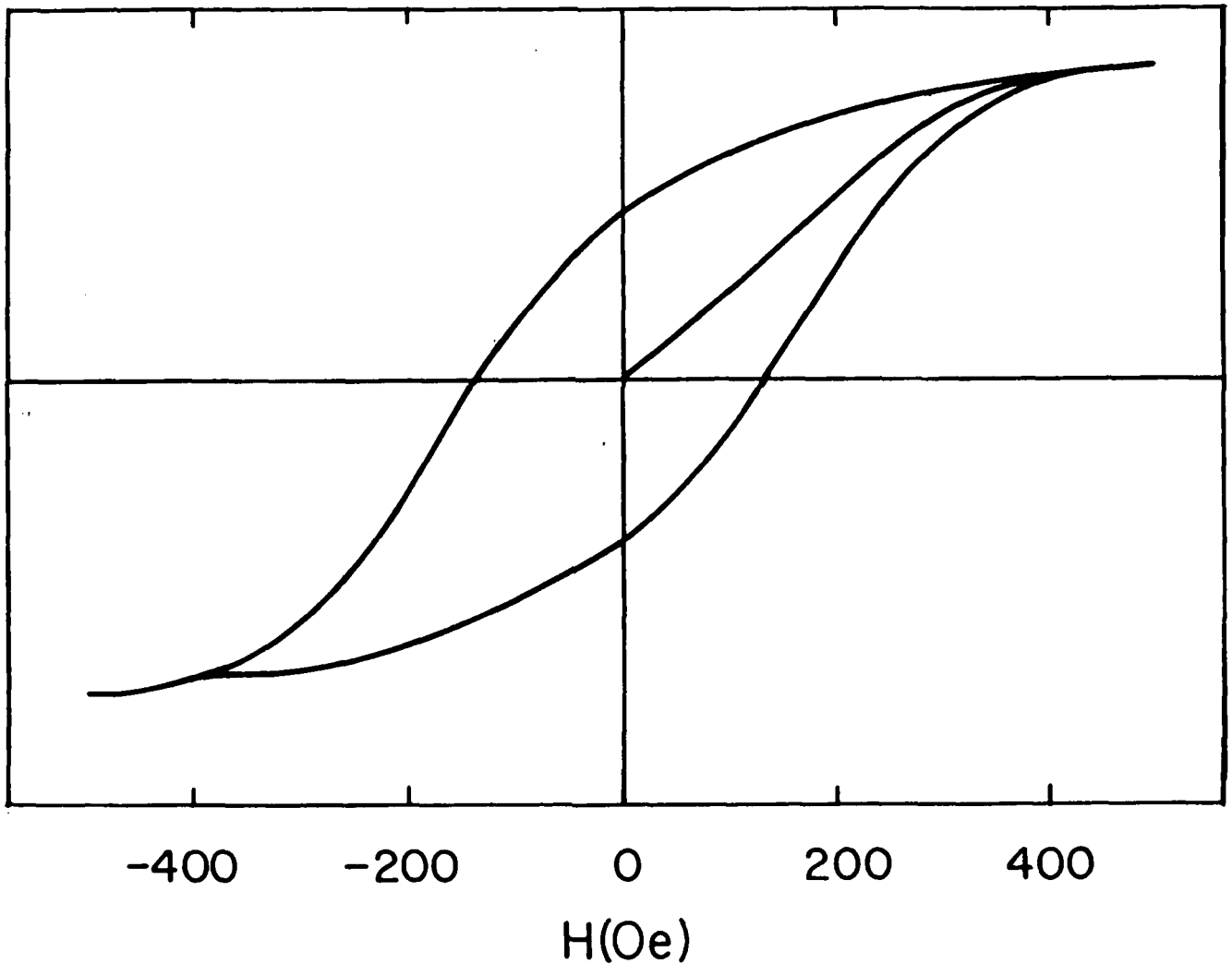
-400
-200
0
200
400
H(Oe)

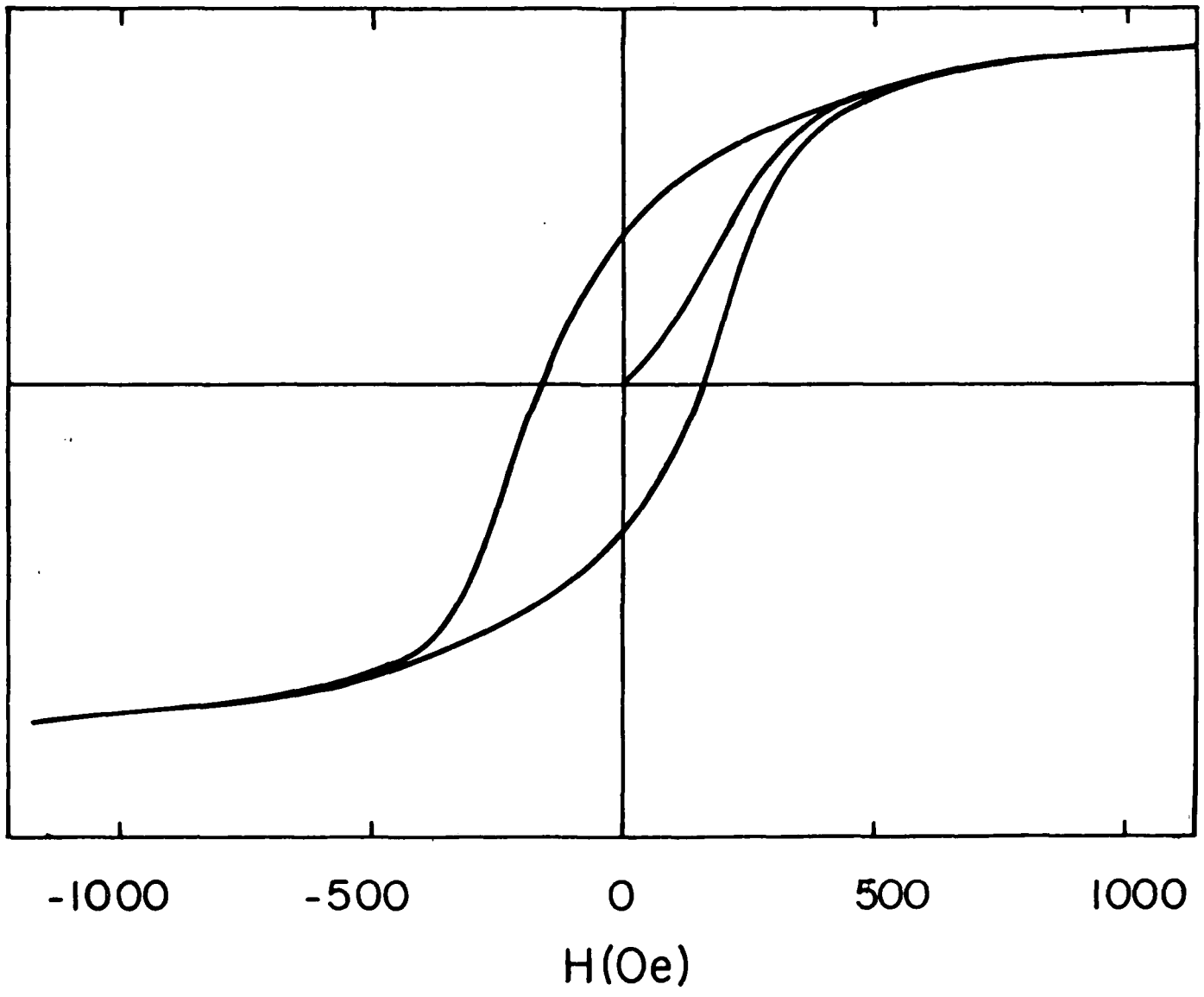
-1000
-500
0
500
1000
H(Oe)

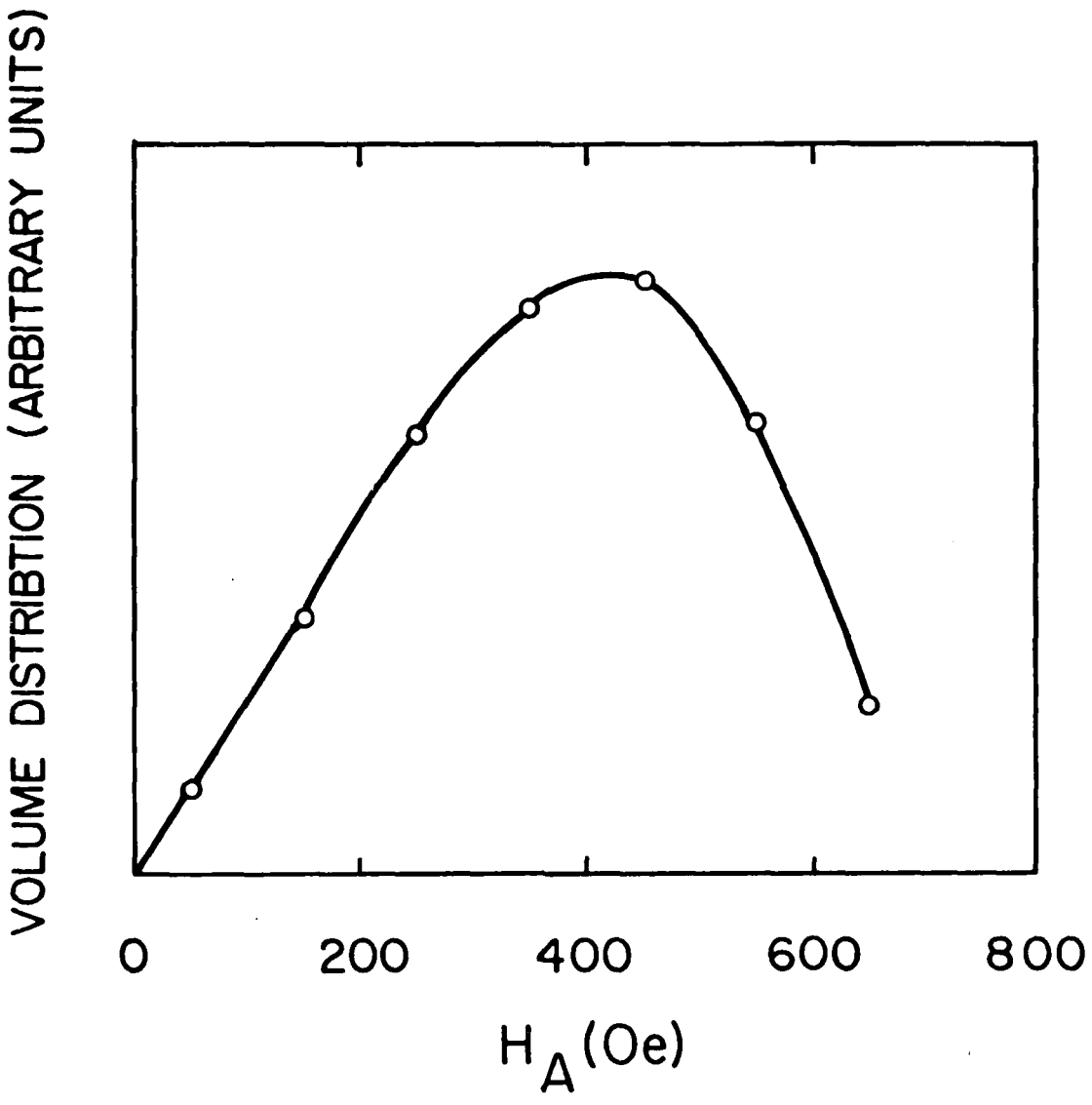
VOLUME DISTRIBTION (ARBITRARY UNITS)
0
200
400
600
800
H_A(Oe)

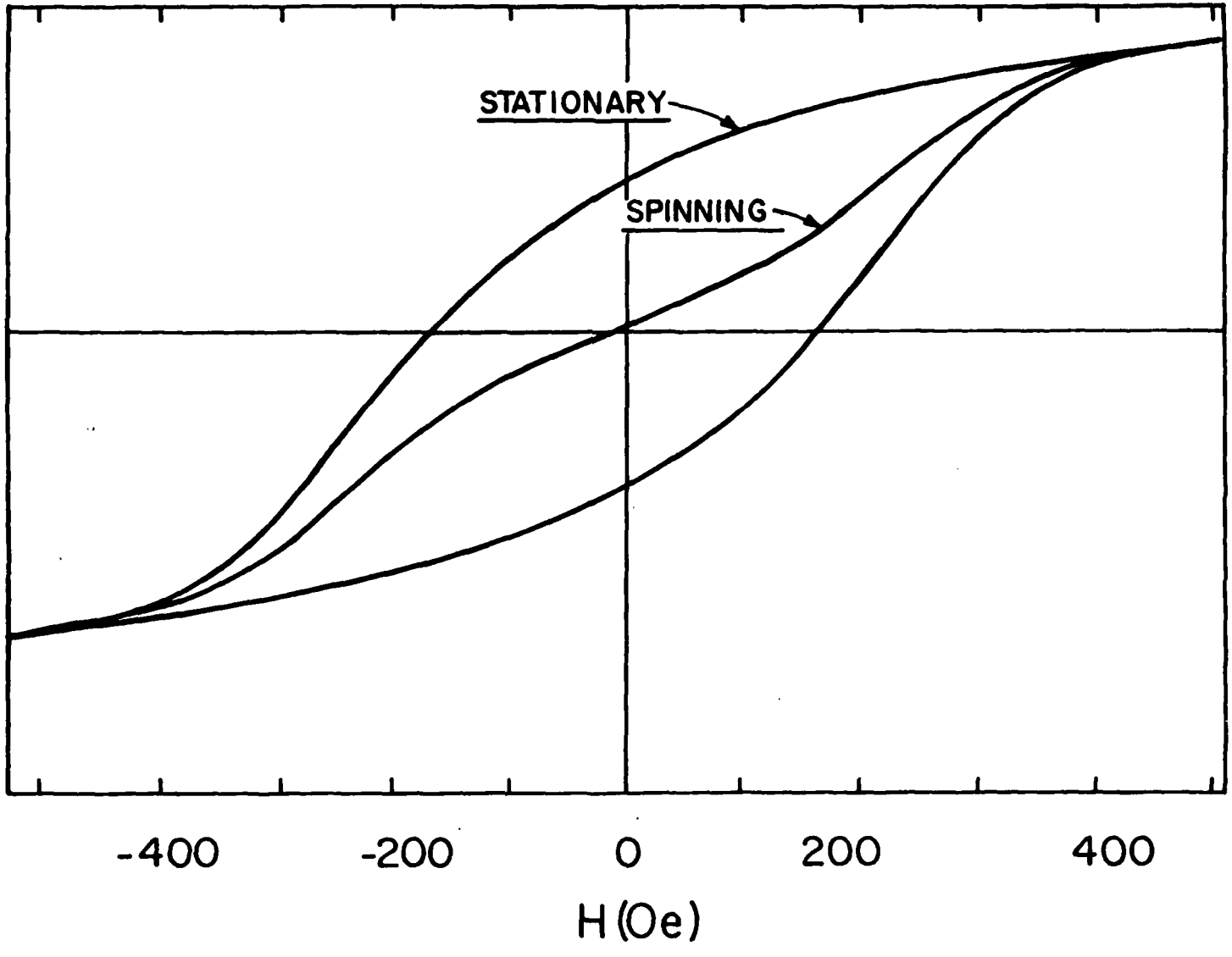
STATIONARY
SPINNING
-400
-200
0
200
400
H(Oe)

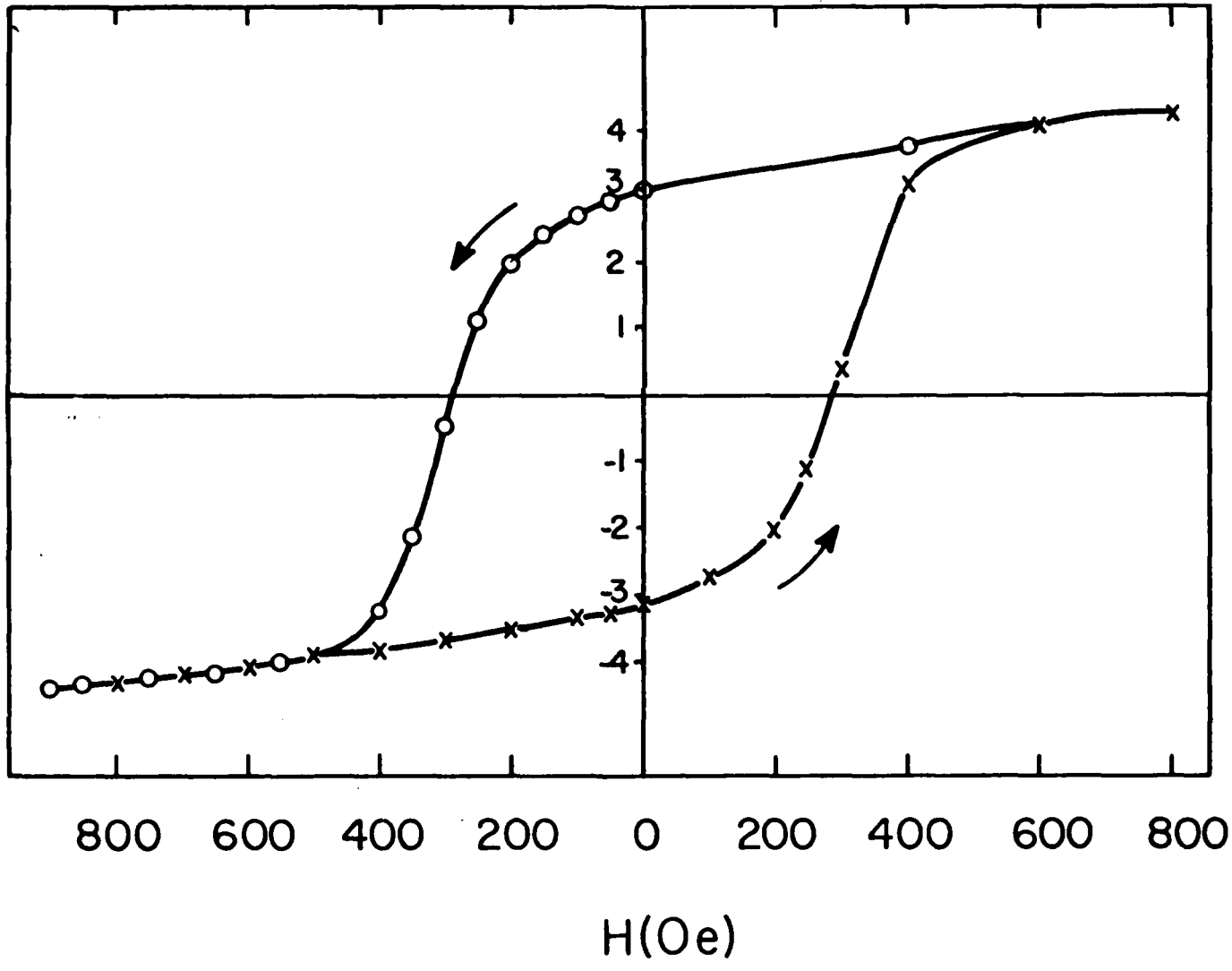
4
3
2
1
-1
-2
-3
-4
800
600
400
200
0
200
400
600
800
H(Oe)

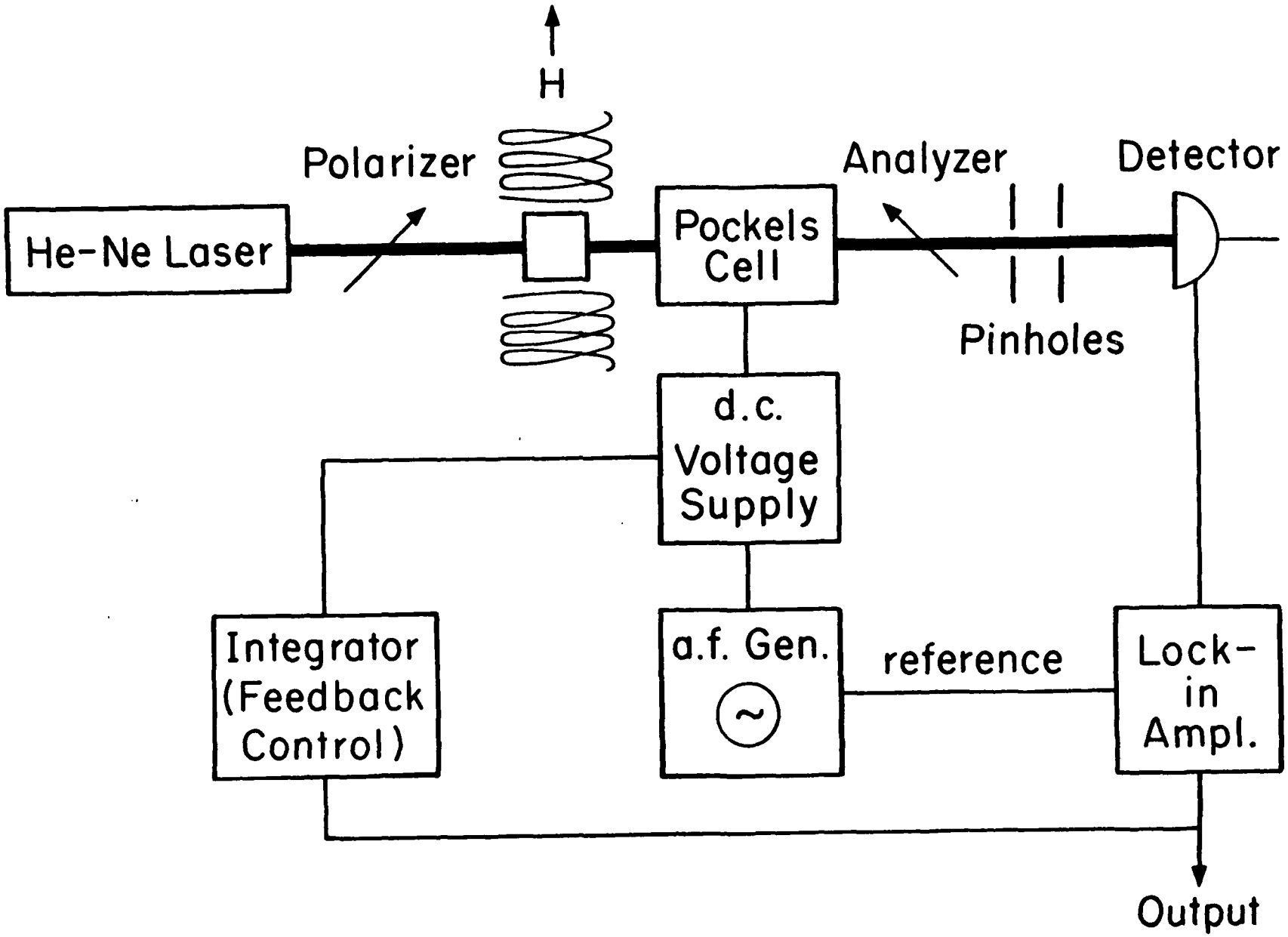
H
Polarizer
Analyzer
Detector
He-Ne Laser
Pockels Cell
Pinholes
d.c. Voltage Supply
Integrator (Feedback Control)
a.f. Gen.
reference
Lock-in Ampl.
Output

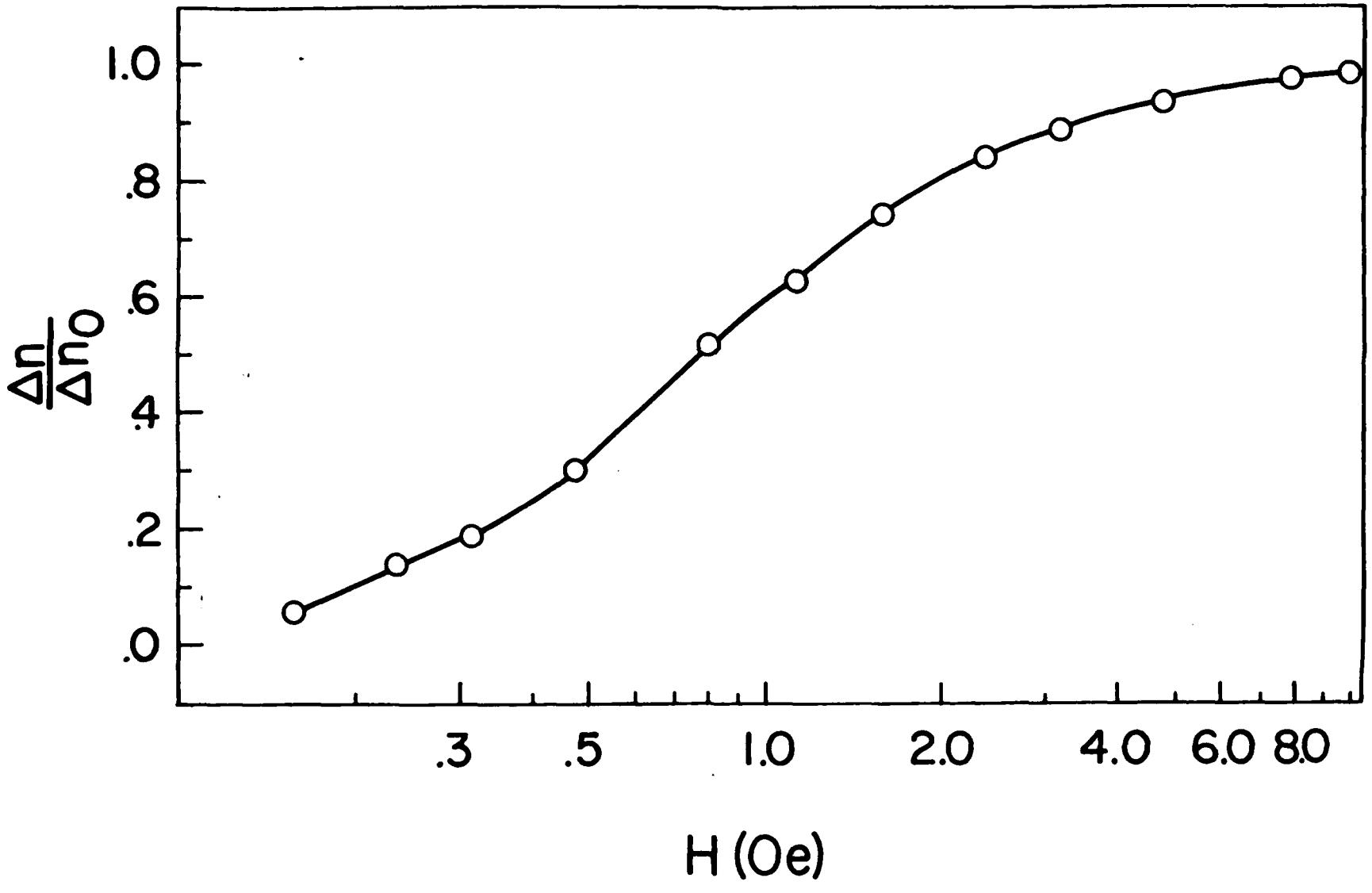
1.0
.8
.6
.4
.2
.0
Δn/Δno
.3
.5
1.0
2.0
4.0
6.0
8.0
H (Oe)

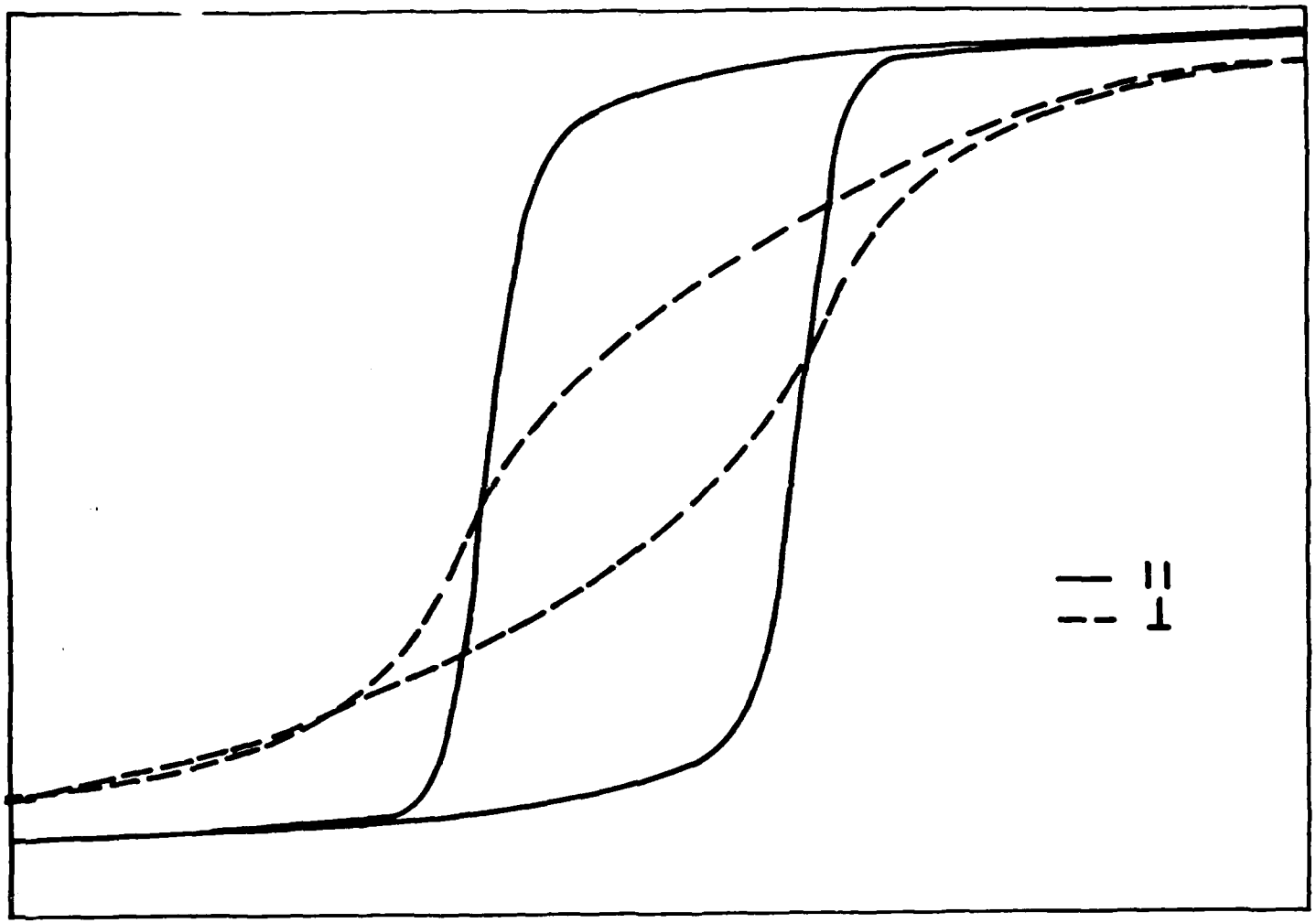
∥
⊥
H(100 Oe/cm)

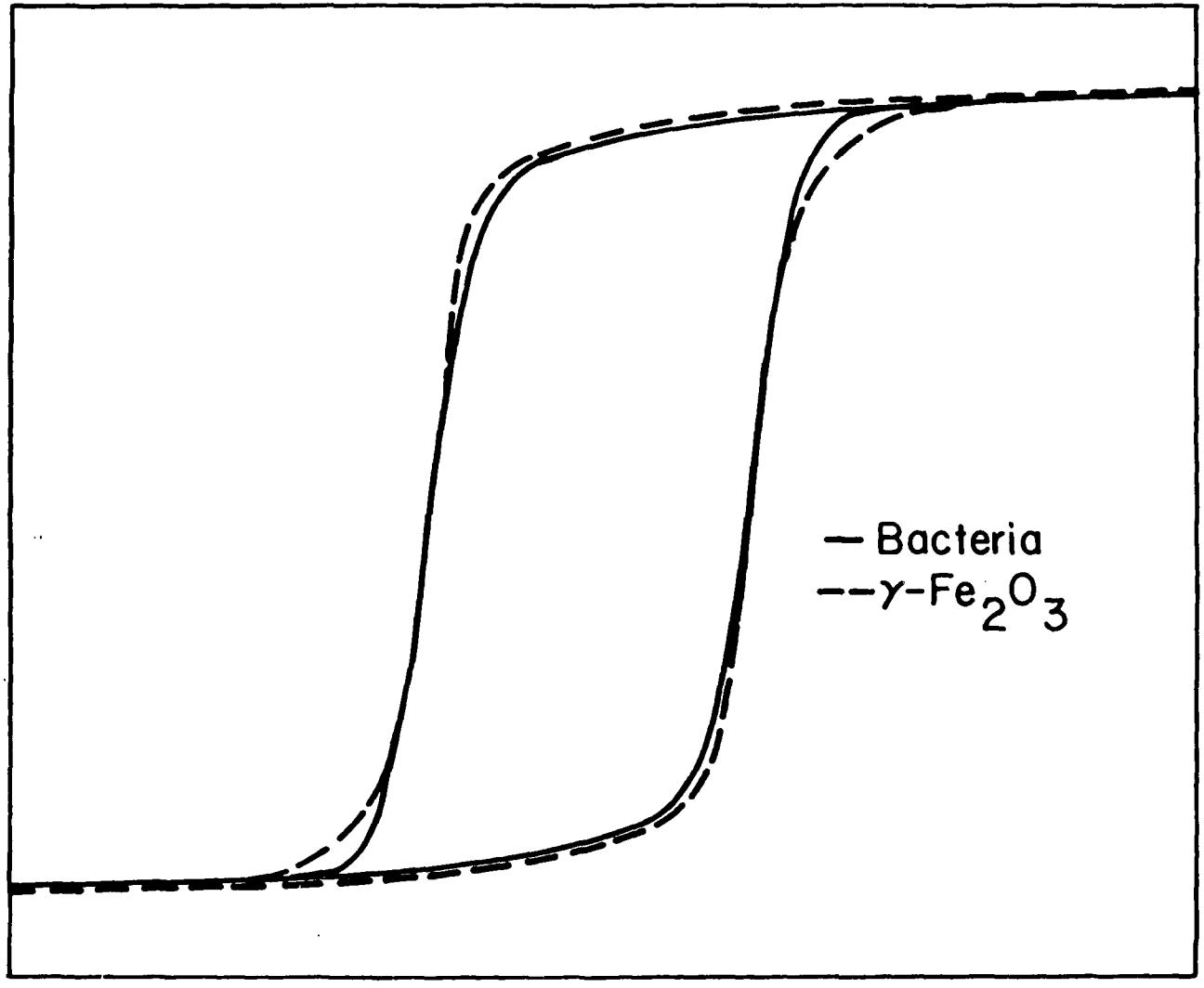
— Bacteria
--γ-Fe2O3
H (100 Oe/cm)

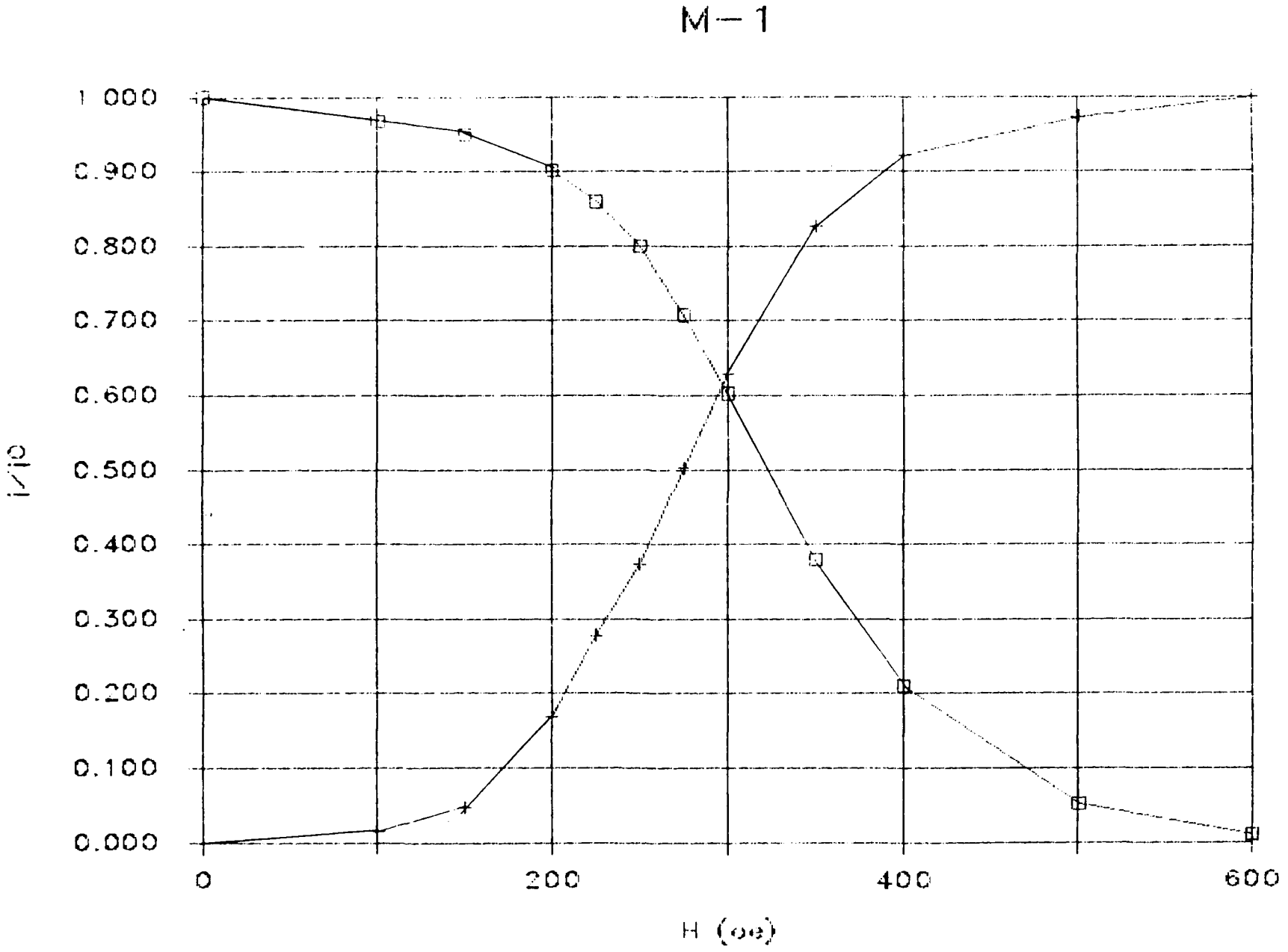
M－1
1.000
0.900
0.800
0.700
0.600
0.500
0.400
0.300
0.200
0.100
0.000
i/i0
0
200
400
600
H (oe)

II 12a

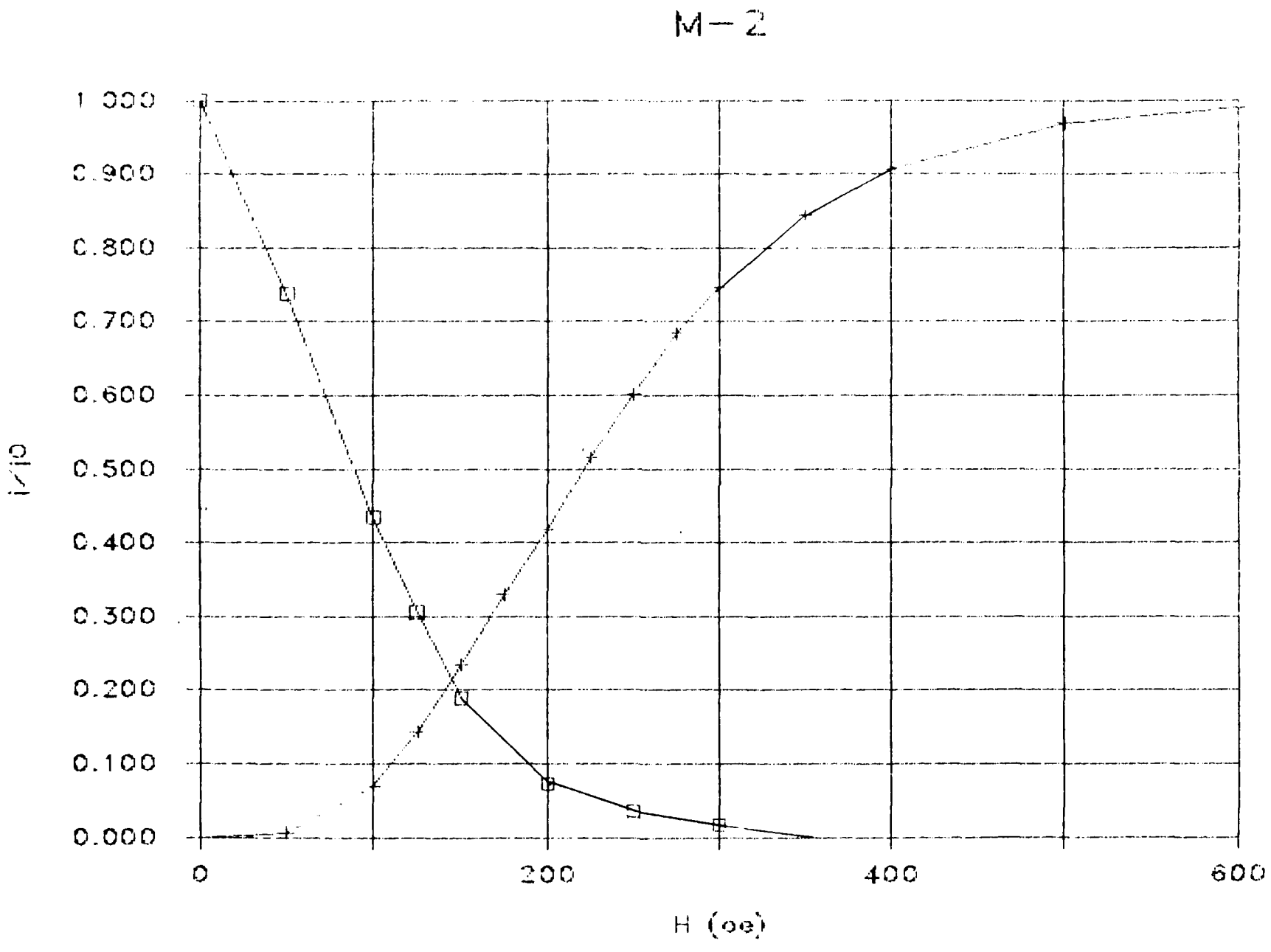
M－2
1.000
0.900
0.800
0.700
0.600
0.500
0.400
0.300
0.200
0.100
0.000
0
200
400
600
H (oe)

II 12b

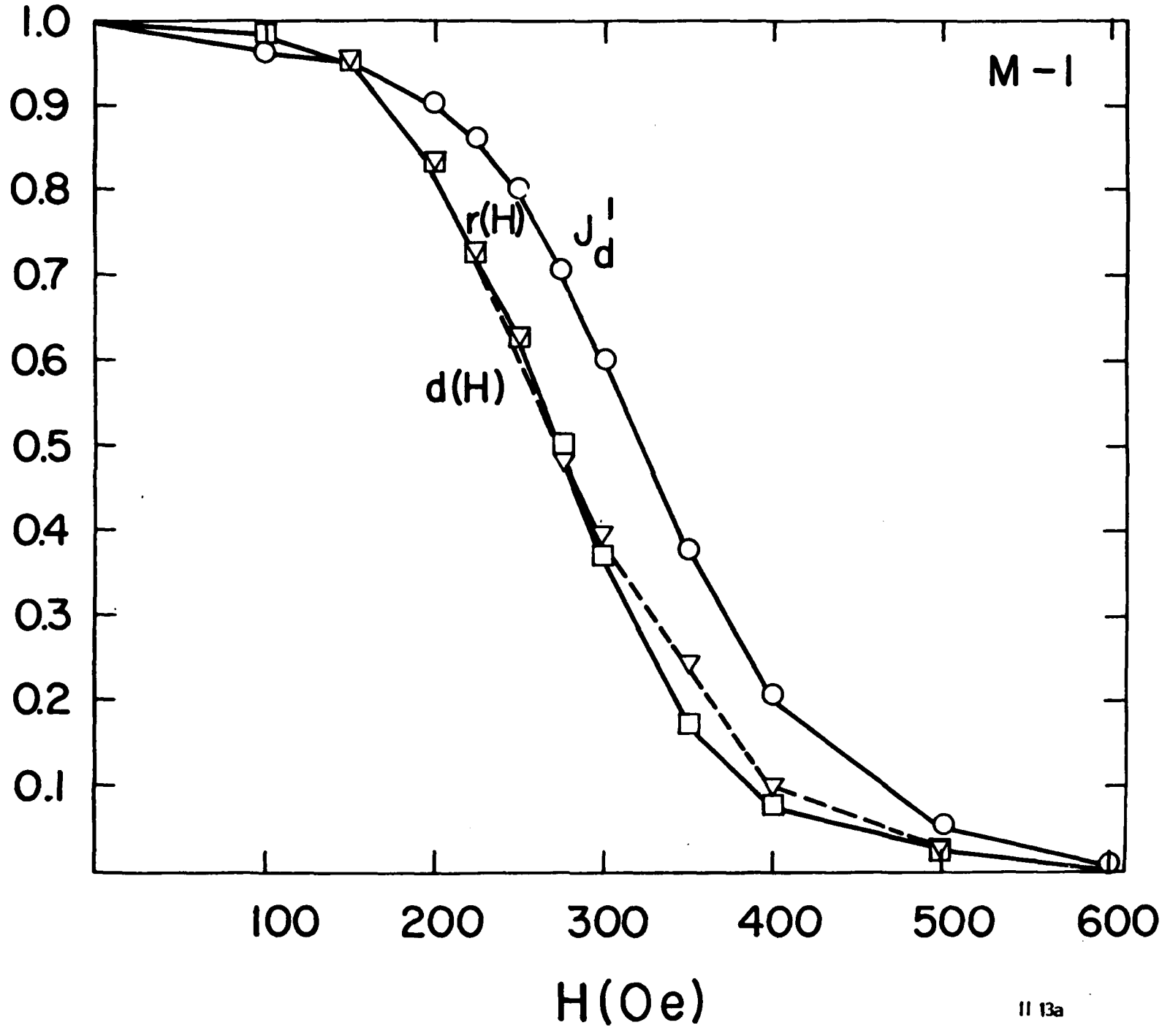
M-1
r(H)
J_d^I
d(H)
1.0
0.9
0.8
0.7
0.6
0.5
0.4
0.3
0.2
0.1
100
200
300
400
500
600
H(Oe)
II 13a

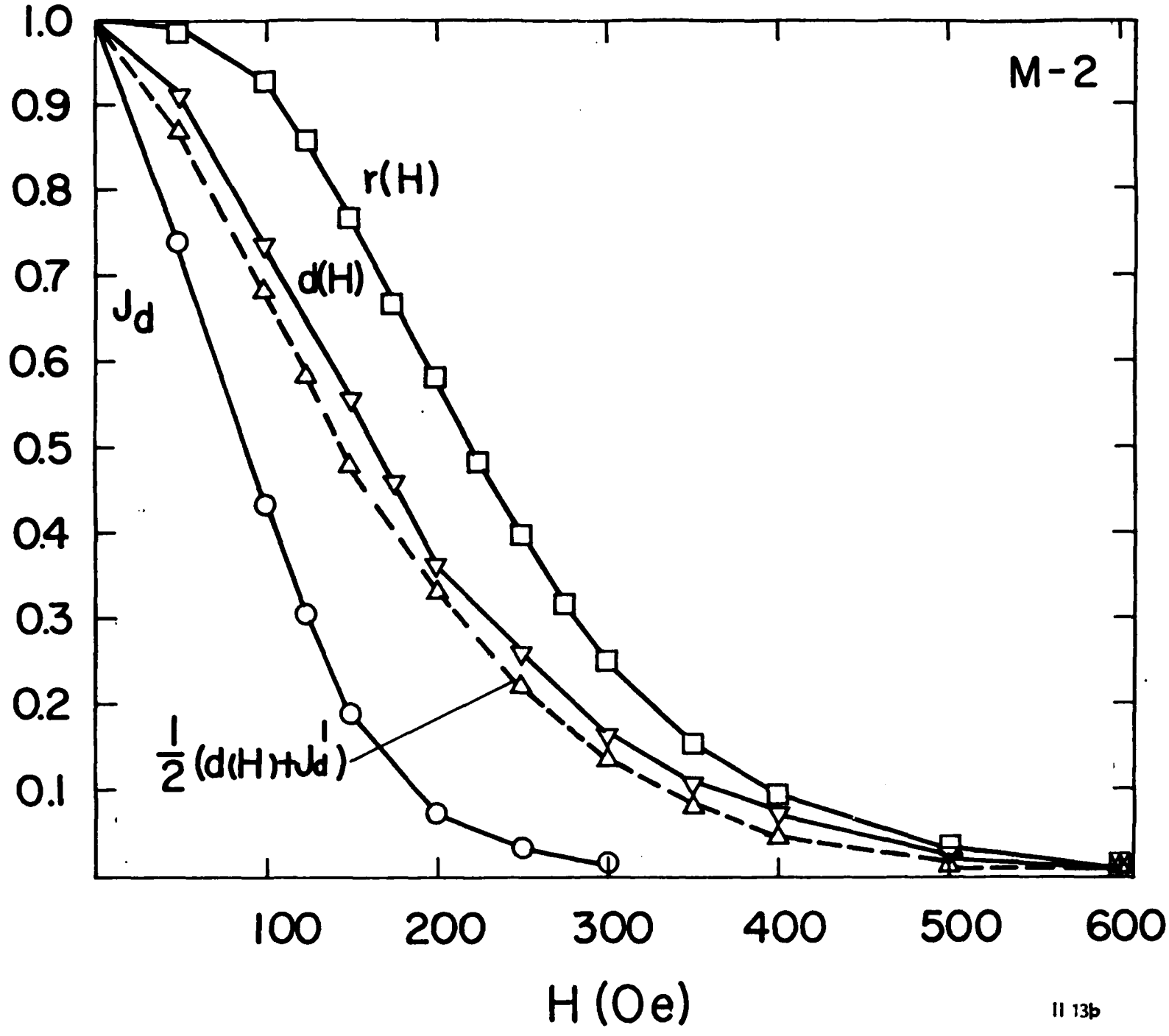
M-2
r(H)
d(H)
J_d
$\frac{1}{2}(d(H)+J_d)$
1.0
0.9
0.8
0.7
0.6
0.5
0.4
0.3
0.2
0.1
100
200
300
400
500
600
H (Oe)

II 13b

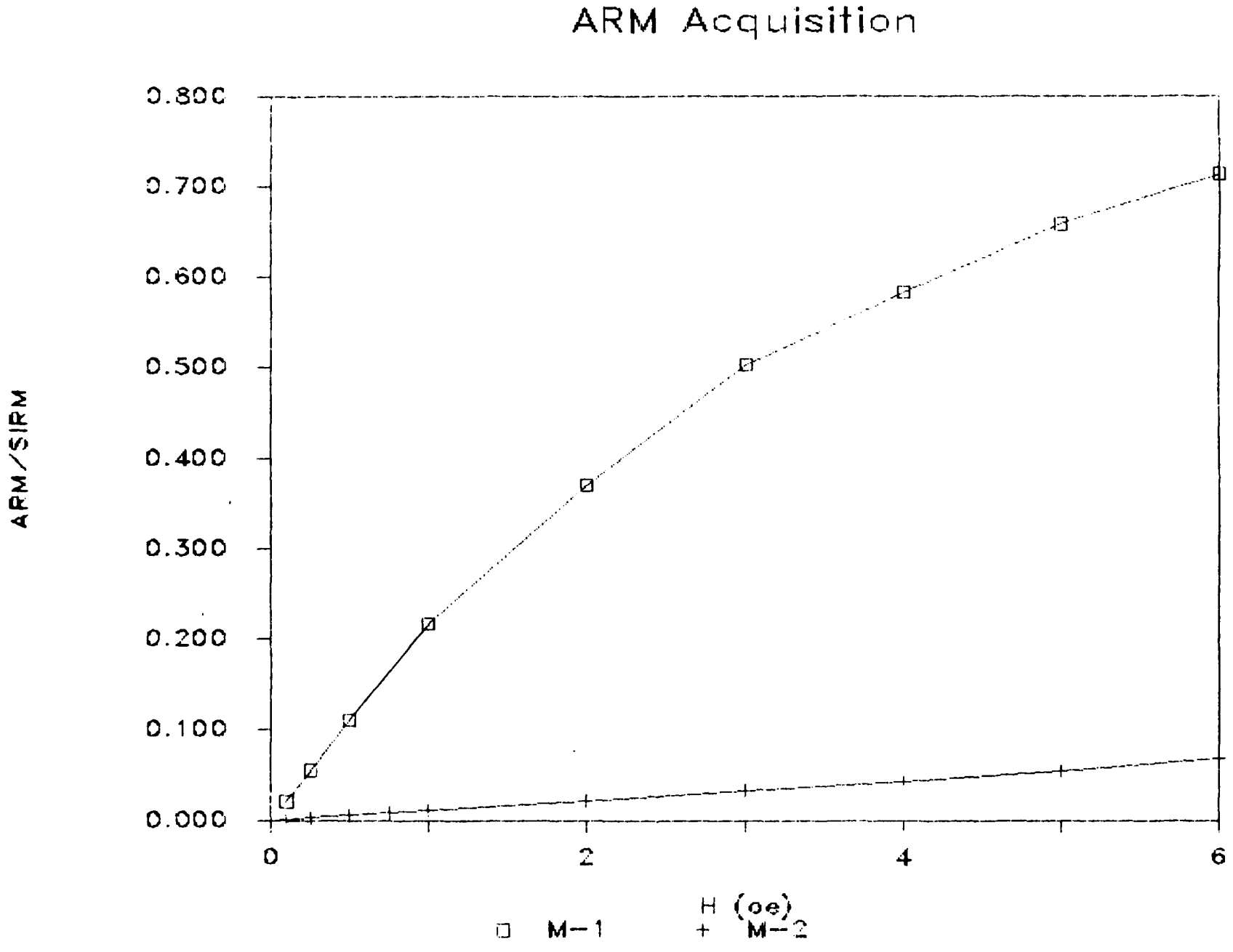
ARM Acquisition
0.800
0.700
0.600
0.500
0.400
0.300
0.200
0.100
0.000
ARM/SIRM
0
2
4
6
H (oe)
M-1
M-2

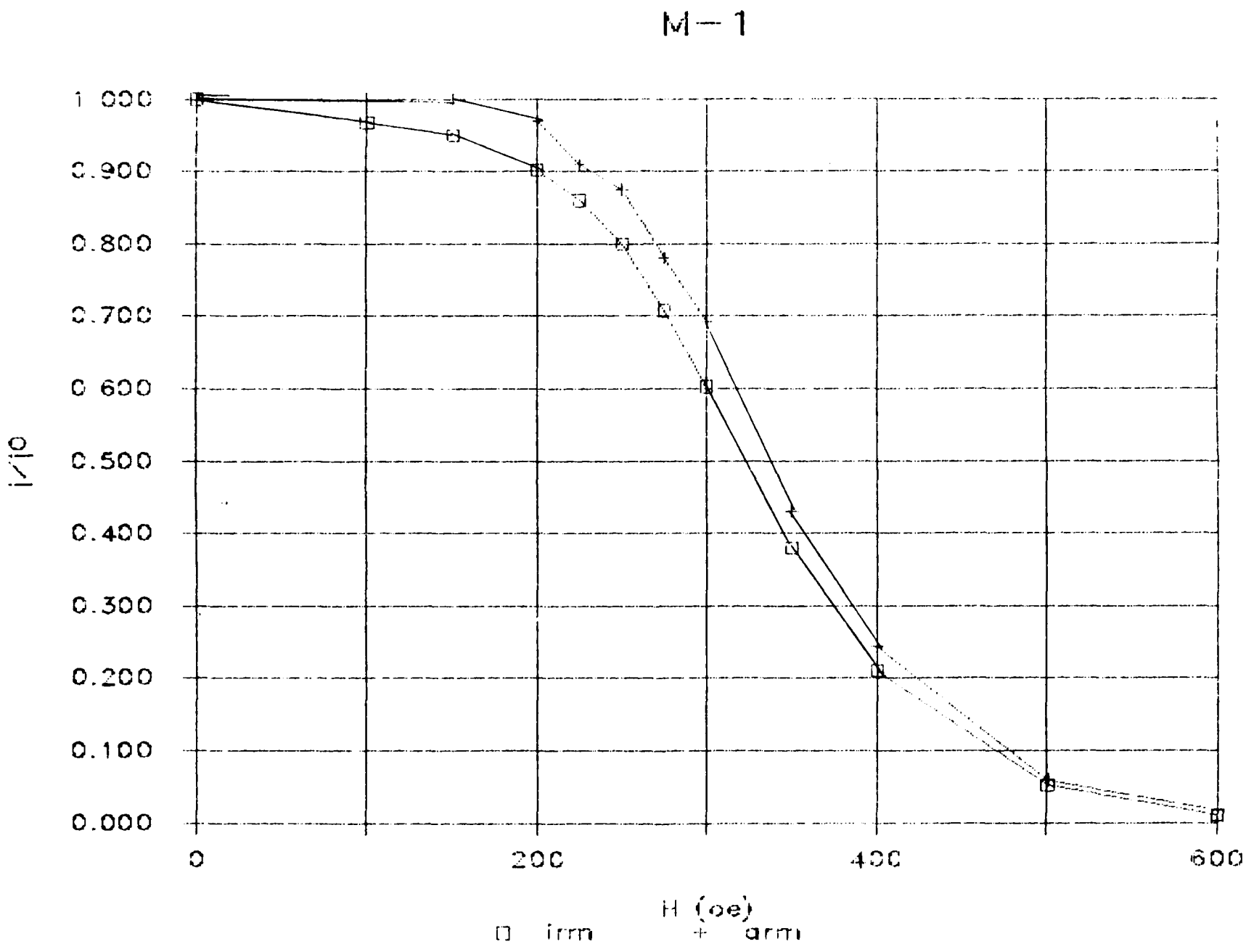
M－1
1.000
0.900
0.800
0.700
0.600
0.500
0.400
0.300
0.200
0.100
0.000
i/i0
0
200
400
600
H (oe)
irm
arm

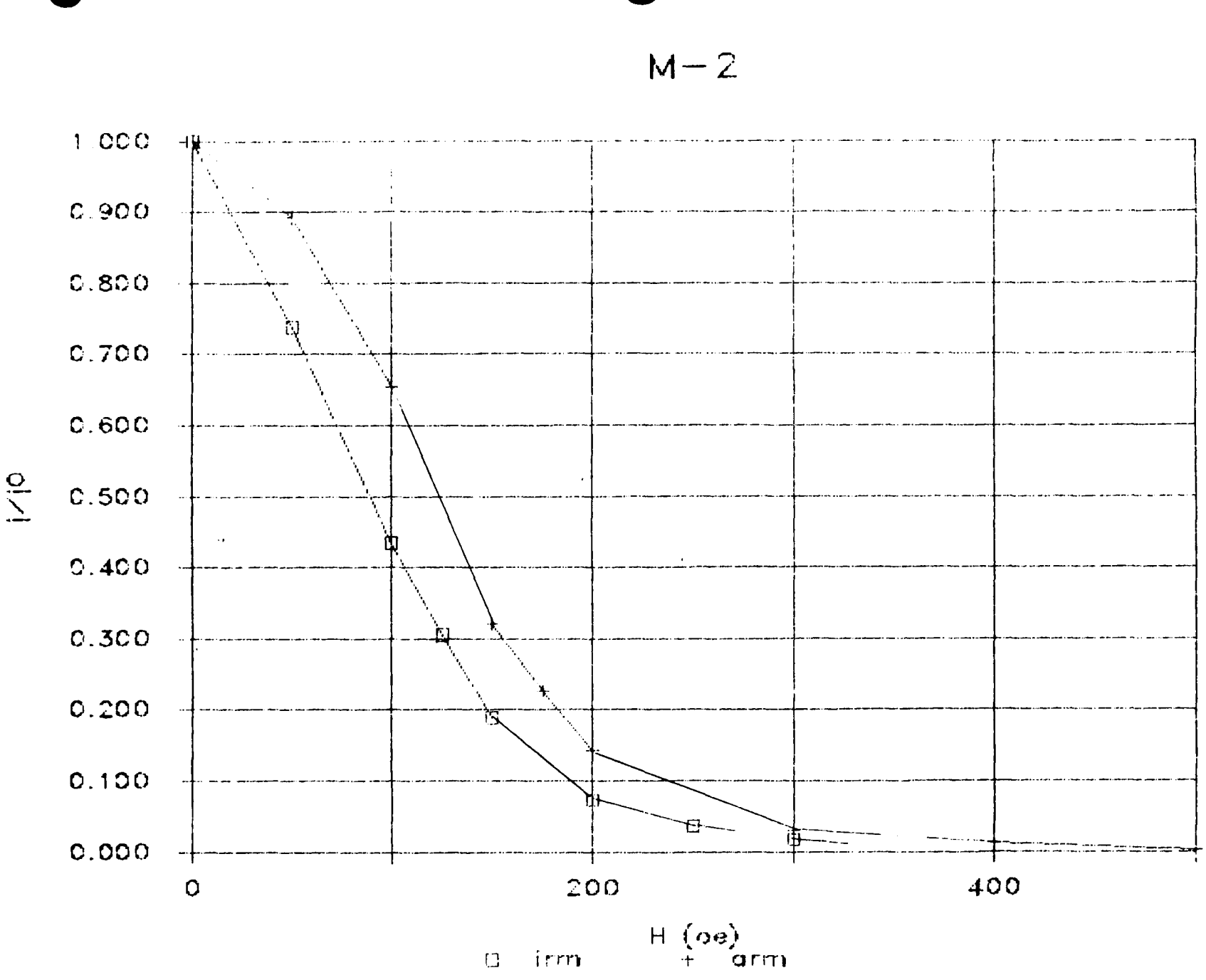
M−2
1.000
0.900
0.800
0.700
0.600
0.500
0.400
0.300
0.200
0.100
0.000
i/i0
0
200
400
H (oe)
irm
arm

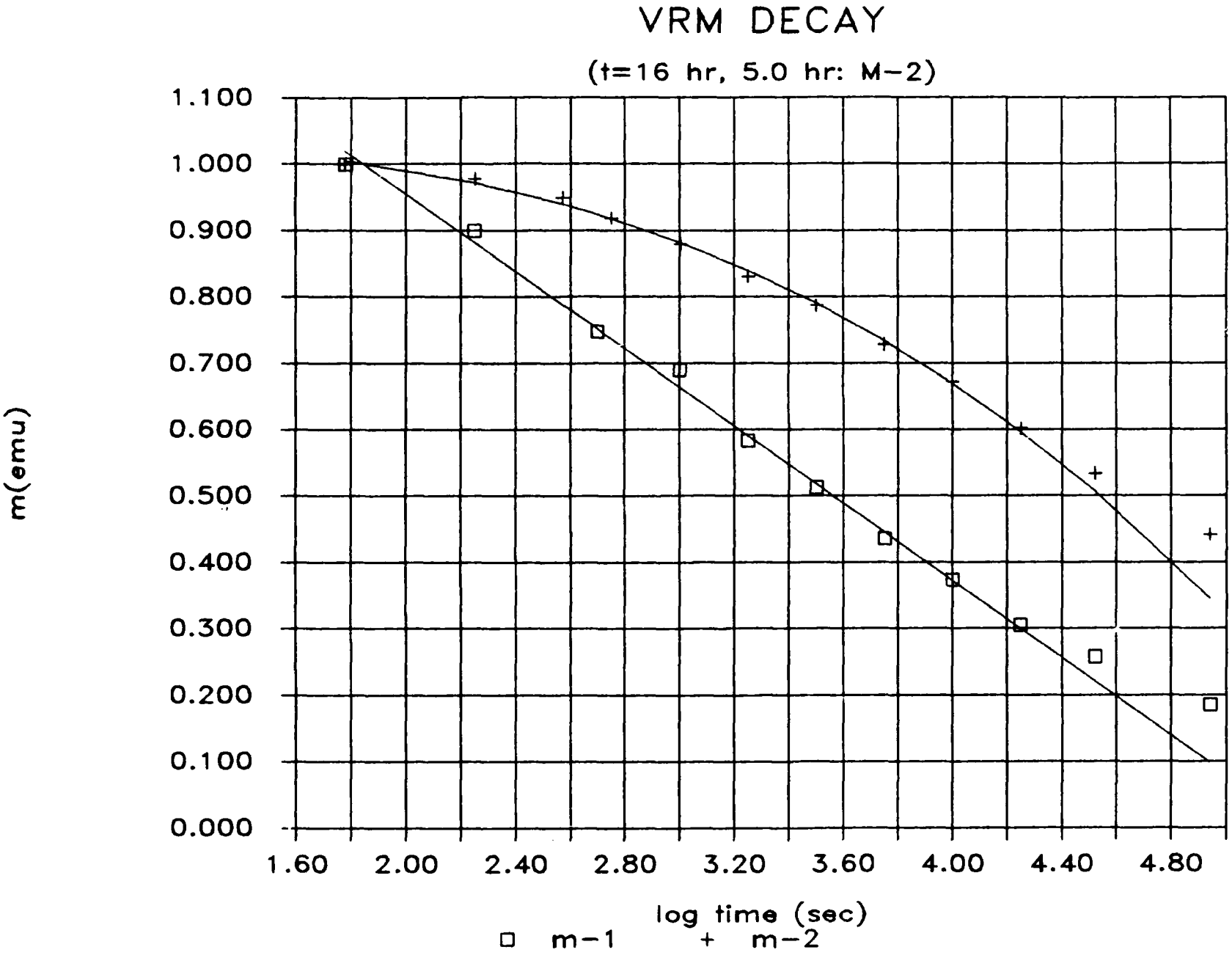
VRM DECAY
(t=16 hr, 5.0 hr: M-2)
1.100
1.000
0.900
0.800
0.700
0.600
0.500
0.400
0.300
0.200
0.100
0.000
m(emu)
1.60
2.00
2.40
2.80
3.20
3.60
4.00
4.40
4.80
log time (sec)
□ m-1
+ m-2

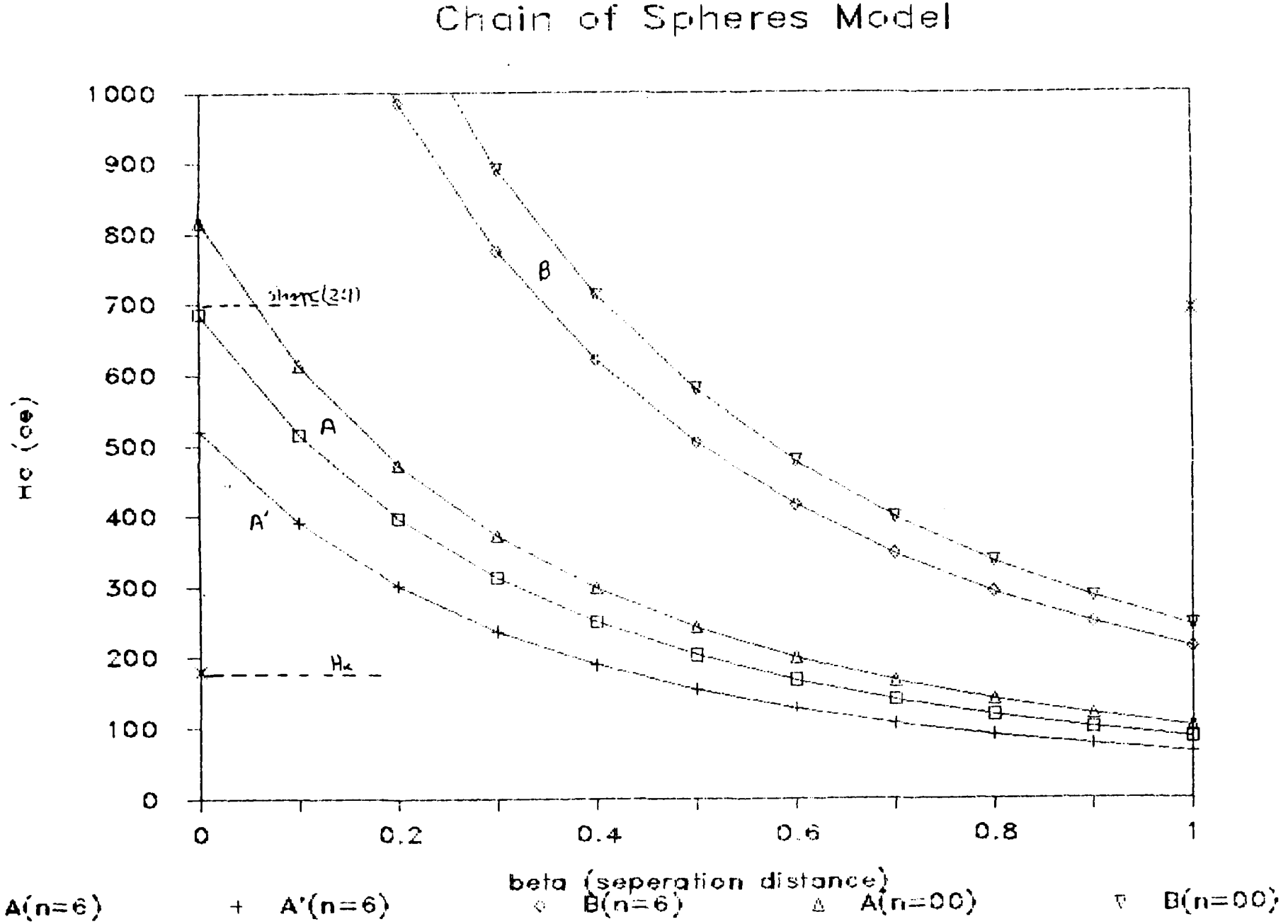
Chain of Spheres Model
1000
900
800
700
600
500
400
300
200
100
0
Hc (oe)
sphere(2:1)
A
B
A'
Hx
0
0.2
0.4
0.6
0.8
1
beta (seperation distance)
A(n=6)
A'(n=6)
B(n=6)
A(n=00)
B(n=00)

III. BASIC EXTRACTION AND MEMBRANE PROPERTIES OF MAGNETIC BACTERIA

A. Introduction

The permanent magnetic character of magnetotactic bacteria (III1) and magnetotactic algae (III2) results from a conspicuous intracellular structure characterizing the group; the "magnetosome" (III3). Those magnetosomes which have been studied are enveloped single crystals of the iron oxide, magnetite, commonly arranged in one or more linear arrays within the cytoplasm (III4, III5, III6, III7). Magnetite crystal morphology may vary among species. In some bacterial species, the crystals are truncated hexagonal prisms as revealed by crystal lattice-imaging. Those within the axenically cultivable species Aquaspirillum magnetotacticum (III8) are truncated octahedrons (III5) which lie in a single helical line along the cell axis and adjacent to the cytoplasmic membrane. The structure and composition of the magnetosome envelope has not yet been widely studied, although trilaminate membrane structures have occasionally been observed surrounding magnetosomes of thin sectioned magnetotactic bacteria collected directly from mud (III9). Balkwill et al. (III3) considered the possibility that magnetite particles of A. magnetotacticum were each surrounded by a lipid bilayer. However, due to the high electron density of the magnetite core, it was not possible to discern the electron opaque inner leaflet expected of a closely apposed lipid bilayer in these stained preparations. We have applied magnetic separation methods to disrupted cells as a unique and effective means of purifying magnetosomes for chemical and structural analyses and, from these magnetosomes, obtained definitive proof of an attendant bilayer envelope.

B. Extraction of Magnetosomes, Methods

1. Media and culture conditions

A. magnetotacticum was grown at 15 L batch cultures as previously described (III10). The chemically defined mineral medium contained 4 mM $NaNO_3$ and lacked organic forms of nitrogen. Iron, at a final concentration of 20 uM, chelated with an equimolar concentration of quinic acid, was added to autoclaved and cooled medium. To study iron limitation, cells were transferred at least three times in medium from which iron compounds were omitted. The total trace iron concentration in media to which no iron was intentionally added was less than 1 uM, as determined with ferrozine (III11).

Cells concentrated by filtration were centrifuged at 5000 x g for 10 min at 4°C. They were resuspended and washed three times in buffer A consisting of 10 mM N-2-hydroxyethylpeperizine-N'-2-ethanesulfonic acid buffer (pH 7.4) containing 10 ug/ml of the protease inhibitor phenylmethyl-sulfonyl fluoride.

2. Magnetosome purification

Approximately 10^{12} cells suspended in 30 ml of buffer A were disrupted by three passes through a French pressure cell at 18,000 psi. Disrupted cells in a centrifuge tube were placed on the gap of a large radar magnet (2 Kgauss). The black magnetic fraction accumulated within thirty minutes at the sides of the tube nearest the magnet. The nonmagnetic fluid fraction was removed by aspiration and the magnetic phase was resuspended in 100 times its volume of buffer A. This procedure was repeated at least ten times. The partially purified magnetosome fraction was suspended in 100 times its volume of buffer A containing 1 M NaCl. The salt was added to

remove adventitious electrostatically associated proteins. Purified magnetosomes were washed at least ten more times with buffer A.

3. Fractionation of nonmagnetic subcellular components

The nonmagnetic cell fraction was separated into outer membrane, inner membrane, and soluble fractions by methods described by Schhnaitman (II12). Nonmagnetic cellular debris (approximately 30 ml obtained from 10^{12} cells) was centrifuged at 500 x g for 15 min at 4°C to remove unbroken cells. The supernatant fluid was centrifuged (200,000 x g; 1 h; 4°C) to remove membranes and the supernatant fluid from this high speed centrifugation, considered to contain soluble proteins, was stored on ice. The brown pellet, containing outer and inner membranes, was suspended in 30 ml of buffer A containing 2% (vol/vol) Triton X-100 and 10 mM $MgCl_2$. The solubilized cytoplasmic proteins were precipitated with cold 95% ethanol overnight at 0°C and collected by centrifugation (500 x g; 15 min; 4°C). Fractionation was evaluated by assaying specific activity of succinic dehydrogenase, an inner membrane enzyme (III4), and by measuring the quantity of 2-keto-3-deooxyoctonate, a constituent of outer member LPS III13.

4. Freeze etching

Cells of A. magnetotacticum strain MS-1 and the nonmagnetic mutant, strain NM-1A, were flash frozen in Freon-22 held at liquid nitrogen temperature. Frozen preparations were fractured, etched for 10 s, and platinum-carbon replicas were made at -100°C in a Balzers BA 360 M freeze etching apparatus. Magnetically purified magnetosomes were similarly prepared. Replicas were examined at 60 kV using either a Philips EM300 or EM400 electron microscope equipped with a gonimeter stage under standard

operating conditions.

5. Thin sections

Cells grown with or without 20 μM iron were fixed for 1 h with glutaraldehyde (5% vol/vol) followed by washing and secondary fixation for 30 min with osmium tetroxide (1% vol/vol) in 509 mM cacodylate buffer (pH 6.8) containing 10 mm $MgCl_2$. Samples were dehydrated in ethanol, followed by propylene oxide, and embedded in EPON 812 or EPON 812-Araldite. Thin sections obtained with an LKB 8800 Ultratome III ultramicrotome were stained with 5% uranyl acetate and 0.4% lead citrate (III14) and viewed with either a Hitachi H600 or Philips EM400 STEM at 80 kV in the TEM mode.

6. Gel electrophoresis

The protein concentration of each subcellular fraction was determined by the method of Lowry et al. (*III15*). *Magnetite, liberated from organic* material during the Lowry assay, was removed by centrifugation prior to spectrophotometric analysis at A_{760}. Proteins (5 ug) from each subcellular fraction were separated by SDS - polycrylamide gel electrophoresis through a 4% stacking gel and a 12% separating gel as described by Laemmli (III16).

Protein from partially purified magnetosomes and nonmagnetic fractions from cells of strain MS-1 were separated by 2-D gel electrophoresis. Samples (30 ug protein each) were separated in a pH gradient ranging from 3.5 to 10.0 with tube gels as described by O'Farrell (III17). At 16 h the constant voltage (400 V) was increased to 800 V for an additional hour. Each tube gel was fixed with 1% agarose to the tope of an SDS - polycrylamide gel (10% to 20% linear gradient of acrylamide). Proteins were separated in the second dimension at constant current (15 mA) for 9 h. Gels were stained with silver as described by Oakley et al. (III18).

7. Lipid analysis

Lipids were extracted from purified magnetosomes with chloroform-methanol as described by Bligh and Dyer (III19) and purified by the Sephadex bead (Pharmacia Fine Chemicals, Piscataway, NJ) method of Wurthier (III19a). The purified total lipids were separated into neutral lipids and fatty acids, glycolipids, and phospholipids with an acid-treated Florisil (Sigma Chemical Co., St. Louis, MO) column (III20). Each lipid fraction was dried and weighed.

The dry phospholipid fraction was dissolved in 0.3 ml of chloroform-methanol (1:1, vol/vol), spotted onto a 20 x 20 cm glass TLC plate of silica gel, and chromatographed in chloroform-methanol-water (65:25:4, vol/vol). Subsequently, the plate was air dried, rotated 90°, and chromatographed in the second dimension using chloroform-methanol-7 N ammonium hydroxide (60:35:5, vol/vol). The developed plate was completely air dried. Lipids were stained with iodine vapors. Each spot was scraped from the TLC plate and transferred to a Pasteur pipet plugged with glass wool. Phospholipids were eluted from the pipets with 2 ml of chloroform-methanol (1:1, vol/vol) followed by 2 ml of absolute methanol. Each sample was collected in a 5 cc glass ampoule and evaporated to dryness under a stream of nitrogen. The residues were each dissolved in 2 ml of 1 N HCl and, after sealing the ampule, heated to 100°C for 4 h. Cooled ampoules were opened and 2 ml of redistilled hexane were added. The mixture was vigorously shaken, allowed to separate, and the aqueous phase was removed and lyophilized. The residues were dissolved in 0.1 ml of distilled water and spotted onto Whatman no. 1 chromatography paper. The chromatogram was developed with redistilled phenol-absolute ethanol-glacial acetic acid (50:5:6, vol/vol),

air dried, and sprayed with ninhydrin reagent. A duplicate chromatogram was sprayed with Dragendorf reagent (III20). The color and R_f value of each unknown sample were compared to those of lipid standards.

C. Results

1. Magnetosome purification

Magnetosomes within A. magnetotacticum cells were always arranged in a linear array in the manner described by Balkwill et al. (III3). They appeared to be enveloped and were separated from one another by a distance of about 150 nm (Fig. III1). The interparticle spacing decreased to about 7 nm in crude preparations of magnetosomes although particles remained attached end-to-end and were still enveloped (Fig. III2a). After NaCl treatment and extensive washing, magnetosomes appeared free of contaminating cellular components. However, each particle remained enveloped and separated from adjacent particles by a distance of 3 nm (Fig. III2b). Purified magnetosomes did not exhibit succinic dehydrogenase activity or contain KDO. SDS detergen treatment removed the enveloping material, destroyed the linear arrangement of the electron-dense particles, allowing them to clump with virtually no interparticle spacing (Fig. III2c).

2. Freeze etching

In frozen and etched preparations of magnetic cells of strains MS-1 (Fig. III3), intact magnetosomes appeared as convex shaped protrusions (MM). Cup-shaped depressions with raised rims (MM) were interpreted to be regions through which the fracture plane had passed with removal of magnetite cores. The raised edges comprising the rim were attributed to a magnetosome envelope differing in composition and structure from adjacent cytoplasm. A

number of representative fracture surfaces associated with magnetosomes within strain MS-1 cells are shown in Fig. III3. The results are those expected if a lipid bilayer were present around each magnetite crystal. Some fractures appeared to expose the external surface of intact magnetosomes (MM). In other cases, the magnetite crystal appeard to have been extracted (as revealed by characteristic raised rims) and the internal surface of the magnetosome enveloping layer (MM) was evident. Occasionally, the fracture appeared to have penetrated the magnetosome envelope without mineral core, thereby exposing a surface which was either the magnetite core or the external face of the internal leaflet of the magnetosome envelope (MMF). The latter would be possible only if the boundary were a lipid bilayer which fractured internally along its hydrophobic region.

Frozen and etched magnetosomes, isolated from cells, displayed these same structural features. When the alignment of magnetosomes to the fracture angle was correct, the particles appeared to be arranged in linear arrays.

Frozen and etched cells of a nonmagnetic mutant strain lacked features associated with magnetite cores or associated enveloping layers although fracture surfaces associated with the inner and outer membranes appeared similar to those of other gram-negative bacteria. Fracture surfaces associated with external wall layers, such as capsules or surface arrays, were not observed with either the magnetic or nonmagnetic strains.

3. Thin sections

Magnetosomes within cells cultured in medium containing 20 mM iron (Fig. III4) appeared in thin sections as an electron-transparent layer and a

2.0 nm electron-dense layer. These results were comparable to those of Balkwill et al. (III3). Stereo views of our thin sections (not shown) offered additional evidence of the bilayer nature of this envelope and suggested it was not merely an electron phase artifact.

Magnetic cells cultured with no added iron contained some typical magnetosomes (Fig. III5). In addition, however, numerous 40 nm diameter membranous vesicles (MV) were present. These vesicles lacked electron-dense cores and were adjacent to one another along the long axis of the cell in the position normally occupied by intact magnetosomes within cells cultured with iron. Each "empty" membrane vesicle consisted of two 1.7 nm thick electron-dense layers separated by a 2.2 nm thick electron-transparent layer. In addition, certain vesicles were not filled with crystalline magnetite but, instead (as determined from energy dispersive X-ray analysis and selected area electron diffraction), contained amorphous iron (Fig. III5) which was presumably a derivative of polyferric hydroxide.

4. Gel electrophoresis

Proteins of the cell outer and inner membranes and of the soluble cell fraction were compared with those associated with the purified magnetosome fraction (Fig. III6). The outer membrane protein profile of this organism was similar to that described by Paoletti et al. (III21). Several proteins of identical molecular weight were shared between the magnetosome membrane and either the outer membrane or inner membrane, but the intensity of the SDS-PAGE bands differed reflecting concentration differences. Two protein molecular weights of 16,000 and 27,000 daltons appeared to be restricted to the magnetosome membrane fraction.

Characteristic magnetosome protein profiles obtained following two-

dimensional gel electrophoresis are shown in Fig. III7. Two abundant anodically migrating proteins, with apparent molecular weights of 15,500 and 16,500 daltons, were present only in the magnetosome fraction. In concert, the uni- and two-dimensional gels showed the magnetosome membrane to be distinct from the other cell outer or inner membranes.

5. Lipid analysis

Magnetically separated and washed magnetosomes from 25 g of wet packed cells yielded 25 mg of purified lipids and 150 mg of purified magnetite. Lipids associated with this magnetosome fraction included free fatty acids (1.5% of total by weight). The phospholipids included phosphatidylethanolamine and phosphatidylserine, as determined by TLC.

D. Magnetosome Membranes

1. Discussion

Previous studies (III3, III9) provided suggestive evidence for a lipid bilayer envelope surrounding the bacterial magnetosome. However, conclusive evidence had been lacking because of the difficulty in interpreting thin sections and the absence of data on purified magnetosomes. We have extended previous cytological studies and have used a magnetic separation method to recover intact magnetosomes from cellular debris. Our data, obtained by freeze-etching and by thin sectioning both cells and magnetically extracted magnetosomes, indicate the presence of a trilaminate membrane surrounding each magnetite core. This membranous envelope was absent from purified magnetosomes treated with detergent to remove lipids and proteins. Trilaminate membrane vesicles with dimensional and spataial characteristics of magnetosomes, but devoid of magnetite cores, were present in wild type

magnetic cells grown without iron. Amorphous iron was occasionally present in small quantity within these vesicles. Magnetosomes, vesicles with amorphous iron, or empty vesicles were not present within cells of the nonmagnetic mutant strain NM-1A. It was apparent, therefore, that these membranes were an integral part of magnetosomes and we consider them to be magnetosome boundary membranes.

Magnetosome membranes do not appear to be contiguous with the cytoplasmic membrane. We have never observed connections between the two membranes in numerous thin sections, including stereo views, of magnetic cells. If the magnetosome membranes were invaginations of the cytoplasmic membrane, we would expect freeze-etching to reveal severed connections as pits in the inner surface of this membrane [as observed with freeze-etched preparations of cyanobacteria which posses photosynthetic membranes as vesicular intrusions of the cytoplasmic membrane (III22)]; it did not. Furthermore, when spheroplasts were made, they did not evert their magnetite crystals as would be expected of particles within surficial invaginations of the cytoplasmic membrane.

The magnetosome membrane does not appear significantly different in overall composition from other cell membranes. We detected proteins, free fatty acids, glycoproteins, and phospholipids as components. The ratio of their abundance is that expected for a biological membrane (III23). Although most proteins detected in envelopes of purified magnetosomes were of similar mass (but not quantity) to those of the cytoplasmic membrane, two were uniquely with the magnetosome envelope. It is tempting to speculate that these could have a specific role in magnetite production. As enzymes, they could promomte the accumulation of supersaturating quantities of iron

within vesicles, serve to oxidize iron, or reduce and dehydrate the ferrihydrate precursor (III24) of bacterial magnetite. They could also be ferrihydrite-associated proteins such as bacterioferritin (III25) apoprotein. As structural proteins, they might contribute to the compartmentalization deemed essential for "organic matrix-mediated" (III26) biomineralization. The use of artificial membranous vesicles to study iron biomineralization, as recently initiated by Mann et al. (III27), would undoubtedly be advanced by purification and inclusion of these magnetosome-specific proteins.

E. References

III1. R. P. Blakemore, "Magnetotactic bacteria," Ann. Rev. Microbiol. 36 (1982) 217-238.

III2. F. F. Torres De Araujo, M. A. Pires, R. B. Frankel, and C. E. Bicudo, "Magnetite and magnetotaxis in algae," Biophys. J. 50 (1986) 375-378.

III3. D. L. Balkwill, D. Maratea, and R. P. Blakemore, "Ultrastructure of a magnetic spirillum," J. Bacteriol. 141 (1980) 1399-1408.

III4. W. J. Dobrogosz, "Enzymatic activity," (1981) 365-392. In P. Gerhardt, R. G. E. Murray, R. N. Costilow, E. W. Nester, W. A. Wood, N. R Krieg, and G. B. Phillips (ed.), Manual of methods for general bacteriology. Americal Society for Microbiology, Washington, DC.

III5. S. Mann, R. B. Frankel, and R. P. Blakemore, "Structure, morphology and crystal growth of bacterial magnetite," Nature 310 (1984) 405-407.

III6. T. Matsuda, J. Endo, N. Osakabe, and A. Tonomura, "Morphology and structure of biogenic magnetite particles," Nature 302 (1983) 411-412.

III7. K. M. Towe, and T. T. Moench, "Electron-optical characterization of bacterial magnetite," Earth and Planet. Sci. Lett. 52 (1981) 213-220.

III8. D. Maratea, and R. P. Blakemore, Aquaspirillum magnetotacticum sp. nov., a magnetic spirillum. Int. J. Syst. Bacterio. 31 (1981) 452-455.

III9. R. P. Blakemore, "Magnetotactic bacteria," Science 190 (1975) 377-379.

III10. R. P. Blakemore, D. Maratea, and R. S. Wolfe, "Isolated and pure culture of a freshwater magnetic spirillum in chemically defined medium," J. Bacteriol. 140 (1979) 720-729.

III11. L. L. Stookey, "Ferrozine -- a new spectrophotometric reagent for iron," Anal. Chem. 42 (1970) 779-781.

III12. C. Schnaitman, "Cell fractionation," (1981) 52-61. In P. Gerhardt, R. G. E. Murray, R. N. Costilow, E. W. Nester, W. A. Wood, N. R. Kreig, and G. B. Phillips (ed.), Manual of methods for general bacteriology. American Society of Microbiology, Washington, DC.

III13. M. J. Osborn and H. C. P. Wu, "Proteins of the outer membrane of the gram-negative bacteria," Ann. Rev. Microbiol. 34 (1980) 3698-3822.

III14. E. S. Reynolds, "The use of lead citrate at high pH as an electron-opaque stain in electron microscopy," J. Cell. Biol. 17, (1963) 208-212.

III15. O. H. Lowry, N. J. Rosenbrough, A. L. Farr, and R. J. Randall, "Protein measurement with the folin reagent," J. Biol. Chem. 193 (1951) 265-275.

III16. U. K. Leammli, "Cleavage of stuctural proteins during the assembly of the head of bacteriphage T4," Nature 227 (1970) 680-685.

III17. P. H. O'Farrell, "High resolution two dimensional electrophoresis of proteins," J. Biol. Chem. 250 4007-4021.

III18. B. R. Oakley, D. R. Kisch, and N. R. Morris, "A simplified stain for detecting proteins in polycrylamide gels," Anal. Biochem. 105 361-363.

III19. R. E. Wurthier, "Purification of lipids from nonlipid contaminants on Sephadex Bead Columns," J. Lipid Res. 7 (1966) 558-561.

III20. R. S. Hanson, and J. A. Phillips, "Chemical composition," (1981) 328-364. In P. Gerhardt, R. G. E. Murray, R. N. Costilow, E. W. Nester, W. A. Wood, N. R. Krieg, and G. B. Phillips (ed.), Manual of methods for general bacteriology. American Society for Microbiology, Washington, DC.

III21. L. C. Paoletti, and R. P. Blakemore, "Hydroxamate production by Aquaspirillum magnetotacticum," J. Bacteriol. 167 (1986) 73-76.

III22. M. A. Lommen and S. Takemoto, "Comparison, by freeze-fracture electron microscopy, of chromotophores, spheroplast-derived membrane vesicles, and whole cells of Rhodopseudomonas spheriodes, J. Bacteriol. 136 (1978) 730-741.

III23. H. J. Rogers, "The membranes of bacteria," (1983) 28-53. In. J. A. Cole, C. J. Knowles, and D. Schlessinger (ed.), Bacterial cell structure. American Society of Microbiology, Washington, DC.

III24. R. B. Frankel, G. C. Papaefthymiou, R. P. Blakemore, and W. O'Brien "Fe_3O_4 precipitation in magnetotactic bacteria," Biochim. Biophys. Acta. 763 (1983) 147-159.

III25. E. I. Stiefel and G. D. Watt, "Azotobacter cytochrome b_{557}.5 is a bacterioferritin," Nature 279 (1979) 81-83.

III26. R. B. Frankel, R. P. Blakemore, and R. S. Wolfe, "Magnetite in freshwater bacteria," Science 203 (1979) 1355-1356.

III27. S. Mann, J. P. Hannington, and R. J. P. Williams, "Phospholipid vesicles as a model system for biomineralization," Nature 324 (1986) 565-567.

F. Figure Captions

Figure III1: Thin section of a magnetic cell of strain MS-1. Outer membrane, OM; inner membrane, IM; magnetosome membrane, MM; magnetite, M. Bar equals 100 nm.

Figure III2: Electron microscopical evaluation of magnetosome purity. (A) Magnetosomes liberated from cells following three passages through a French pressure cell. Particles, each separated by a distance of 4 nm, remain in chains. Note contaminating cellular debris. (B) Purified magnetosomes following treatment with M NaCl and extensive washing. Interparticle spacing has decreased to 3.5 nm, yet magnetosomes remain in chains. Note the covering around each particle and the lack of contaminating cellular debris. (C) Magnetosomes following treatment with 10% SDS. Enveloping materials has been removed and particles are randomly oriented. Bar equals 250 nm.

Figure III3: (A) Freeze-etch preparation of a magnetic cell of strain MS-1. An intact magnetosome appears convex with the magnetosome membrane surface (MM) exposed while a magnetosome from which the iron core has been removed by the fracture appears concave revealing the inside of the membrane (MM). PHB, poly-B-hydroxybutyrate. (B) The fracture has penetrated the magnetosome membrane and has exposed what appears as either the face of the magnetite particles or the convex fracture of the inner leaflet of the magnetosome membrane, MM. Arrow indicates the direction of shadow. Bar equals 250 nm.

Figure III4: Thin sections of cells cultured under iron limitation. (A) Note the trilaminate structure of the membranous vesicles (MV) which lie along the same axis as complete magnetosomes. Bar equals 250 nm.

Figure III5: Note small electron-dense deposits of amorphous iron within the membranous vesicles. Bar equals 100 nm.

Figure III6: SDS-PAGE of cell fractions of strain MS-1. Outer membrane proteins, OM; inner membrane proteins, IM; magentosomes membrane proteins, MM; soluble proteins, SP; molecular weight standards, MW. Arrows indicate positions of the 16,000 and 27,000 dalton magnetosome membrane proteins.

Figure III7: Two-dimensional gel electrophoresis of proteins recovered from the (A) magnetic and (B) nonmagnetic fractions from strain MS-1. Arrows indicate the position of the 15,500 and 16,500 dalton anionic proteins which are present only in the magnetic fraction.

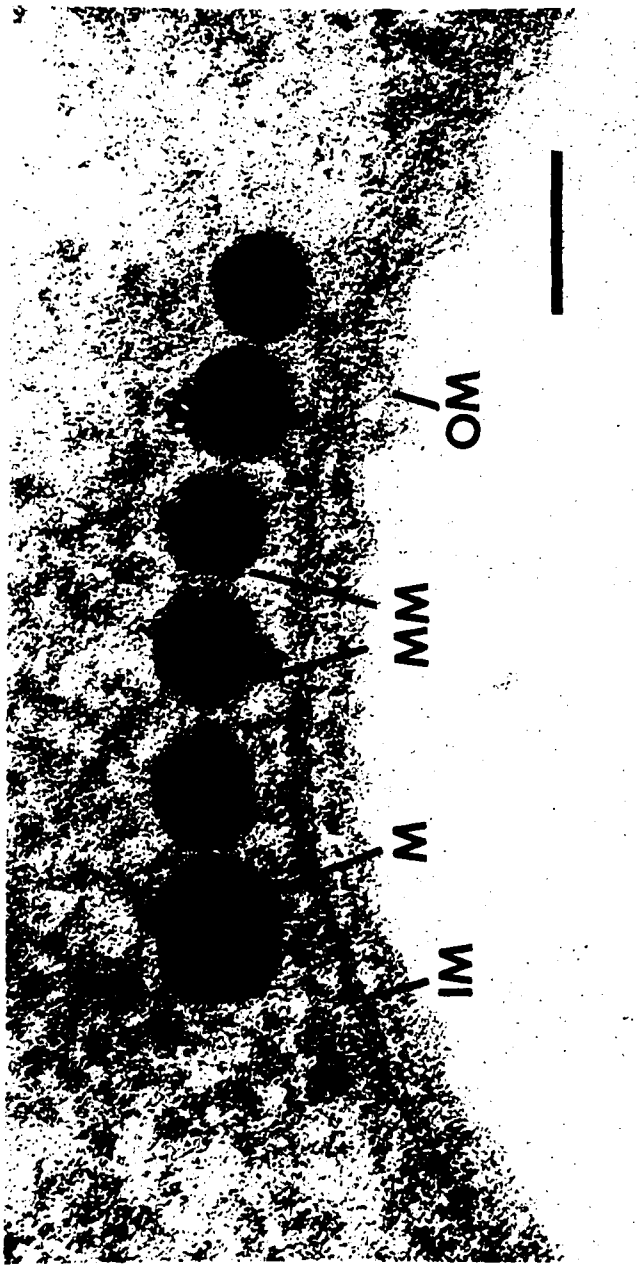
OM
MM
M
IM


B
C
A

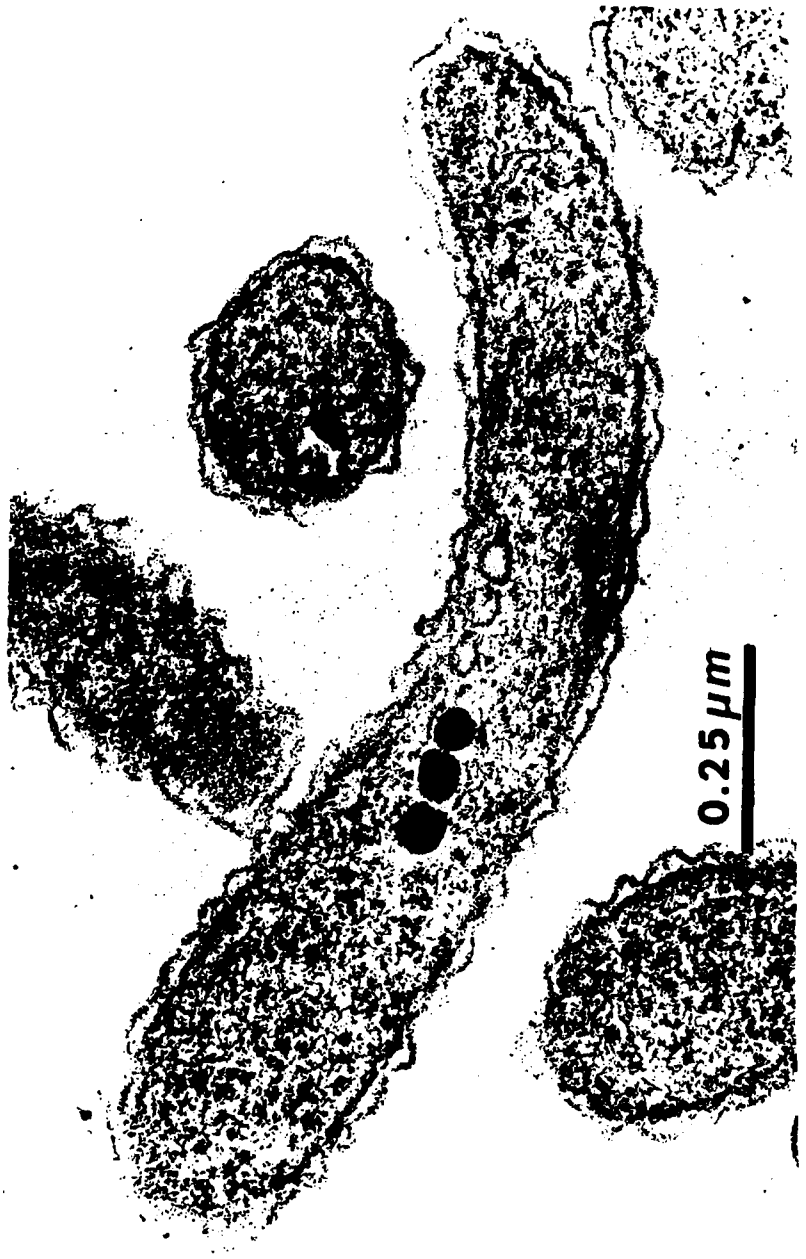
0.25 μm

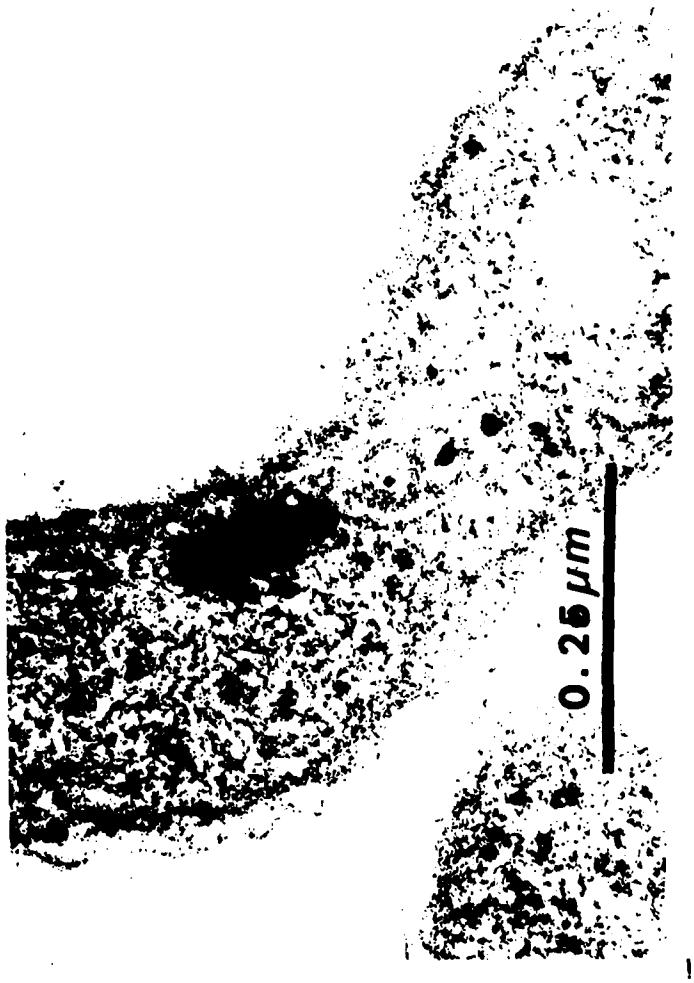
0.25 μm

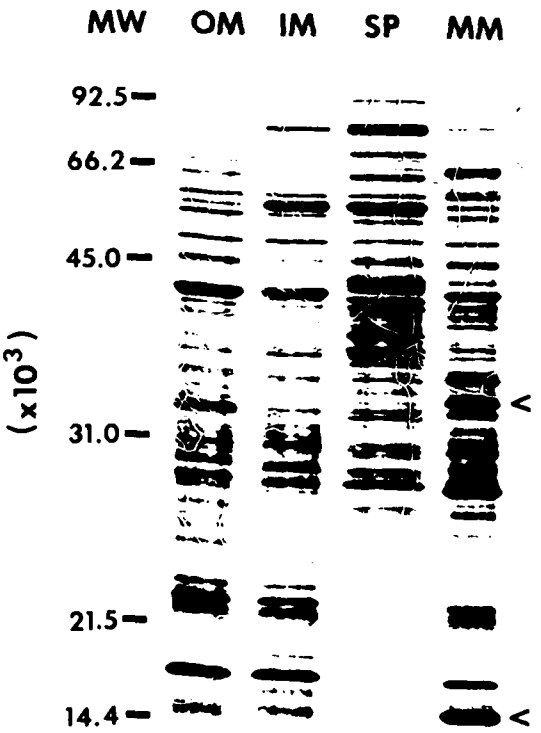
MW
OM
IM
SP
MM
92.5
66.2
45.0
31.0
21.5
14.4
(x10³)

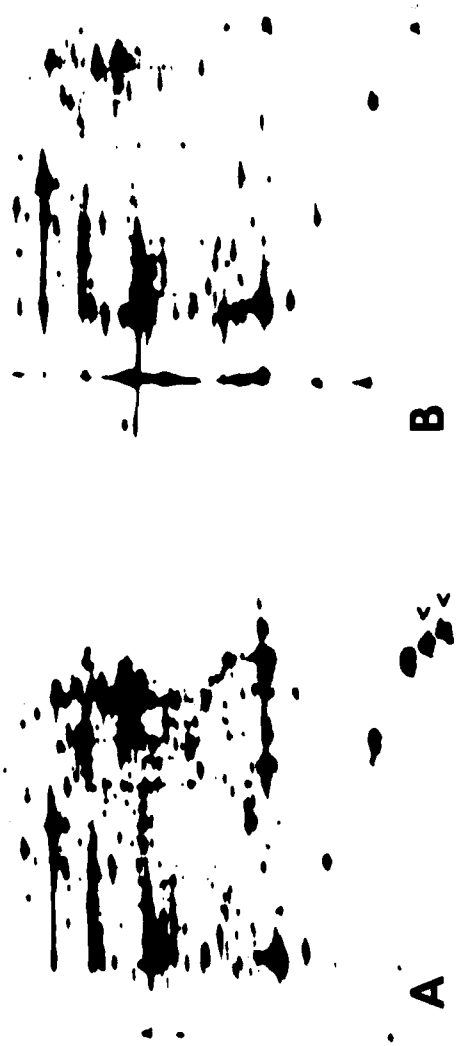
B
A

IV ELECTROMAGNETIC PROPERTIES OF MAGNETIC BACTERIA

A. Introduction

Measurements of the absorption coefficient, refractive index and dielectric permitivity of magnetotactic bacteria have been carried out in the frequency range 60-750 GHz (wavenumber range 2-25 cm^{-1}). The measurements were made using the technique of dispersive fourier transform spectroscopy (IV1-IV3). The experimental set up, a two-beam polarization interferometer, is shown schematically in Fig. IV1. The source is a high-pressure mercury lamp and the detector is an InSb bolometer operated at liquid helium temperatures. The polarizers are wire-wound grids.

B. Sample Preparation

The samples consisted of freeze-dried cells following glutaraldehyde fixation in a low-melting point, inert binder. About 1 gram of freeze-dried cells were thoroughly dispersed in a mixture consisting of lanolin, vaseline and parrefin, each one part by weight. This mixture melts at about 50°C, and should have not strong EM absorption features in the frequency range of interest because there are no strongly polarizable chemical groups associated with these materials. The sample holders consisted of three inch diameter dense polyethylene, another inert substance. Three dishes were prepared. One dish was measured empty, another filled with the binder, and the third with binder and bacteria.

C. Absorption Coefficient

The first measurements were made for about 1 gram of bacterial cells added to the binder. The absorption coefficient as a function of frequency (wave number) is shown in Fig. IV2 and IV3. By subtracting the results of

the three dishes, the absorption of the binder and bacteria, the binder, and the bacteria could be determined. As can be seen, the absorptions are relatively featureless over the frequency range of interest. Refractive index and permittivity are shown for the bacteria in Fig. IV4.

In these measurements, the sample is placed in one of the active arms of the interferometers. It was noticed that rotating the specimen in place resulted in changes in the absorption intensity and phase. This implies that the sample was slightly birefringent. This could result from some partial alignment of the bacteria in the sample which could occur as the sample cooled from the melting point of the binder (50°C) to ambient temperature in the local geomagnetic or laboratory background field.

A more concentrated sample was prepared by adding approximately 4 grams of freeze-dried cells to the bacteria plus binder sample. This time we decided to enhance the birefringent effect by cooling the specimen from 50°C in the 5000 G horizontal field of an electromagnet. The absorption coefficient as a function of frequency (wave number) is shown in Fig. IV5, for two orientations of the sample dish, 90° apart. A signficant birefringent effect can be seen in these data.

Finally, a measurement of the bacteria and binder sample was made in an intense magnetic field of 79 kOe oriented perpendicular to the dish, i.e., oriented at 90° to the orientation axis of the bacteria in the sample. The measurement is shown in Fig. IV6. There is a strong absorption line at about 188 GHz. It is reasonable to attribute this absorption to ferrimagnetic resonance on the Fe_3O_4 in the bacterial magnetosomes. The resonance frequency as a function of g factor and magnetic field is given by

$$\nu = 1.4 \times g\, H \quad \text{GHz} \qquad \text{IV.1}$$

where H is in kilogauss. For g = 2, we expect the resonance to occur at 221 GHz. Therefore the experimental g-factor is 1.70. Further analysis is required to understand the details of the resonance. However, we note that the magnetic data showed that the anisotropy fields were of the order of 400 G or so. Therefore in a 79 KOe field, the magnetosome particle moments should be magnetized parallel to the external magnetic field.

D. References

IV1. M. N. Afsar, "Dielectric Measurements of Millimeter-Wave Materials," IEEE Transactions on Microwave Theory and Techniques MTT-32 (1984) 1598-1609.

IV2. M. N. Afsar, "Precision Dielectric Measurements of Non-polar Polymers in the Millimeter Wavelength Range," IEEE Transactions on Microwave Theory and Techniques MTT-33, p. 1410-1415.

IV3. M. N. Afsar, "The Measurement of the Properties of Materials," Proc. of the IEEE 74 (1986) 183-199.

E. Figure Captions

Fig. IV1: The layout of a two-beam polarization interferometer for dispersive Fourier transform spectroscopy of solids. The radiation source is a high-pressure mercury vapor lamp. The polarizer/analyzer grid polarizes the incident beam and analyzes beams before reaching the detector. The beam-splitter grid splits the polarized beam and recombines them.

Fig. IV2: Absorption coefficient as a function of frequency for binder, binder and bacteria, and bacteria alone.

Fig. IV3: Absorption coefficient for bacteria alone from Fig. IV1 on an expanded scale.

Fig. IV4: Refractive index and permittivity for bacteria as a function of frequency.

Fig. IV5: Absorption coefficient as a function of frequency for the binder alone and for two orientations of the binder and bacteria sample. The absorption due to the bacteria alone are also shown.

Fig. IV6: Absorption as a function of frequency for the bacteria in a vertical magnetic field of 79 kOe.

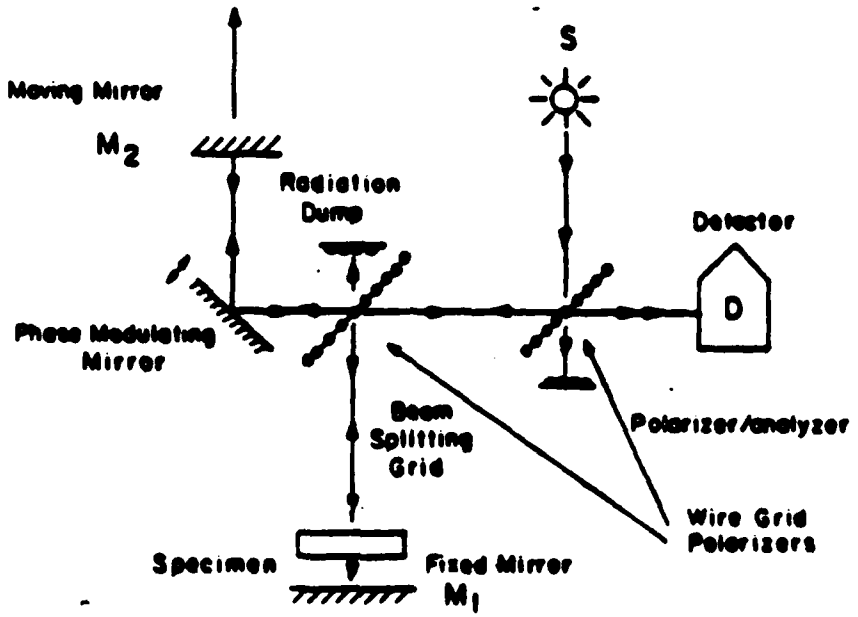

Fig. 1. The layout of a two-beam polarization interferometer for dispersive Fourier transform spectroscopy of solids. The radiation source is a high-pressure mercury vapor lamp. The polarizer/analyzer grid polarizes the incident beam and analyzes beams before reaching the detector. The beam-splitter grid splits the polarized beam and recombines them.

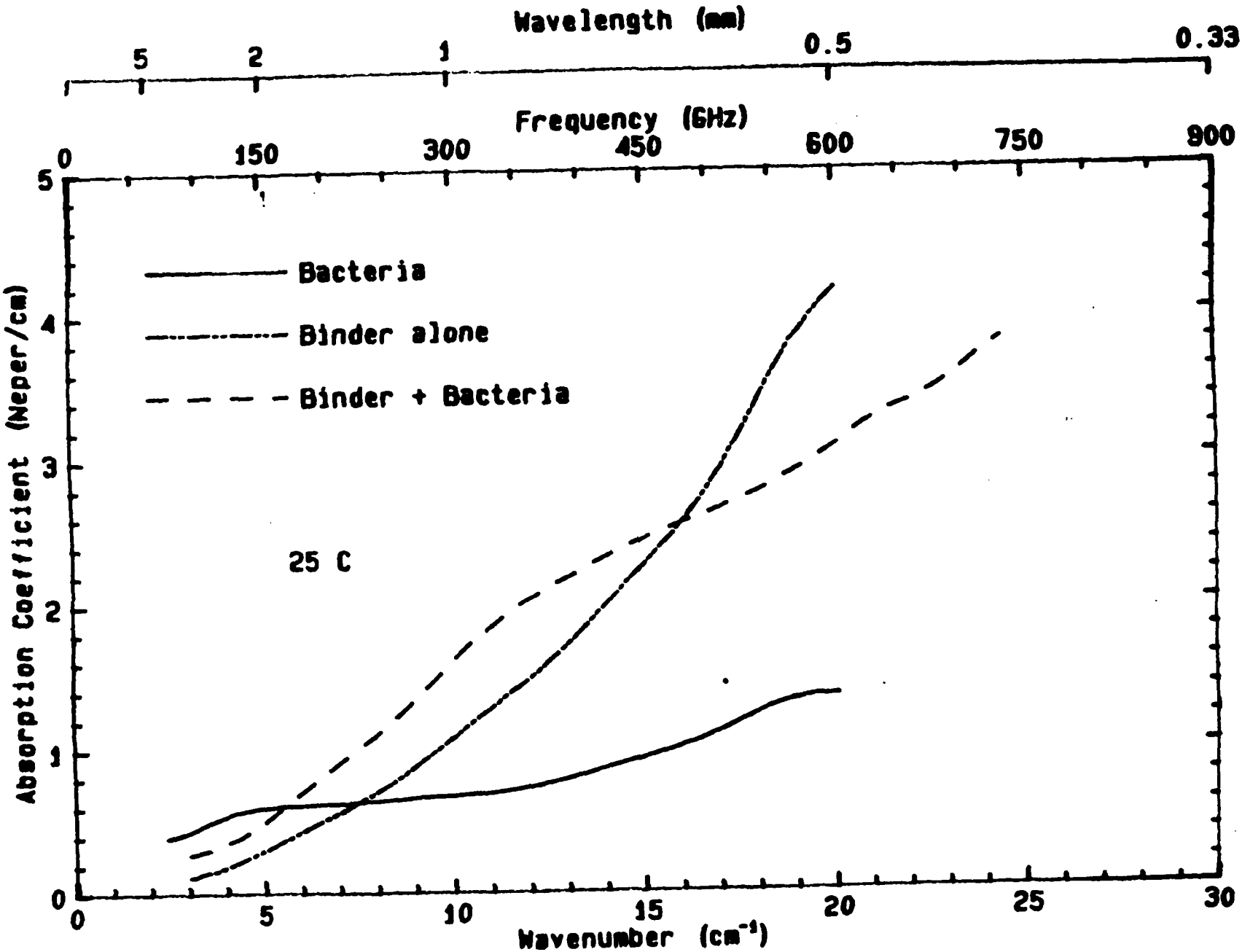
Wavelength (mm)
5
2
1
0.5
0.33
Frequency (GHz)
0
150
300
450
600
750
900
Bacteria
Binder alone
Binder + Bacteria
25 C
Absorption Coefficient (Neper/cm)
0
1
2
3
4
5
0
5
10
15
20
25
30
Wavenumber (cm⁻¹)

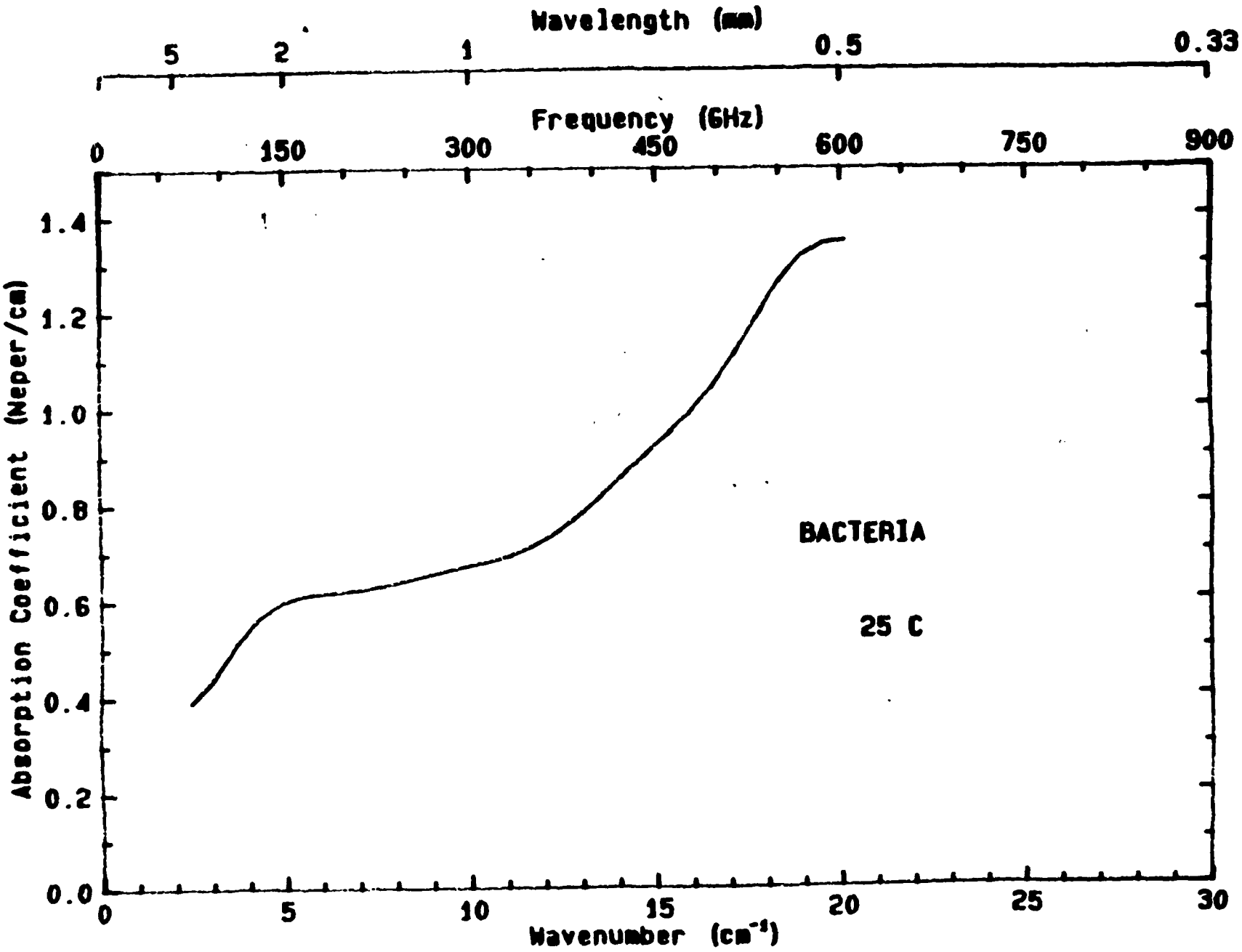
Wavelength (mm)
5
2
1
0.5
0.33
Frequency (GHz)
0
150
300
450
600
750
900
Absorption Coefficient (Neper/cm)
1.4
1.2
1.0
0.8
0.6
0.4
0.2
0.0
BACTERIA
25 C
0
5
10
15
20
25
30
Wavenumber (cm⁻¹)

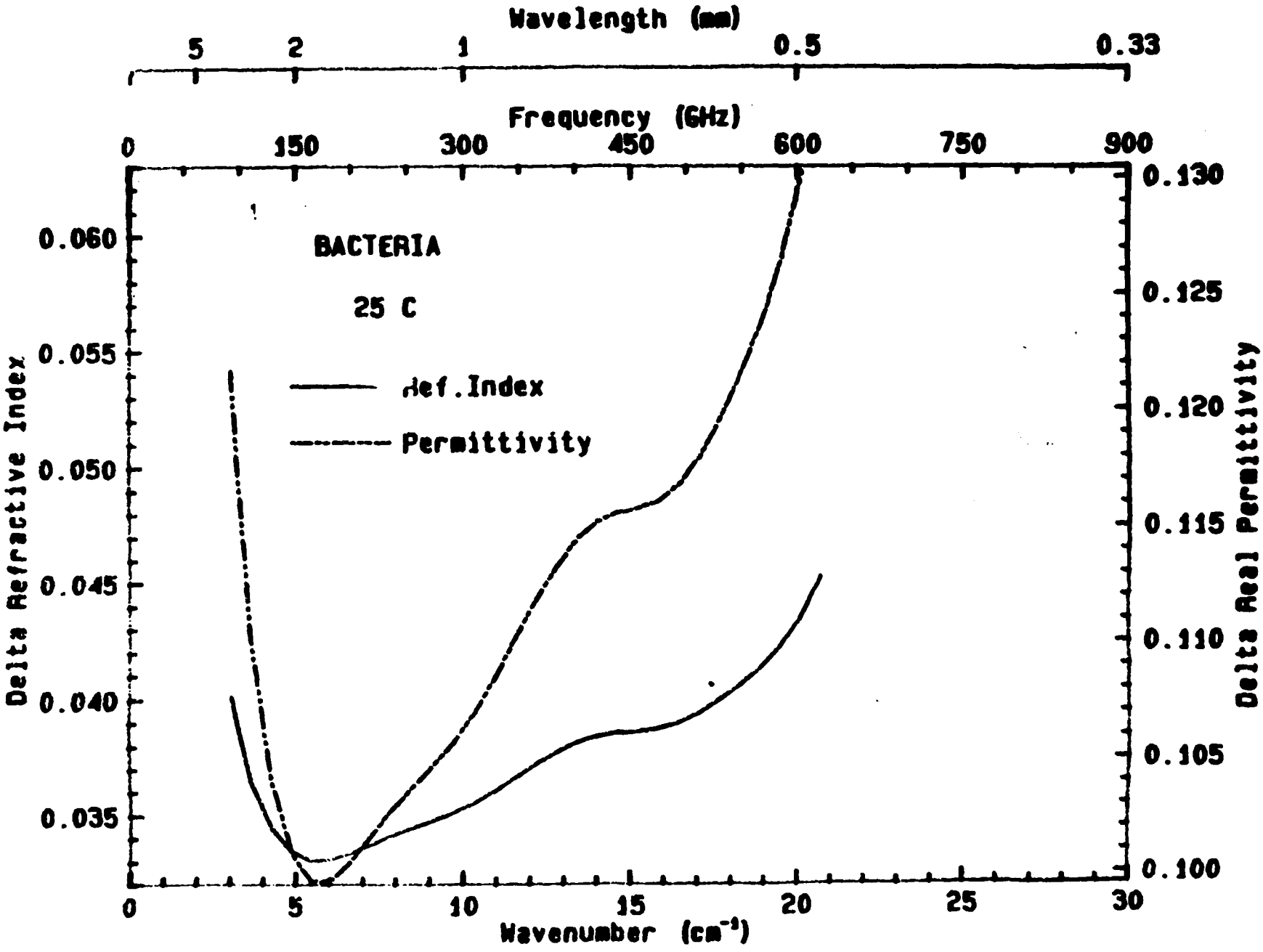
Wavelength (mm)
5
2
1
0.5
0.33
Frequency (GHz)
0
150
300
450
600
750
900
BACTERIA
25 C
Ref.Index
Permittivity
Delta Refractive Index
0.060
0.055
0.050
0.045
0.040
0.035
Delta Real Permittivity
0.130
0.125
0.120
0.115
0.110
0.105
0.100
0
5
10
15
20
25
30
Wavenumber (cm⁻¹)

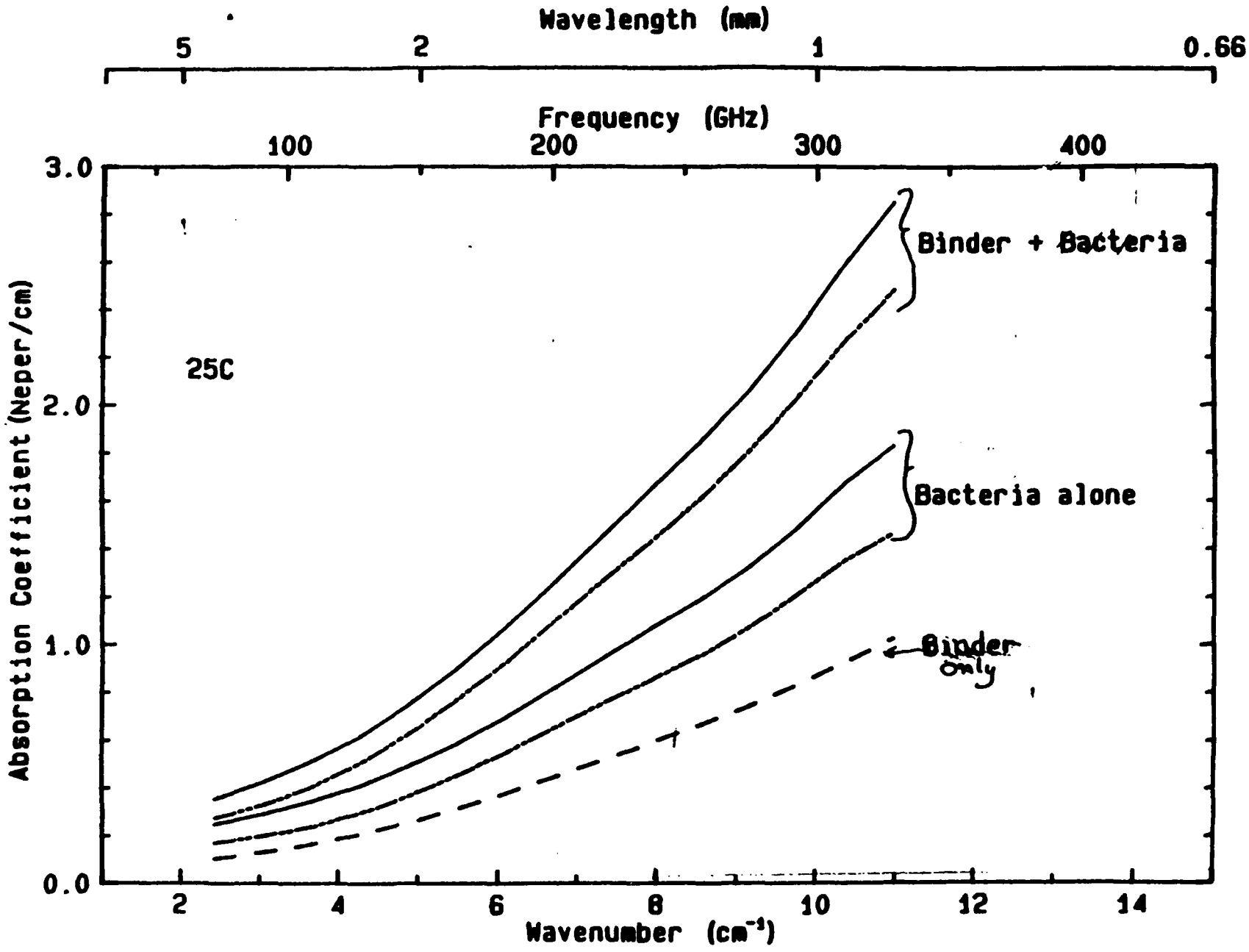
Wavelength (mm)
5
2
1
0.66
Frequency (GHz)
100
200
300
400
3.0
2.0
1.0
0.0
Absorption Coefficient (Neper/cm)
25C
Binder + Bacteria
Bacteria alone
Binder Only
2
4
6
8
10
12
14
Wavenumber (cm⁻¹)

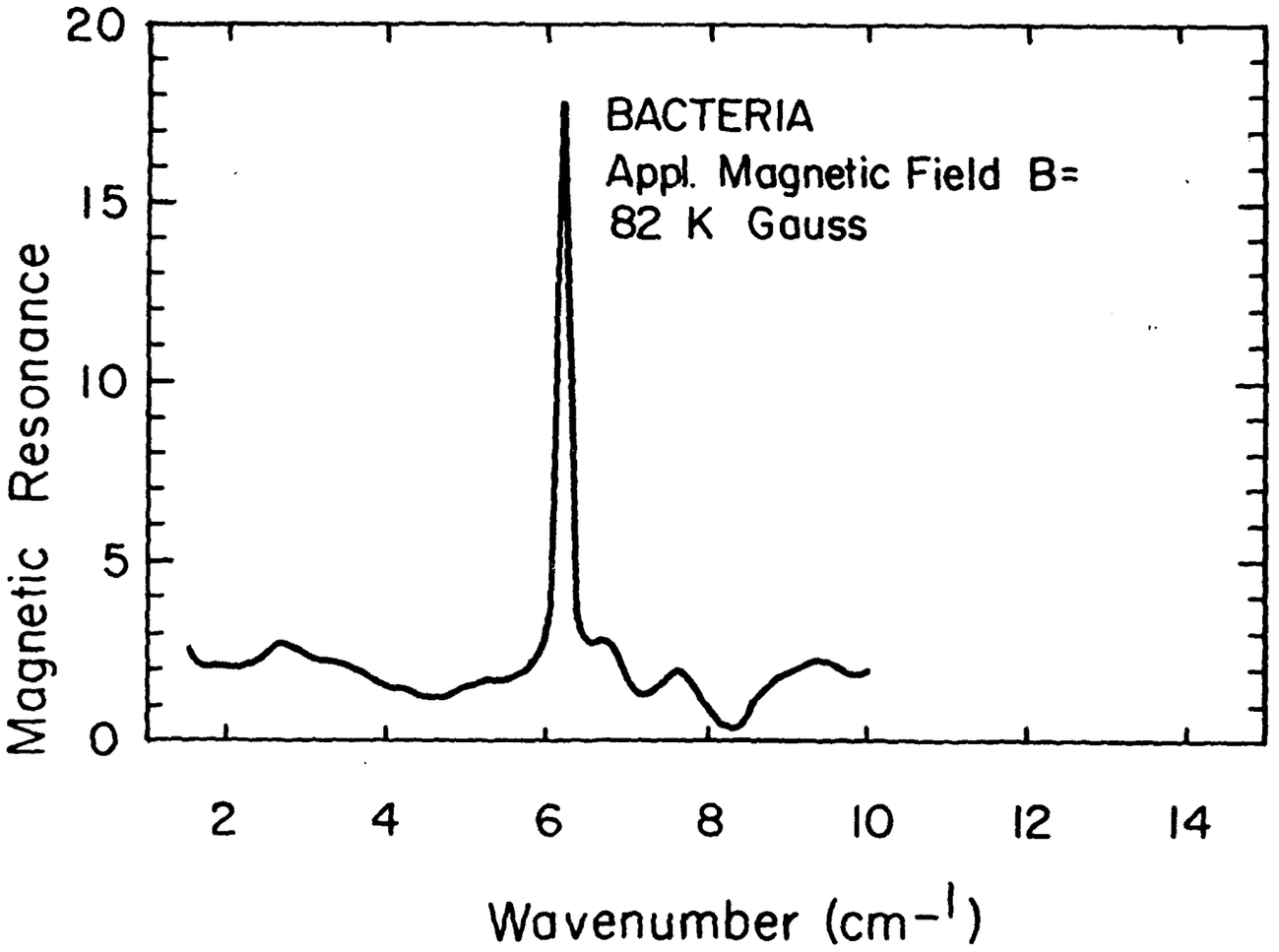
BACTERIA
Appl. Magnetic Field B=
82 K Gauss
Magnetic Resonance
0
5
10
15
20
2
4
6
8
10
12
14
Wavenumber (cm⁻¹)

SUPPLEMENT 1 — GENETIC ENGINEERING

A. Introduction

Production of useful commodities chemicals or biomolecules by means of genetically improved microorganisms growing in large-scale culture describes the very essence of genetic engineering biotechnology. We have undertaken research directed at making strains of magnetic bacteria useful in biotechnology. Two goals are to place genes coding for useful products into existing strains of magnetic bacteria and, conversely, to locate and move genes coding for magnetosomes from magnetic bacteria to microorganisms which produce useful products. In either case, the advantages which would accrue include much improved methods, employing high gradient magnetic separation techniques, for separating cells from their excreted products.

B. Approach and Results

It was considered possible that genes coding for magnetite synthesis might reside on a plasmid. Plasmids and other extrachromosomal elements were sought using ethidium bromide stained agarose gel electrophoresis. In addition, Ekhardt gels (in-well lysis methods) were used. No plasmids or extrachromal DNA elements have been found, hoever, necessitating a more exacting search for magnetic genes. A DNA library or gene bank was prepared of the total DNA of A. magnetotacticum strain MS-1, using a plasmid vector in preparation for moving strain MS-1 DNA fragments into E. coli strain K-12. Because strain K-12 restricts (hydrolyses) MS-1 DNA, a suitable permissive recipient K-12 had to first be constructed.

Clones comprising the MS-1 gene library were screened for siderphore synthesis in the belief that a fundamental aspect of magnetite production is

the necessity for cells to first accumulate extra cellular iron internally. However, no siderphore producing colonies were detected on a medium specifically designed (by Dr. J. Neilands, U. Cal. Berkeley) to reveal siderphore producing bacterial strains. Several possible reasons for not detecting clones with siderphore genes using this system are under continuing investigation.

On a positive note, the genomic DNA of strain MS-1 was probed with a nick translated modified E. coli outer membrane protein-specific gene sequence as well as with synthetic oligonucleotide probes constructed from knowledge of the amino acid sequence of the E. coli outer membrane protein ton B involved in iron uptake. A homologous gene sequence was detected in the MS-1 DNA. This ton B sequence codes for a protein important in at least two efficient iron uptake systems in E. coli and other Gram negative bacteria. An E. coli detection mutuant strain defective in this sequence has been constructed to serve as a recipient in cloning the homologous MS-1 sequence. These experiments demonstrate the feasibility of cloning and expressing in E. coli genes from strain MS-1. However, recent progress has improved our understanding of the proteins more intimately associated with the bacterial magnetosome than those of the cell outer membrane (see Sect. III-D,). As such, these proteins are much more desirable candidates for constructing probes for detecting magnetite. Specific genes in our genomic library, and efforts to determine their amino acid sequence in preparation for constructing probes, have begun. In summary, DARPA supported research has contributed to a "green light" status for initiating intensive efforts to clone magnetite genes from strain MS-1 with the long range intent of constructing magnetic forms of other microorganisms.

SUPPLEMENT 2 — METAL UPTAKE BY MAGNETIC BACTERIA

A. Introduction

Bacterial cells are small particles with a large surface area-to-volume ratio. They have functional wall groups with negative charges on their surface and they are enveloped by lipid membranes. All of these features contribute to their high capacity for adsorbing metallic cations or hydrophobic organic molecules. Thus, they readily bind metals or chlorinated hydrocarbons or polyaromatic hydrocarbons to which they are exposed. Magnetic bacteria are especially useful in this regard because they offer the promise of economical recovery of substances from polluted or metal-laden water or processes streams. Results of experiments with a number of metals (Cu, Cr, Co, Ni, Ti, Hg and Pb) indicate that even in concentrations as high as 200 μM, these do not prevent magnetosome formation or reduce the magnetism of magnetic bacteria. Equally important, the cells were not killed or destroyed by the highest metal concentration used. Thus, the bacteria appear quite suited for the accumulationo of these metals by passive sorption and could subsequently be used to collect or concentrate these metals by passage through a high gradient magnetic field.

One system we have investigated in more detail is the potential use of magnetic bacteria in recovery of Pu^{4+} from low level wastes too costly to process by chemical precipitation or ion exchange methods. Plutonium is vital to successful exploration of space (Pu^{238} is used to power satellites and space craft via radioisotope thermoelectric generators, RTG's). The coordination chemistry of Pu^{4+} is very similar, if not identical to, that of iron. Because it moves with ease along pathways normally used to channel iron into cells and competes with iron, it could be toxic and radiotoxic.

However, its half life is so long that in biological terms it is most helpful to consider it as "stably radioactive".

Microbes may concentrate and mobilize this metal through soil and water. Current problems at Hanford, WA and Savannah River Plant, SC involving leaking storage or waste repositories may be augmented by the action of microbes (or their chelators). The facility for binding and transporting Pu provided by microbes could be turned to advantage if those same microbes were also magnetic by virtue of possessing magnetosomes. In this case, the cells would provide a means of recovering the metal magnetically.

B. Approach and Results

Working with radiochemists at Los Alamos National Laboratory, BMC scientists investigated the binding of Pu^{4+} to magnetic bacteria and compared them in this regard with other bacteria noted for their Pu binding capacity (the latter had been isolated from soils and well fluids at Yucca Mtn. high level waste repository in Nevada).

Two strains of magnetic spirilla, MS-1 and MS-2, were used in preliminary growth experiments with low levels of Pu^{4+} (ca. 1 μCi/ml). Cell inocula were added to polycarbonate culture vessels containing known initial amounts of Pu^{4+}, and after growth the distribution of radioactivity in culture fluids, cells and culture vessel wall surfaces was determined. Values were compared to those obtained with uninoculated and killed cell controls. The initial and final radioactivity values were determined by means of liquid scintillation spectrometry techniques. Magnetic spirillum strain MS-2 adsorbed on a per cell bases, four times, or more, as much Pu^{4+}

as did bacterial strains previously chosen by LANL staff as their most effective in binding this radionuclide. More importantly, these results were reproducible, and equally important to their superior Pu binding , the cells remained intact (they grew) and were very magnetic. These results provided sufficient incentive to continue examining the possible role of magnetic bacteria as "vectors" for sequestering Pu from low level wastes and process streams.

Advantages over existing methods of Pu recovery include:

1. Lack of requirement for use of strong acids such as HNO_3;
2. Low cost separation techniques;
3. Lowered solution volumes;
4. Ability to recover Pu from very low level sources or solutions;
5. Lack of requirement for ion exchangers which in turn must be processed to remove Pu.

Future studies should include maximation of binding, magnetic recover of Pu-laden cells, and determining if Pu^{4+} enters the cell as does iron.

SUPPLEMENT 3 — A TEST FOR BIOACCUMULATION

A. Literature Review

The quest to recover metallic elements from the environment has recently intensified. Dwindling deposits of high grade metals have prompted extensive research for improved extraction procedures from low grade metal ores, principally sulfide complexes. Additionally, soluble metal species produced from mining, industrial processes, and municipal waste water are being released into the environment in frightfully high quantities. The solubility and retention of metals in the soil and water table is determined by the total amount released, the content of mobilizing and immobilizing organic matter, and the concentration of salts and ligands (S1). The ultimate fate of metals released is still uncertain, but the toxic nature of metallic ions poses a very real threat to all forms of life on this planet.

Historically, the recovery of precious and toxic metals has involved a variety of purely physico-chemical processes, including precipitation, ion exchange, solvent extraction, and electrowinning. These are inherently expensive and inefficient (S2). Advancements in microbial technology have provided incentives for both the industrially and environmentally inclined investor to investigate the feasibility of biological metal recovery from both waste water and sulfide ore deposits.

At present, microorganisms play their premier metal recovery role in the leaching process of low grade metal sulfide ores. Thiobacillus ferrooxidans is the primary prokaryote involved in this process. Hutchins et al. (S3) present an excellent review of recent developments in this field, especially with respect to leaching of uranium, copper, and precious metals, as well as the biogenic desulfurization of coal.

The ability of microorganisms to remove soluble metal ions from industrial and municipal waste waters is also currently under investigation. Two systems exist which account for the accumulation of metal cations from solution. **Passive accumulation** refers to the electrostatic association of positively charged metals ions with the negatively charged walls of bacteria and other microorganisms. Biosorbtion by bacteria appears to differ among morphological types. Gram positive bacteria have been shown to accumulate divalent cations by the negatively charged carboxyl groups of the peptidoglycan within the cell walls (S4). Investigators have also reported metal complexation by the phosphoryl substituents of the Gram negative lipopolysaccharide (S5). In either case, biosorption of metals by microorganisms offers feasable possibilities for recovery of metals from solution.

Biosorptive systems have mainly been studied with regard to heavy metal recovery. Lead, plutonium, uranium, and mercury are of particular interest because of their potentially toxic nanture as well as their relatively high content in mine tailings and industrial effluents. In a recent experiment, Nakajima et al. (S6) compared the absorbtive capacity of immobilized cells from a variety of microorganisms. They report the preferrential accumulation of uranium by all tested species of bacteria, yeasts, and fungi when saturated with a mixed metal solution. The bacterial and fungal species absorbed an average of 80 to 90 mg of uranium per gram of dry biomass while the tested yeast strains accumulated only half as much. The amount of biosorbed lead and copper was comparable among the tested microorganisms, averaging about 35-45 mg per gram of dry biomass. The lighter transition metals, such as cadmium, zinc, nickel, cobalt, and

manganese were absorbed only in trace amounts.

Friis et al. (S7) have shown that the dry biomass of Streptomyces longwoodensis is an extremely effective biosorbent material. Columns containing these organisms complex up to 0.44 g of uranium per gram of dry weight biomass at pH 5.0. Determining the relationship between the phosphorus content and uranium uptake, these investigators propose that the metal ions are bound to the phosphodiester residues within the Gram negative wall. Algae have also been shown to be effective biosorbents. Hasset et al. (S1) reported that high levels of lead, zinc, copper, mercury, and cadmium in a lead mine discharge stream were reduced to acceptable drinking levels by in situ algal biomass.

The second system of metal bioaccumulation does not involve electrostatic association of metal ions with the outer layers of cells. Alternatively, cells selectively transport metal ions across their cell membrane systems and accumulate them intracellularily. Compared to the large biosorptive capacity of microbial cells, intracellular accumulation is quite minimal and usually not feasable as a means of metal recovery. There exists, however, a group of unique bacteria which do accumulate large amounts of metals as intracellular inclusions. Magnetic bacteria recover solubilized iron from their environment and deposit it in the form of a crystallized iron oxide. In cells of Aquaspirillum magnetotacticum, the crystalline inclusions are composed of the iron oxide magnetite and account for about 2% of the cell's dry weight. This amount is comparable to the passive accumulation systems of the biosorbents discussed above. In this investigation we wished to determine whether cells of A. magnetotacticum can accumulate metals other than iron as partial constituents of their metallic

inclusions. Incorporation of toxic metals in a magnetic moiety could prove very valuable as a tool for metal reclamation.

B. Materials and Methods

1. Culture conditions

Cells of Aquaspirillum magnetotacticum were cultured with 0 μM, 20 μM, and 200 μM concentrations of each of the following compounds: $Cu(CH00)_2$ $2H_2O$, $CrCl_2$ gH_2O, $CoCl_2$ $6H_2O$, $NiCl_2$, $TiCl_3$, $HgCl_2$, and $Pb_3(C_6H_5O_7)$ $3H_2O$. All cultures were passed three times in the various media prior to sampling.

2. Electron microscopy

Unstained cells and cells negatively stained with 0.5% uranyl acetate were visually examined using a Hitachi H600 scanning-transmission electron microscope operating in the transmission mode at 80 kV accelelrating voltage. Cells were also examined using a VG Microscope HB5 scanning-transmission microscope operating in the STEM mode at an accelerating voltage of 100 kV. Elemental dispersive X-Ray anallysis (EDAX) was performed with a Link System LZ5 detector.

3. Purification of magnetite from cells

Cells were harvested from 15 1 growth vessels through tangential flow filtration followed by centrifugation at 5000 X g for 10 min. Cells were washed 10 times in 10 mM HEPES buffer (pH 7.4) and mechanically disrupted using a French pressure cell. Magnetic material was separated from non magnetic debris with the application of a strong magnetic field for one hour. The magnetite was liberated from associated organic matter by suspending the intact magnetosomes in 5N NaOH. The mineral phase was washed

excessively with deionized distilled water and magnetically separated from the supernatant fluid. Purified magnetite (approximately 10 mg wet weight) was solubilized in 10 ml of 0.1N HCl by incubating the suspension at room temperature for 7 days. The acidic metal solutions were analyzed using an Instrumentation Laboratories atomic absorption spectrophotometer operating with an acetylene-air flame for all metals except uranium which was combusted with an acetylene-nitrous oxide flame.

C. Results

1. Cellular morphology

As recorded in Figures S1-S3, cells cultured with each of the tested metals exhibited extensive production of poly-B-hydroxybutyric acid which appear as electron transparent intracellular deposits and also deeply stain with Sudan black for light microscopy. Adjacent to the PHB granules were electron dense inclusions. As evidenced by scanning electron microscopy and elemental dispersive X-ray analysis (Fig. S4), these deposits contain large amounts of sodium and phosphorus, consistent with the composition of polyphosphate inclusions. The also appear as red deposits in a blue cytoplasm when stained with toludine blue which is also indicative of polyphosphate. Positioning the electron probe next to these inclusions, the X-Ray signal for sodium and phosphorus decreases to background level (Fig. S5). Other metals were not detected within the polyphosphate inclusions.

Unusual magnetosome chain morphology was observed with many cells cultured at 20 μm and 200 μm concentrations of the investigated metals. The number of cells exhibiting aberrant magnetosome arrangement appeared to increase with each successive passage. By the eighth passage roughly 30% of the population contained unusual chains. Figure S6 is a photomicrograph of

an unstained cell grown with 20 μm Ni in which the magnetosomes do not line up in a single chain. Figure S7 represents a cell which was cultured with 20 μM lead. The divergent chain formation is quite apparent. Mercury grown cells as well exhibit aberrant magnetosome chain morphology, as depicted in Fig. S8. Although not indicative of the rest of the population, the ultimate in confused magnetosome arrangement is presented in Fig. S9. Multiple magnetosome chains assume no consistent orientation within the cell but are divided equally between the daughter cells of an apparently dividing cell.

2. Composition of magnetite particles

Results from elemental dispersive X-Ray analyses of the magnetite grains within intact cells growth with 20 μM nickel are presented in Fig. S10. As expected, iron is the predominant compositional element within the magnetic inclusions. Nickel was not detected within the magnetite grains, nor was detectable within the surrounding cytoplasm (Fig. S11). As evidenced by atomic absorption, none of the investigated metals were detected within the purified magnetic fraction.

D. Discussion

Cells of A. magnetotacticum are affected by relatively high concentrations of metals other than iron in at least three ways. Intracellular accumulation of PHB is normally associated with nitrogen or energy limitations. The exorbitant production of this carbon storage polymer observed during this study suggests that metals affect either nitrogen assimilation or some form of cellular catabolism. Likewise, the occurrence of polyphosphate granules is another indication that the tested

metals are somemhow affecting cellular metabolism, although at this point the mechanisms remain unkown.

Aberrant chain morphologies in magnetic cells is particularly interesting. Normally cultured cells contain about 20 octahedron shaped crystals of magnetite each measuring about 42 nm on a side and appear as a single chain along the central axis of the celll (S8). What determines the relatively consistent size of magnetosomes or why magnetosomes normally appear in chains is still a mystery. It has been speculated that the envelope surrounding each of the crystals may somehow be involved (S9). The effects of metals on aberrant chain morphology may prove beneficial for the elucidation of the controlling mechanisms of magnetosome formation.

Within the EDAX analysis cells of A. magnetotacticum do not seem to accumulate metals other than iron in their magnetic inclusion bodies. However it would be a grave error to assume tht there exists no magnetic species which can accumulate metals other than iron as intracellular inclusions. Environments rich in toxic metals have been repeatably shown to influence the population of indigenous microflora (S10, S11). Duxbury et al. (S12) have compared relative tolerances between bacteria isolated from metal laden waters to those found in waters which were free from high levels of metal contaminants. They report that tolerance to nickel by adapted bacteria was nearly four times as great as by cells from unpolluted environments. In a study by Aiking et al. (S13), cells of Klebsiella aerogenes were maintained at a steady state in a continuous culture system free from high levels of toxic metals. Upon the addition of 6×10^{-4} M cadmium, growth ceased by resumed (presumably reflecting adaptation) within 5 hours. The adapted cells were more resistant to cadmium and could be

maintained at a steady state in the presence of this metal. These cells also formed extracellular deposits of cadmium sulfide which accounted for about 2.5% of their dry weight. It was proposed that these sulfide deposits accounted for cadmium tolerance. Large cadmium resistant populations also occur naturally in soil to which metal-rich sewage sludge has been applied (S14).

Environmentally adapted organisms which concentrate toxic metals as intracellular deposits may exist but we must have a system by which we can recover them. Magnetic bacteria both provide a unique handle by which bacterially adsorbed metals may be recovered. Their ubiquitous nature supports the possiblity that they may indeed be recovered from the sediments of metal rich environments. The discovery of a magnetic bacteria which can incorporate toxic metals intracellularly should be quite valuable for the advancement of biologically mediated metal recovery and should be pursued.

E. References

S1. J. M. Hasset, J. C. Jennett, and J. E. Smith, "Heavy metal accumulation by algae," (1980) In. R. A. Baker (ed.) Contaminants and Sediments, p. 409. Ann Arbor Science, Ann Arbor, MI.

S2. D. G. Lundgren and E. E. Malouf, "Microbial extraction and concentration of metals," (1983) 223-249. In Advances in Biotechnological Processes 1. Alan R. Liss, Inc., NY.

S3. S. R. Hutchins, M. S. Davidson, J. A. Brierley, and C. L. Birerley, "Microorganisms in the reclamation of metals," (1986). In L. N. Orston, A. B. Balows, and P. Bauman (eds.) Annual Review of Microbiology. Annual Reviews Inc., NY.

S4. T. Beveridge and S. F. Koval, "Binding of metals to cell envelopes of Escherichia coli," Appl. Envir. Microbiol. 42 (1981) 325-335.

S5. T. Beveridge and G. Ferris, "Site specificity of metallic ion binding in Escherichia coli K-12 lipopolysaccharides," Can. J. Microbiol. 32 (1986) 52-55.

S6. A. Nakajima and T. Sakaguchi, "Selective accumulation of heavy metals by microorganisms," Appl. Biotech. Microbiol. 24 (1986) 59-64.

S7. N. Friis and P. Meyers-Keith, "Biosorption of uranium and lead by Streptomyces longwoodensis," Biotechnol. Bioeng. 28 (1986) 21-28.

S8. D. L. Balkwill, D. Maratea, and R. P. Blakemore, "Ultrastructure of a magnetic spirillum," J. Bacteriol. 141 (1980) 1399-1407.

S9. R. P. Blakemore, "Magnetic bacteria," (1982). In Annual Reivews of Microbiology, Annual Reviews Inc., Palo Alto, CA.

S10. B. Austin, D. A. Allen, A. L. Mills, and R. R. Colwell, "Numerical taxonomy of heavy metal-tolerant bacteria isolated from an estuary," Can. J. Microbiol. 23 (1986) 1433-1447.

S11. C. Houba and J. Renacle, "Composition of saprophytic bacterial communities in freshwater systems contaminated by heavy metals," (1980).

S12. T. Duxbury and B. Bicknel, "Metal tolerant bacterial populations from natural and polluted soils," Soil Biol. Biochem. 15 (1983) 243-250.

S13. H. Aiking, K. Kok, H. van Heerikhuizen, and J. van't Riet, "Adaption to cadmium by Klebsiella aerogenes growing in continuous culture proceeds mainly via formation of cadmium sulfide," Appl. Envir. Microbiol. 44 (1982) 938-944.

S14. T. Barkay, S. C. Trip, and B. H. Olson, "Effects of metal-rich sewage sludge application on the bacterial community of grasslands," Appl. Envir. Microbiol. 49 (1985) 333-337.

F. Figure Captions

Fig. S1: Cells of A. magnetotacticum grown with 20 μm added nickel. Note the electron transparent regions which have previously been identified as poly-B-hydroxybutryrate granules. Electron dense inclusions are also evident.

Fig. S2: Enlargement of a cell of A. magnetotacticum grown with 20 μm added nickel. Note the electron transparent poly-B-hydroxybutyrate granules. Electron dense inclusions are also evident.

Fig. S3: Unstained preparation of A. magnetotacticum grown with 20 μM added nickel. As shown in the previous figure, electron dense and electron transparent regions are quite evident.

Fig. S4: EDAX spectrum of an electron dense inculsion within a cell of A. magnetotacticum grown with 20 μm added nickel. Note the high sodium and phosphorus peaks which are consistent with polyphosphate inclusions. Also note the absence of a peak for nickel.

Fig. S5: EDAX spectrum of cytoplasm adjacent to putative polyphosphate inclusions of cells grown with 20 μm nickel. Notoe the reduction in sodium and phosphorus peaks.

Fig. S6: Nickel grown cell of A. magnetotacticum exhibiting aberrant magnetosome chain morphology.

Fig. S7: A. magnetotacticum grown in the presence of 20 μm added lead. Note the duel chain formation which is abnormal in this species.

Fig. S8: A. magnetotacticum cultured with 20 μm added mercury. Multiple discontinuous chains are quite evident.

Fig. S9: Cell of A. magnetotacticum which had been passed five times in media containing 20 μm added nickel. Note the extremely abnormal chain morphology.

Fig. S10: EDAX spectrum of a magnetosome within a cell cultured with 20 μm added nickel. Note the absence of a nickel peak. The peak which is adjacent to the region expected for nickel is a copper response generated from the grid.

Fig. S11: EDAX spectrum of cytoplasm which is adjacent to a magnetosome within a cell grown with 20 μm added nickel.

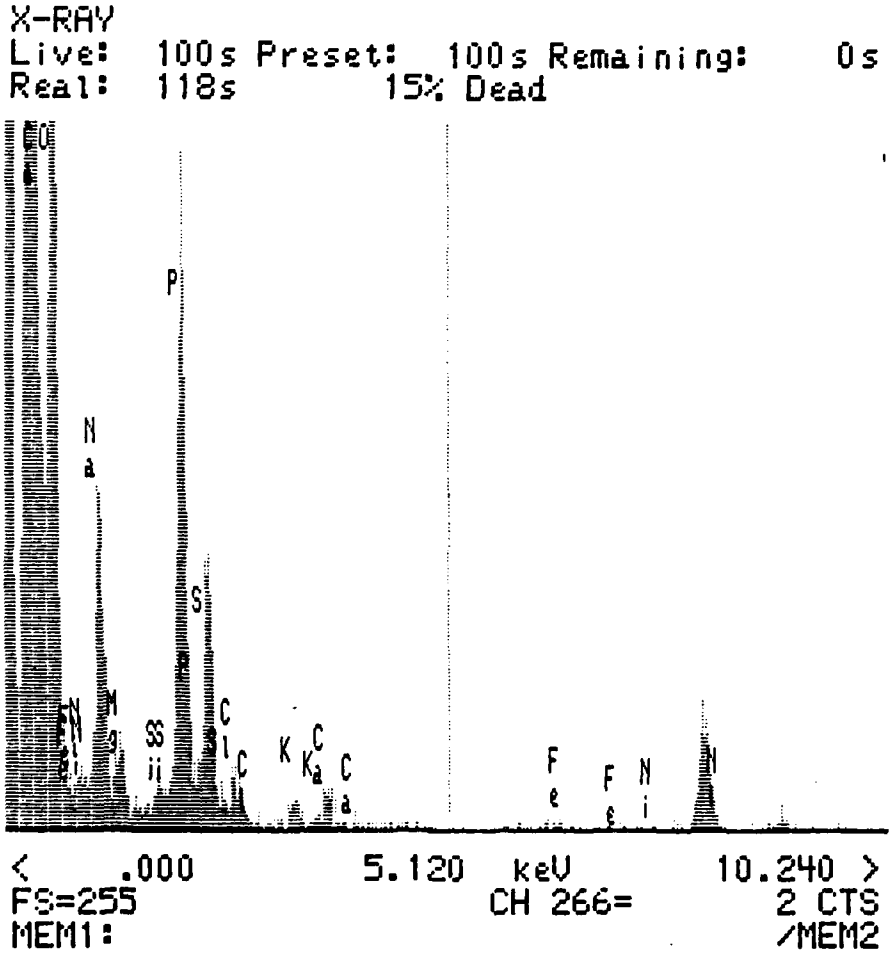
X-RAY
Live: 100s Preset: 100s Remaining: 0s
Real: 118s 15% Dead
P
S
K
F
e
F
e
N
i
< .000
5.120 keV
10.240 >
FS=255
CH 266=
2 CTS
MEM1:
/MEM2

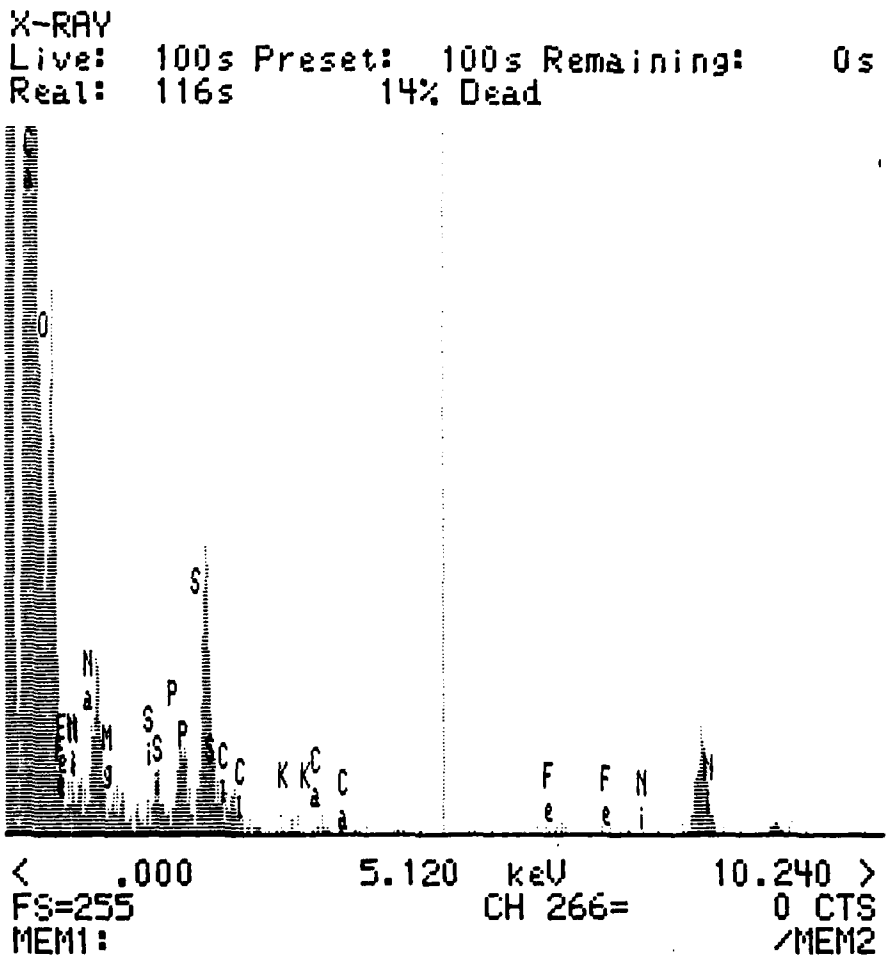
X-RAY
Live: 100s Preset: 100s Remaining: 0s
Real: 116s 14% Dead
O
Na
Mg
Si
P
S
Ca
Fe
Ni
< .000
5.120 keV
10.240 >
FS=255
CH 266=
0 CTS
MEM1:
/MEM2

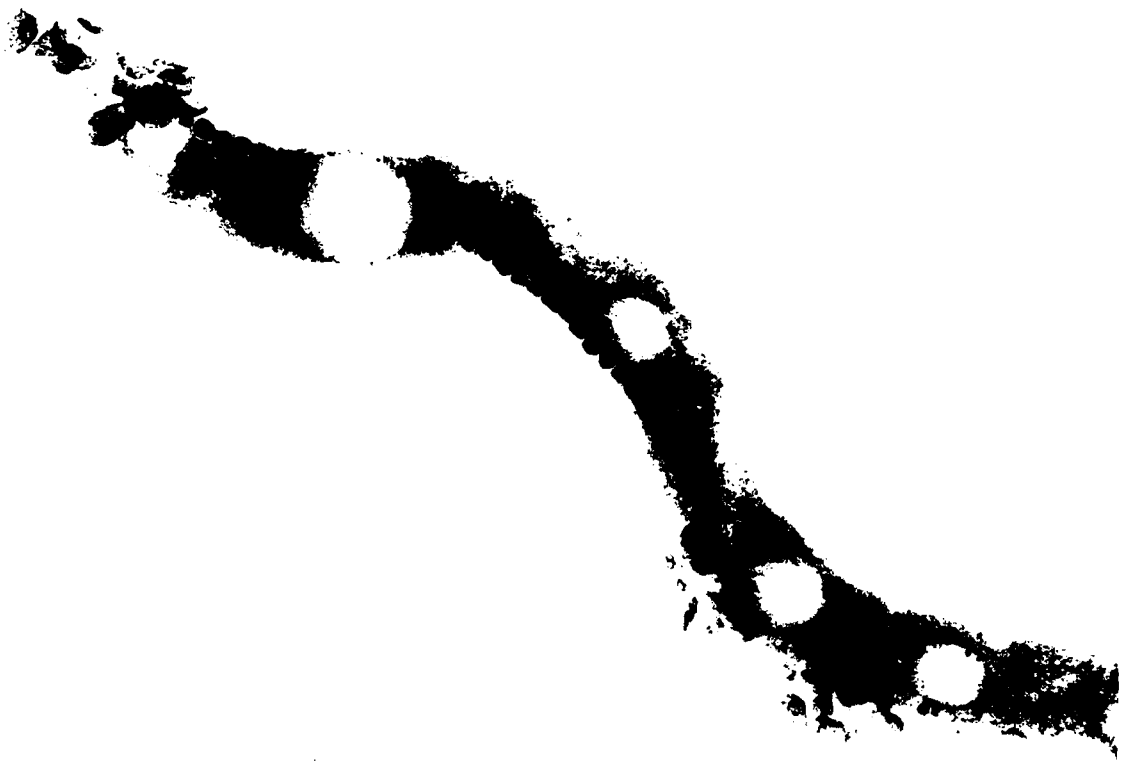

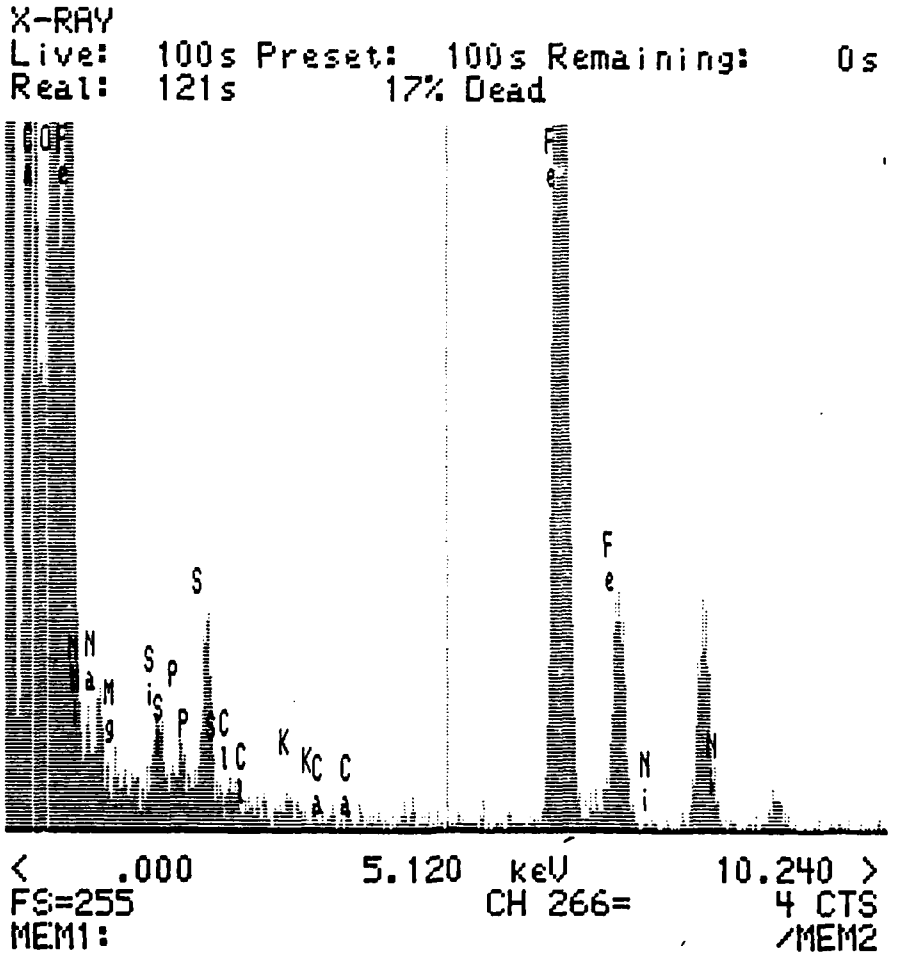
X-RAY
Live: 100s Preset: 100s Remaining: 0s
Real: 121s 17% Dead
O
Fe
Na
Mg
Si
S
P
Cl
K
Ca
Fe
Ni
.000
5.120 keV
10.240
FS=255
CH 266=
4 CTS
MEM1:
/MEM2

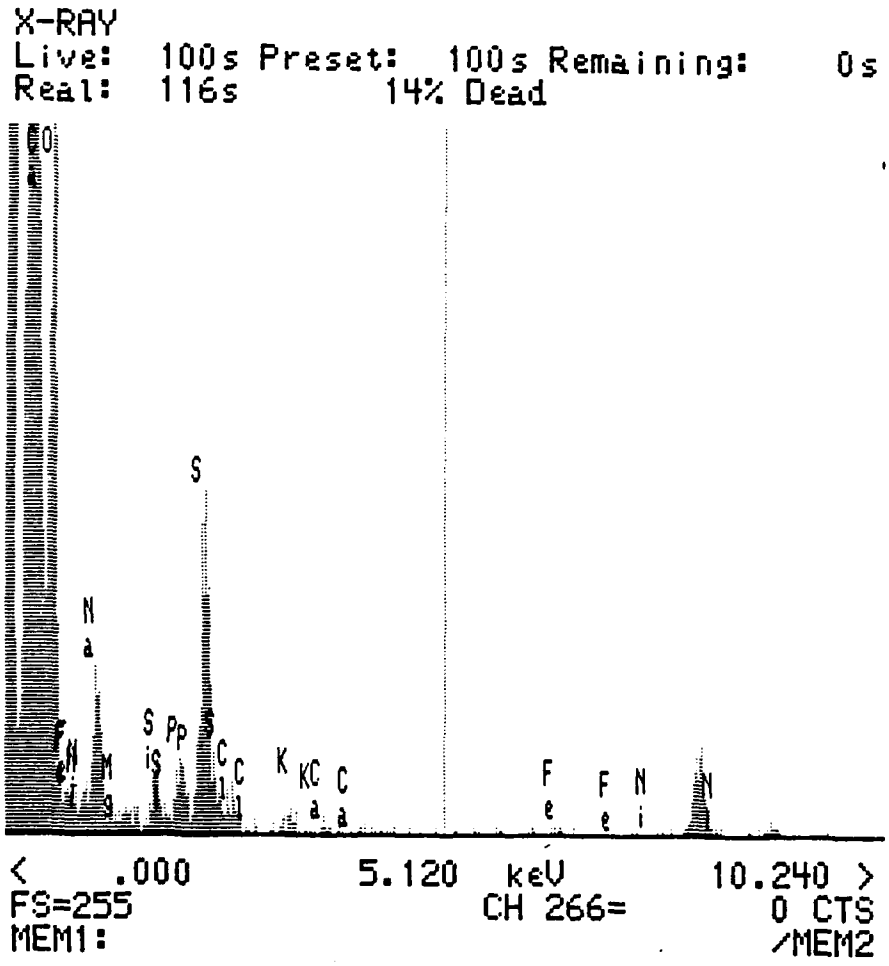
X-RAY
Live: 100s Preset: 100s Remaining: 0s
Real: 116s 14% Dead
O
Na
S
Si
Pp
K
Ca
Fe
Fe
Ni
Ni
< .000 5.120 keV 10.240 >
FS=255 CH 266= 0 CTS
MEM1: /MEM2